# COMPUTATIONAL STUDY OF 3D TURBULENT FLOW IN A TANDEM INDUCER/IMPELLER ROCKET PUMP ROTOR

by

Philippe Renaud

Thesis submitted to the Faculty of the

Virginia Polytechnic Institute and State University

in partial fulfillment of the requirements for the degree of

Master of Science

in

Mechanical Engineering

APPROVED :

Dr. John Moore, Chairman

Dr. J.A. Schetz

Dr. W.F. Ng

March, 1995

Blacksburg, Virginia

C. 2

LD
5655
V855
1995
R463
C. 2

# COMPUTATIONAL STUDY OF 3D TURBULENT FLOW IN A TANDEM INDUCER/IMPELLER ROCKET PUMP ROTOR

by

Philippe Renaud

Dr. John Moore, Chairman

Mechanical Engineering

(ABSTRACT)

A computational study of the flow in a tandem inducer/impeller rocket pump has been performed using a 3D elliptic flow program including viscous effects. The axial inducer has four blades and the centrifugal impeller has eight main blades and sixteen splitter blades. The purpose of this thesis is to investigate the flow in the turbopump, and check its proper design .

A literature review discusses both elements of the pump, and then analyzes the possible matching configurations. More details are given for the geometry of interest .

The generation of a single zone 3D grid for the tandem combination is then presented in detail, after which simpler grids are derived for the inducer alone .

The results of the 3D tandem inducer/impeller calculation are presented extensively to provide good knowledge of the flow inside this little investigated configuration. Velocity vectors, static pressure and rotary stagnation pressure are shown in meridional and blade-to-blade views. A balanced flow split is achieved in the impeller main-blade passages. Cavitation inception is also discussed .

Additional 3D calculations are performed for the inducer alone, with varying exit geometry (axial or radial). Comparisons of geometry influence on the inducer flow are carefully investigated, as well as the influence of the impeller. The impeller slightly modifies the inducer exit flow but not its overall performance. As a consequence, it is found that separate design calculations could be performed for the inducer and the impeller. The latter would use the inducer circumferentially averaged exit flow as its inlet conditions. It is suggested that impeller suction performance be optimized using tandem inducer/impeller calculations .

## Acknowledgments

I would like to thank all the people who supported me during these 15 months I spent in Blacksburg, and who contributed to the achievement of this thesis .

First, I wish to express my sincere gratitude to Dr. John Moore, my advisor, and to Joan G. Moore, his wife, for their appreciated pedagogical qualities, their qualification from which I learned a lot, their enthusiasm in work and their sense of humor ("*d'Artagnan*") throughout this project. Thanks to Dr. J.A. Schetz and Dr. W.F. Ng who were also on my advisory committee .

I am very grateful to the "Société Européenne de Propulsion" which sponsored this project, especially to Philippe Geai and Evelyne Sauvage-Boutard without whom I would never have been able to undertake this Master's study. Thanks also to Frédéric, Jean-Michel, Thierry and Tony for their different support .

Finally, thousands of thanks to all my friends who shared these 15 unforgettable months and contributed to my "American dream" : my 'brother' Erwan (et zut!), Anne-Laure and Frédéric, Sandrine, Raphael, Luc and Marie-Laure, the 'big American cars French connection', Vincent et les autres (les p'tits jeunes), Adel and Amelene, Andrew, Bénédicte, Dan, Ehab, Gladys, Jean-Luc, John, Joe, Jeff, Loulou, Matt, Pierre, Rebecca, Rose, Ruth, Sabrina, Samir, Scott, my roommates, Valérie, Lincoln and my enormous V8 big old boat of a car, and all the others who spent some time with me .

*To Caridel .*

# TABLE of CONTENTS


**1.0 INTRODUCTION . 1**

**2.0 LITERATURE REVIEW . 6**

*2.1 Introduction . 6*
2.1.1 Cavitation . 6
2.1.2 Inducers . 9
2.1.2.1 Design . 9
2.1.2.2 Inducer flow field . 10
2.1.2.3 Previous computational studies . 12
2.1.3 Impellers . 14
2.1.3.1 Classification . 15
2.1.3.2 Design . 18
*2.2 Inducer / impeller configurations . 20*
2.2.1 The different matching solutions . 20
2.2.1.1 Separate shafts configuration . 20
2.2.1.2 In-between inducer/impeller stator vane configuration . 20
2.2.1.3 Integral inducer/impeller configuration . 20
2.2.1.4 Tandem inducer/impeller configuration . 24
2.2.2 Details about the tandem inducer/impeller combination . 24
2.2.2.1 Advantages . 27
2.2.2.2 Flow investigations . 28
*2.3 Previous computations for the VULCAIN inducer . 29*
2.3.1 Inducer alone calculation [17] . 29
2.3.2 Tandem bladed inducer calculation [18] . 31
*2.4 The Moore Elliptic Flow Program (MEFP) . 35*

**3.0 SCOPE AND OBJECTIVES OF THIS RESEARCH . 37**

**4.0 GENERATION OF 3D FINITE DIFFERENCE CALCULATION GRIDS . 39**

*4.1 Data provided . 39*
4.1.1: The initial meridional 2D grid : 40
4.1.2: The inducer : 40
4.1.3: The impeller : 40
*4.2 Blade interpolation . 44*
4.2.1: Why interpolate the blades ? : 44
4.2.2: The interpolation grid : 44
4.2.3: The interpolation procedure : 45
*4.3 3D file generation for the different regions . 48*
4.3.1: The impeller : 48
4.3.2: The inducer : 48
4.3.3: The upstream region : 49
4.3.4: The downstream region : 49
4.3.5: The inducer/impeller gap region : 50
*4.4 Construction of 3D calculation grids . 51*
4.4.1: goptw : A tool to manipulate grids : 51
4.4.2 : Turbopump assembling - Grid refinements : 51
4.4.2.1 Changes in the i-direction 51
4.4.2.2 Tip-gap definition 51
4.4.2.3 Changes in the k-direction 52
4.4.2.4 Smoothing in the j-direction, in the inducer 52
4.4.2.5 Impeller leading edges correction 52
4.4.2.6 Grid smoothing in the j-direction, in the impeller 52
*4.5 Final 3D grids . 53*
4.5.1 : Tandem inducer/impeller 3D grid : 53
4.5.1.1 Grid definition 53
4.5.1.2 A,B,C parameters 53
4.5.2 : Inducer alone 3D grids : 57
4.5.2.1 New grid-spacing in the j-direction 57
4.5.2.2 Radial-exit grid 58
4.5.2.3 Axial-exit grid 58

**5.0 RESULTS OF THE TANDEM INDUCER-IMPELLER 3D FLOW CALCULATION. 63**

*5.1 Introduction . 63*
*5.2 Calculation procedure and details : 64*
*5.3 Calculation main results . 65*
5.3.1: One-dimensional Mass-averaged pressures : 65
5.3.2: Flow split in the impeller : 68
5.3.3: Efficiencies : 70
*5.4 Inducer meridional results analysis . 72*
5.4.1: Velocity vectors : 72
5.4.2: Rotary stagnation pressure : 74
5.4.3: Inducer Leading Edge vortex : 74
5.4.4: Static pressure and blade-loading : 77
*5.5 Blade-to-blade results for the inducer and the impeller . 81*
5.5.1: Definition of the unrolled blade-to-blade view : 81
5.5.2: Velocity vectors : 81
5.5.3 : Rotary stagnation pressure : 85
5.5.4 : Static Pressure at the Exit of the Inducer : Influence on the Inter-Blade Gap . 87
*5.6 Loss build-up through the tandem inducer/impeller . 92*
*5.7 Flow analysis in the impeller . 95*
5.7.1: Meridional Velocities . 95
5.7.2: Impeller Blade Loading . 97
5.7.3: Static Pressure : 99
5.7.3.1 Blade-to-blade analysis 99
5.7.3.1 Blade surface analysis 99
5.7.4: Isentropic Relative Velocities in the Impeller : 104
5.7.4.1 Computation of the isentropic relative velocity W 104
5.7.4.2 Relative flow in the impeller 104
*5.8 Cavitation in the tandem inducer/impeller . 108*
5.8.1: Cavitation inception : 108
5.8.2: Cavitation patterns : 108
5.8.3: Inducer LE cavitation : 110

**6.0 COMPARATIVE STUDY OF DOWNSTREAM INFLUENCES ON THE INDUCER. 113**

*6.1 Introduction . 113*
*6.2 Main results of the comparative study . 115*
6.2.1: Mass-averaged pressures : 115
6.2.2: Efficiencies : 115
6.2.3: Circumferentially averaged flow at the inducer exit : 117
6.2.4: Inducer/impeller matching : 122
*6.3 Introduction to the impeller and geometry influences on the inducer . 128*
*6.4 Blade-to-blade and inter-blade gap results . 132*
6.4.1: Definition of accurate constant fraction-of-height surfaces : 132
6.4.2: Reduced pressure : 132
6.4.3: Rotary stagnation pressure : 137
*6.5 Inducer meridional analysis : static pressure and blade-loading . 140*
*6.6 Insight into the inducer/impeller uncoupling . 151*
*6.7 Conclusions relative to downstream inducer influences . 145*

**7.0 CONCLUSIONS . 146**

**BIBLIOGRAPHY 150**

**APPENDIX 1 : BLADE INTERPOLATION PROCEDURE . 157**

**APPENDIX 2 : MEFP GEOMETRY FORMAT 163**

**Vita 167**

# TABLE of ILLUSTRATIONS

Figure 1 : Typical tandem inducer/impeller configuration .....2

Figure 2 : S.E.P Tandem inducer/impeller MCA geometry .....4

Figure 3 : Cavitation influence on head-rise : Head vs. NPSH (from [2]) .....8

Figure 4 : Basic inducer types (from[3]) .....11

Figure 5 : Qualitative nature of flow field inside inducer passages :
secondary flows (from [14]). .....13

Figure 6 : Shrouded/unshrouded impellers and their relative performance
(from [4]) . .....16

Figure 7 : Low and High pressure fuel turbopumps in the SSME (from [36]) . .....21

Figure 8 : Rocketdyne ADP fuel turbopump (from [35]) . . .....22

Figure 9 : Integral inducer/impeller (from[27]) . .....23

Figure 10 : Evolution of the Tandem inducer/impeller configuration .
Part A . (from [36]) . . .....25

Figure 11 : Evolution of the Tandem inducer/impeller configuration .
Part B . (from [35] and [25]) . . .....26

Figure 12 : Velocity vectors on meridional views of the first blade (from [17]) . .....30

Figure 13 : Radial distribution of losses at the inducer exit (from [17]) . .....32

Figure 14 : Comparison of the blade loadings for the inducer :
(a) alone [17] and (b) : in the tandem bladed configuration [18] . .....33

Figure 15 : Radial distribution of losses in the tandem bladed inducer (from [18]) . .....34

Figure 16 : Meridional view of the initial grid . .....41

Figure 17.a : Axial view of the inducer (pressure surface) .....42

Figure 17.b : Meridional view of the inducer (both surfaces) . .....42

Figure 18 : Meridional view of the impeller main and splitter blades (both surfaces) ...43

Figure 19 : Final Interpolating Grid .....46

Figure 20 : Comparison between the initial and the interpolated blade
(hub layer of the impeller main blade) . .....47

Figure 21 : Meridional view of the 85x31x14 calculation grid . .....54

Figure 22 : Unrolled blade-to-blade view of the full tandem
inducer/impeller grid (85x31x14) .....55

Figure 23 : Meridional view of the IARC grid (83x15x15) . .....60

Figure 24 : Unrolled blade-to-blade view of the IARC grid (83x15x15) .....61

Figure 25 : Meridional view of the IAXC grid (70x15x15) . .....62

Figure 26 : Mass-averaged pressure coefficients . .....66

Figure 27 : Mass-averaged losses throughout the MCA configuration . . .....67

Figure 28 : Flow split in the impeller . . .....69

Figure 29 : Meridional view of the velocities in the inducer . .....73

Figure 30 : Meridional view of rotary stagnation pressure, P*, in the inducer .
Contour interval 0.05,0.2 . .....75

Figure 31 : Cross-sectional views of the inducer leading edge vortex . .....76

Figure 32 : Meridional view of the static pressure, P, in the inducer . Contour interval 0.01,0.05 . ....78

Figure 33 : Meridional view of the inducer blade loading . Contour interval 0.02,0.1 . ....79

Figure 34 : Blade-to-blade view of velocity vectors through the inducer and the impeller, near the hub . ....82

Figure 35 : Blade-to-blade view of velocity vectors through the inducer and the impeller, near mid-height . ....83

Figure 36 : Blade-to-blade view of velocity vectors through the inducer and the impeller, near the tip . ....84

Figure 37 : Blade-to-blade view of rotary stagnation pressure through the inducer and the impeller, near mid-height . Contour interval 0.05,0.1 . ....86

Figure 38 : Blade-to-blade view of the static pressure in the inducer and the inter-blade gap (hub). Contour interval 0.01,0.05 ....88

Figure 39 : Blade-to-blade view of the static pressure in the inducer and the inter-blade gap (mid-height) . ....89

Figure 40 : Blade-to-blade view of the static pressure in the inducer and the inter-blade gap (tip) . ....90

Figure 41 : PS and SS isentropic relative velocity in the inducer . ....91

Figure 42 : Loss build-up through the tandem inducer/impeller combination . ....94

Figure 43 : Meridional view of the impeller near-wall velocity vectors . ....96

Figure 44 : Blade loading of the impeller (contour interval 0.2) . ....98

Figure 45 : Blade-to-blade view of the static pressure in the impeller (hub) ....100

Figure 46 : Blade-to-blade view of the static pressure in the impeller (mid-height) ....101

Figure 47 : Blade-to-blade view of the static pressure in the impeller (tip) . ....102

Figure 48 : Comparison between the static pressure coefficient (PS & SS) of MB1 and MB2 at k=6 (mid-height) ....103

Figure 49 : Isentropic relative velocity (PS & SS, near-wall) for (SP1,SP2,MB1) and (SP3,SP4,MB2) at k=6 (mid-height) .....105

Figure 50 : Across the channel relative velocity (PS & SS) for all the blades, at mid-height .....107

Figure 51 : Blade-to-blade view showing static pressure coefficients below zero and the possibility of cavitation inception (mid-height, tip, tip gap) . Contour interval 0.01,0.05 .....109

Figure 52 : Meridional view of the blade-to-blade cavitation core decay . Contours for P<-0.05. Contour interval 0.01,0.05 . .....111

Figure 53 : Cross-sectional view of the cavitation core . Contour interval for P : 0.01,0.05 . .....112

Figure 54 : Mass-averaged pressure coefficients for the three calculations . .....116

Figure 55 : Location of the axial cut plane in the tandem (a) and axial (b) cases .....118

Figure 56 : Hub-to-shroud circumferentially averaged profiles : (a) total pressure ; (b) static pressure ; (c) rotary stagnation pressure (bottom) .....119

Figure 57 : Hub-to-shroud circumferentially averaged profiles : (a) axial relative velocity (top) ; (b) tangential velocity ; (c) relative flow angle (bottom) .....121

Figure 58 : Comparison of the actual inducer/impeller gap with Jakobsen's suggestion . .....125

Figure 59.a : Inducer/impeller gap in the LE-5 Liquid Oxygen Turbopump [25] . . .....126

Figure 59.b : Observed gaps in the tandem inducer/guid vane/impeller combination of the LE-7 Fuel Turbopump .....126

Figure 60 : Possible modification for the inducer/impeller gap . .....127

Figure 61 : Backflow development in the tandem inducer/impeller. .....129

Figure 62 : Static pressure in the gap (A=1.225) for the three configurations . .....131

Figure 63 : Blade-to-blade view of the reduced pressure near the hub, for the IARC and the ITC . .....134

Figure 64 : Blade-to-blade view of the reduced pressure at mid-height, for the IARC and the ITC . .....135

Figure 65 : Blade-to-blade view of the reduced pressure near the tip & shroud, for the IARC and the ITC . .....136

Figure 66 : Cross-sectional views of loss build-up at the inducer TE and in the gap, for the three configurations .....139

Figure 67 : Meridional view of the static pressure at mid-passage, for the three configurations .....141

Figure 68 : Meridional view of the ITC, IAXC and IARC inducers blade loadings . ....142

Figure 69 : Meridional view of the two grid systems (superposition) . .....159

Figure 70 : Double linear interpolation procedure . .....162

Figure 71 : GEOMI triple coordinate system : (I,J,K), (A,B,C) and (x,y,z) . .....166

# LIST of TABLES

Table 1 : Advantages of the combined inducer/impeller (from[38]) . .....27

Table 2 : Definition of the C parameter. .....57

Table 3 : Flow split in the impeller . .....68

Table 4 : Relative importance of the different terms in the efficiency computation for the MCA elements . .....70

Table 5 : Relationship between losses and flow split . . .....93

Table 6 : Computation of the efficiency for the different inducers . .....115

# NOMENCLATURE

**Roman**

A = grid parameter in the streamwise direction, or area

b = impeller passage height

B = grid parameter in the tangential direction

C = grid parameter in the hub-to-shroud direction

c = chord length (m)

$C_p$ = static pressure coefficient

dx = infinitesimal variation of x

D = diameter (m)

DZJ = axial distance recommended by Jakobsen

g = gravitational acceleration ($m^2/s$)

H = stagnation head rise (m)

i = grid index in the streamwise direction

j = grid index in the tangential direction

k = grid index in the hub-to-shroud direction

$L$ = mixing length (m)

$\dot{m}$ = mass flow rate (kg/s)

$N$ = rotation speed (rpm)

NPSH = Net Positive Suction Head (m)

$N_s$ = specific speed

$p_{crit}$ = value of p at cavitation inception (Pa)

$p_{vap}$ = vapor pressure (Pa)

$p$, $p_s$ = static pressure (Pa)

$P$, $P_s$ = static pressure coefficient

$p_t$ = stagnation pressure (Pa)

$P_t$ = stagnation pressure coefficient

$p_r$ = reduced pressure (Pa)

$P_r$ = reduced pressure coefficient

$p^*$ = rotary stagnation pressure (Pa)

$P^*$ = rotary stagnation pressure coefficient

$Q$ = volumetric flow rate (m3/s)

$r$, $R$ = radius (m)

$\mathbf{r}$ = position vector

$\bar{r}$ = dimensionless hub-to-tip radius

Re = Reynolds number

$s$ = unrolled streamwise distance (m), or position along the blade chord (m)

$S_s$ = suction specific speed

T = temperature (K)

U = blade speed (m/s)

V = absolute velocity (m/s)

w = work done per unit mass flow rate (J/kg)

W = relative velocity (m/s)

**W** = relative velocity vector

z = axial position (m)

**Greek**

$\beta$ = flow angle relative to axial direction (degree)

$\eta$ = hydraulic efficiency

$\theta$ = angular (tangential) location (rad)

$\mu$ = kinematic viscosity (kg/m s)

$\nu$ = hub-to-tip ratio

$\omega$ = rotation rate (rad/s)

$\Omega$ = rotation rate vector

$\rho$ = density (kg/m3)

$\phi$ = flow coefficient

$\sigma$ = cavitation parameter, or solidity c/s

$\tau$ = shear stress

$\Psi$ = head coefficient

$\Psi_E$ = moment of momentum coefficient

$\Psi_{loss}$ = loss coefficient

$\Psi_t$ = total pressure coefficient

$\Psi_{TSs}$ = dissipated moment of momentum coefficient (due to wall-shear stresses on the stationary shroud) .

**Subscript**

0 = reference station upstream of the inducer, or at the diffuser inlet

1 = inlet reference station

2 = exit reference station

c = critical (cavitation)

f = final

h = hub

max = maximum

min = minimum

n = nominal condition

s = shroud

t = total, or tip

vap = vapor

z = axial

$\theta$ = tangential

**Superscript**

$\overline{A}$ = A area-averaged

$\overline{\overline{A}}$ = A mass-averaged

T = transposed

**Abbreviations**

2D = two-dimensional

3D = three-dimensional

IAC = inducer alone configurations

IARC = inducer alone in the radial configuration

IAXC = inducer alone in the axial configuration

ITC = inducer in the tandem configuration

LE = leading edge

LTE = leading and trailing edges

MB = main blade

PS = pressure side

SP = splitter

SS = suction side

TE = trailing edge

# 1.0 INTRODUCTION

Launching vehicles into space requires high specific power engines and high energy fuels to reduce as much as possible the weight of the launcher, and therefore increase the payload. Minimizing weight demands low propellant storage pressures to decrease the thickness of the tank walls. It also requires minimum weight for the feeding and combustion systems .

These severe requirements first cause hydrogen and oxygen to be generally used as the propellants because they provide one of the most powerful combustion reactions. Then, low weight feeding systems make use of high rotational speed turbopumps to increase the pressure for the combustion chamber .

The combination of low pressure stored propellants with high rotational speeds give rise to inevitable cavitation, which may be detrimental to the pump performance. Cavitation-resistant inducers, used as the first stage of the main pump, raise the static pressure enough to allow cavitation bubbles to collapse before they enter the following blade-rows. An important step was made by NASA in the understanding of cavitating rocket pump inducers with the development of the SSME oxidizer turbopump. Working in the same way, the French "Société Européenne de Propulsion" (S.E.P) developed a tandem-bladed inducer for the LH2 turbopump of the VULCAIN engine for the European launcher ARIANE V.

With the challenge of ever increasing power with decreasing turbopump sizes and weights, various concepts are being investigated. Among them, the tandem inducer/impeller configuration offers the possibility to eliminate the guide vanes used to direct the flow between the inducer exit and the impeller inlet. Thus, the turbopump weight and length are decreased, and more mechanical simplicity is achieved. Figure 1 shows a typical tandem inducer/impeller configuration. The inducer tip gap can be seen.

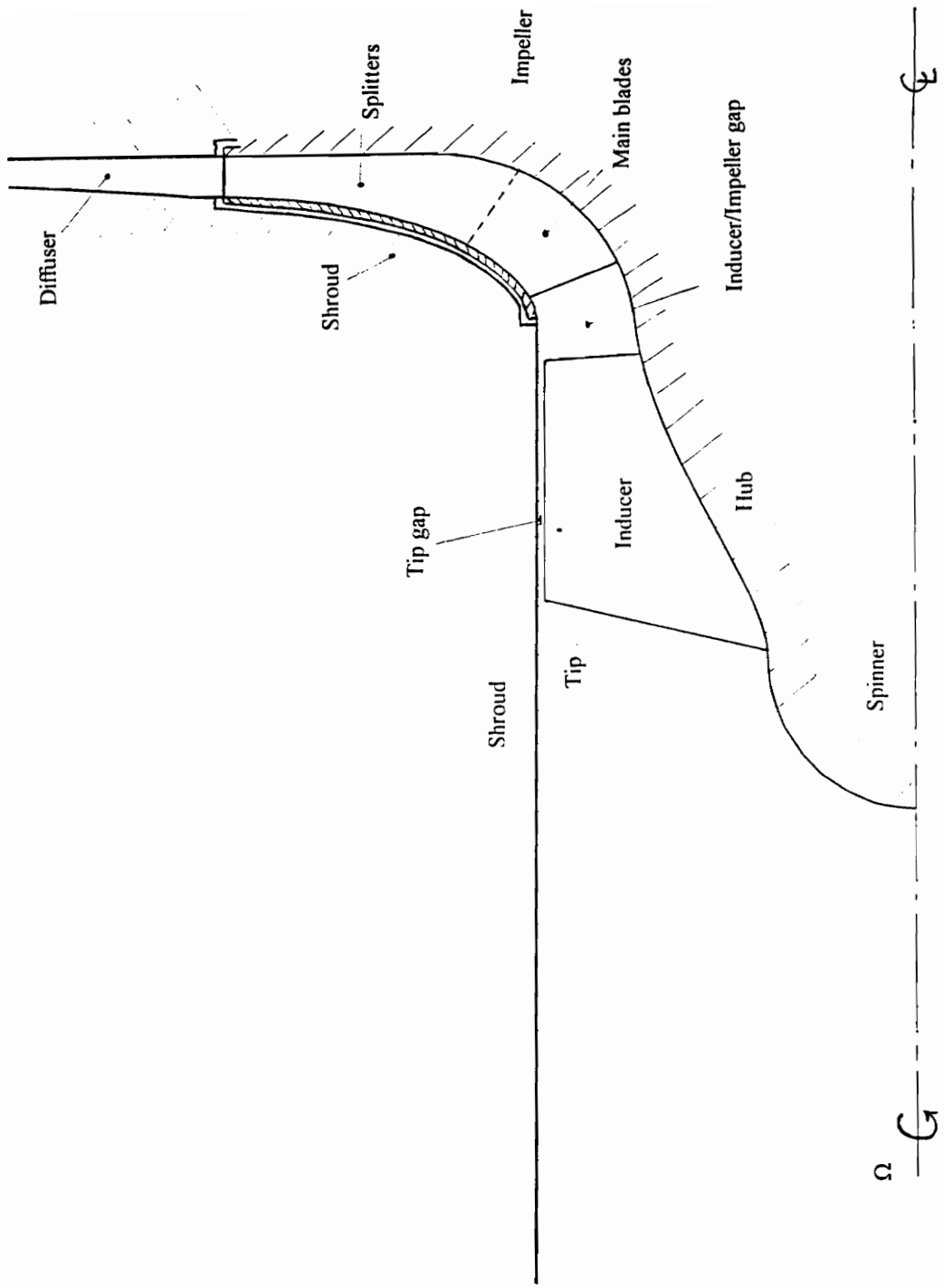


*Figure 1 : Typical tandem inducer/impeller configuration .*

There are no guide vanes between the two stages. The impeller is shrouded, and can incorporate splitter blades .

The development of the LE5 engine in Japan belongs to this category of turbopumps. The interest lies in higher pump efficiencies obtained in the range of small stage specific speeds compared to usual designs. As a part of its research for post-ARIANE V launchers, S.E.P is studying a new concept of turbopump in which the tandem inducer/impeller configuration has to be integrated. The MCA geometry (Fig. 2) consists of a four bladed-inducer immediately followed by a 24 bladed, highly-loaded shrouded impeller (8 main blades and 16 splitters, with two splitters per main blade passage). Both inducer and impeller are rotating at the same speed, and no blade row is used between them to guide the flow. The figure shows the geometry : (1) in a quasi-axial view, from which one can see the relative orientations of the inducer trailing edges and the impeller main blades leading edges ; and (2) in a side view, in which the inducer/impeller gap can be seen .

Many features are of interest in this particular geometry :

_ As far as design is concerned, the optimum locations (in the meridional and blade-to-blade views) of a) the leading edges of the impeller main blades with respect to the inducer blade and b) of the leading edges of the splitter blades with respect to the impeller main blades are sought .

_ Besides achieving the required performance with maximum efficiency, one is interested in physical phenomena that may occur in the inducer/impeller gap, in the impeller itself, or upstream of the inducer. Of particular interest is the possibility of backflows or separation at the impeller inlet, as well as the inducer/impeller interaction in the gap .

So far, very little work (both numerical or experimental) is available for the tandem configuration. The use of 3D Navier-Stokes codes is a valuable technique in predicting the performance and flow characteristics of such a combination. This thesis presents the first known calculation of the 3-D flow inside a tandem inducer/impeller. It is also the first high-Reynolds-number calculation at real engine operating conditions (fluid, rotation speed, flow rate). The flow calculations will be performed using the *Moore Elliptic Flow Program* (MEFP) developed at Virginia Polytechnic Institute and State University by Joan G. Moore and John Moore. This computer code was used for the two previous VPI&SU/S.E.P studies, the inducer calculations of LeFur, and the tandem-bladed inducer calculations of Excoffon .

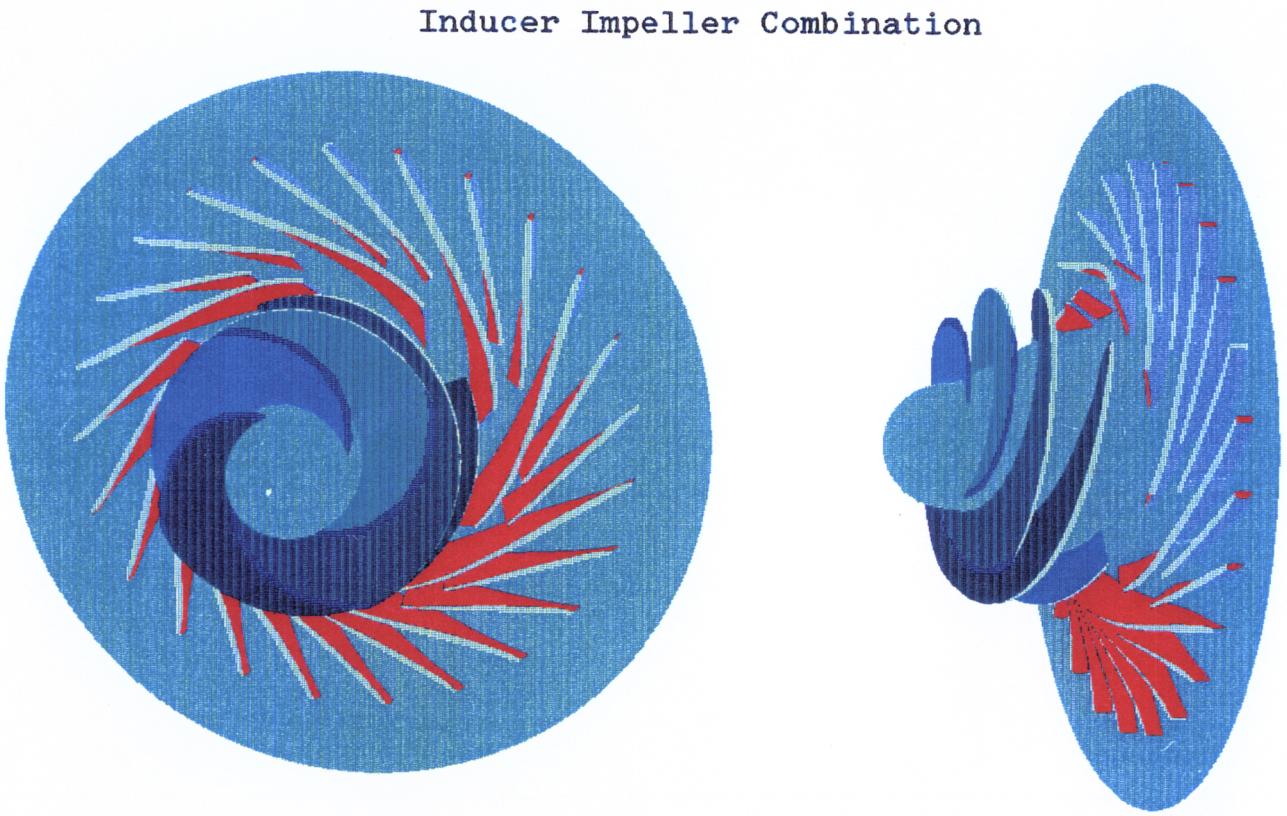


*Figure 2 : S.E.P Tandem inducer/impeller MCA geometry .*

The 3D turbulent calculations performed in this thesis first aim at providing insight into the non-cavitating flow behavior inside the turbopump. Tandem calculations require large computational meshes, and much interest also lies into the determination of which calculation procedure to adopt : is a combined inducer/impeller flow calculation necessary or can separate calculations (one for each component) be performed ?

In this thesis, a literature review introduces the importance of cavitation and the roles of each component, the inducer and the impeller. The possible ways of matching the two are then discussed, and more emphasis is devoted to the tandem configuration. The results of the two previous SEP inducer calculations are reviewed as well as the principal characteristics of the MEFP code .

The scope and objectives of this work are then presented .

Before running the computations, 3D grids have to be defined. Chapter 4 details the construction procedure used to obtain the single zone grids required by MEFP from the geometry files provided by S.E.P .

Chapter 5 presents the results of the 3D calculation for the tandem inducer/impeller configuration performed at nominal conditions. The flow main characteristics are first presented, showing in particular the very good flow split between the impeller passages. The flow in the tandem configuration is then studied in terms of velocity field, pressure rise, loss build-up, blade loading and cavitation inception. Efficiencies are also predicted .

Performing simpler separate calculations for both elements requires a good understanding of the interactions between the inducer and the impeller. Also, the influence of the inducer exit geometry is of interest since the previous SEP calculations used axial exits, whereas the tandem geometry is characterized by a radial exit. Chapter 6 is devoted to analyzing the downstream influences on the inducer flow itself. The interest of an axial exit is shown, and the possibility of uncoupling the inducer and the impeller is considered in terms of impeller inlet flow and loss distributions. A procedure for performing an impeller alone calculation using the results of the inducer alone flow field is presented. Finally, the possible role of tandem inducer/impeller flow calculations in optimizing the inducer/impeller interaction is suggested .

**Note :**

Throughout this thesis, the tandem inducer/impeller configuration refers to an ***axial-inducer / centrifugal-impeller*** combination .

# 2.0 LITERATURE REVIEW .

## *2.1 Introduction .*

This section defines the main points of interest in the pump design used in the present study : an introduction to cavitation, inducers and impellers is given in the context of the pump design shown in Fig. 2. As will be seen, this design is consistent with a modern trend to the tandem inducer/impeller configuration for the first stage of rocket pumps .

### 2.1.1 Cavitation .

As a result of the combined effects of reduced tank pressures and increased rotation speed, cavitation is often likely to occur in the first stage of the turbopump. Cavitation can be described as the formation of vapor bubbles or pockets that develop as the fluid pressure falls below a certain value. Fluid vaporization at the fluid/vapor interface essentially occurs at constant temperature, starting at the blade leading edge. The critical pressure $p_{crit}$ below which cavitation develops depends on the vapor pressure of the fluid (for a given fluid temperature), the turbulence intensity, the presence of undissolved gas particles and impurities, and the thermodynamic effect of the fluid considered. Basically, the thermodynamic effect [1] delays cavitation inception. Vaporization needs heat to occur, which it takes from the bulk fluid. In the fluid close to the surfaces of cavitation, the temperature drops and therefore decreases the vapor pressure. Cavitation inception occurs at this critical pressure $p_{crit}$ smaller than $p_{vap}(T)$, even though simplistic approaches often keep $p_{crit} = p_{vap}(T)$ .

Extensive work has been performed in turbomachines (pumps and turbines) on cavitation, in order to better understand and control its development. Whereas cavitation inception has relatively mild consequences, further increases of the phenomenon can lead to blade erosion, rotordynamic instabilities, strong performance decreases (head, efficiency) and, in the worst cases, pump failure .

* The pertinent parameter used to characterize the occurrence of cavitation is the Net Positive Suction Head (NPSH) defined by :

$$\mathrm{NPSH} = \frac{P_{total,inlet} - P_{vap}(T_{fluid})}{\rho g} \tag{2.1}$$

It represents the available total pressure at the pump inlet to prevent it from cavitating. It is often used to represent pump performance characteristics with respect to cavitation increase. For good working conditions of the pump, the available NPSH has to be greater than the required NPSH which depends only on the pump and the working conditions. Figure 3 shows how cavitation can influence the head rise generated by an inducer [2] .

* The suction performance of a pump stage is characterized by the suction specific speed $S_s$ defined by :

$$S_s = \frac{N\sqrt{Q}}{NPSH^{3/4}} \tag{2.2}$$

When suction specific speed is to be evaluated for an inducer, a corrected definition is used :

$$S_s' = \frac{S_s}{\sqrt{1-\nu^2}} \tag{2.3}$$

where $\nu$ is the hub-to-tip ratio at the inducer inlet :

$$\nu = \frac{D_{hub1}}{D_{tip1}} \tag{2.4}$$

$S_s'$ takes the presence of the inducer hub into account by increasing the flow rate to compensate for the area blocked by the hub. For rocket design, a low inlet total pressure is desired to minimize tank weight. Therefore, the available NPSH decreases and the goal for inducers is to have a high $S_s$. To get high $S_s$, designs are made with low flow coefficients $\phi = \frac{V_{ax}}{U_{tip}}$ [1]. Typical inducer flow coefficients are in the range [3]

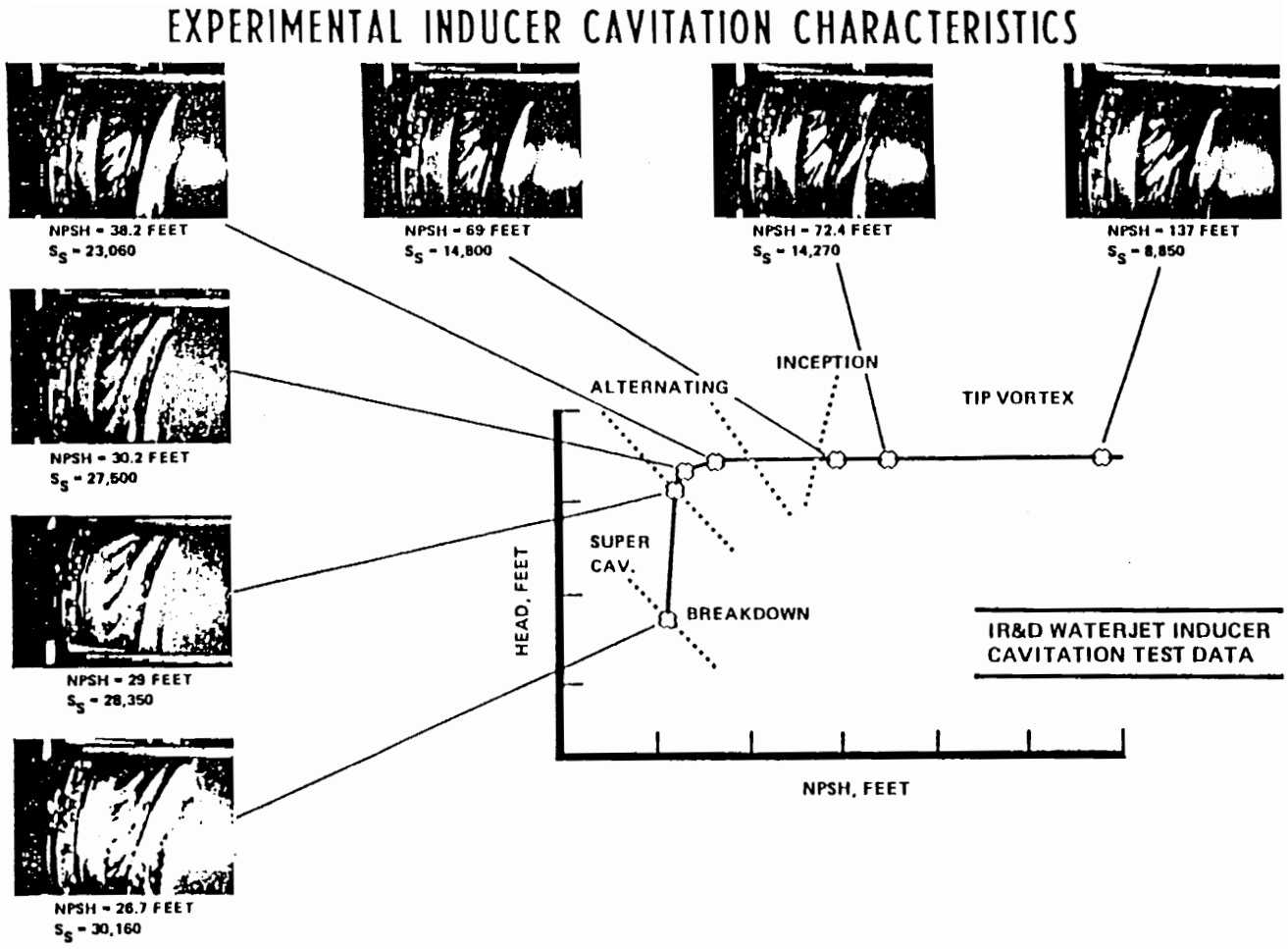


*Figure 3 : Cavitation influence on head-rise : Head vs. NPSH (from [2]) .*

$0.04 \leq \phi \leq 0.2$. Modern designs are more consistent with low $\phi$ values, typically 0.08 . As a consequence of low flow coefficients, the inducer inlet area must increase : the tip radius also increases whereas the hub radius decreases. In engineering units (rpm, gpm, ft), rocket engines typically run with $S_s$ from 15,000 to 50,000 .

## 2.1.2 Inducers .

Inducers are axial-flow pumps used as the first stage of the turbopump. They generally run at the same speed as the whole pump. Their particular design results from the requirement that they have high suction specific speeds, i.e. they are able to pump fluids with low NPSH. They are designed to withstand cavitation that inevitably develops because of low NPSH and high rotation rates. Inducers have to provide enough head rise so that cavitation does not extend beyond half the channel length [1]. This requirement is essential in providing good working conditions for the following blade rows which are not designed to withstand cavitation, and thus have poor performance if the inducer does not meet its objectives. Also, the inducer must be designed to minimize weight and size .

### *2.1.2.1 Design .*

The inducer usually contains 3 to 5 high-solidity (large chord-to-spacing ratio) blades which define long and narrow passages to provide time and space for the cavitation bubbles to collapse, and the pressure to increase. The blades usually wrap around about 300 degrees and have very sharp leading and trailing edges. The leading edges are also very thin and have optimized incidence angles to minimize the local static pressure drop in the fluid. Because inducers have low flow coefficients [1], they have correspondingly large stagger angles (typically 70 to 85 degrees). Together, these characteristics allow inducers to have high suction specific speeds .

Jakobsen [3] gave an extensive state-of-the-art review of inducers in 1971. He classified them according to head-rise capability and also according to the shape of the meridional flow path .

_ *head-rise :* inducers are divided into low head ($\Psi \leq 0.15$) or high head ($\Psi > 0.15$) inducers. $\Psi$ is the head coefficient defined by :

$$\Psi = \frac{gH}{U_{tip}^2} \tag{2.5}$$

The head-rise capability is a function [3] of blade geometry : low-head inducer blades are either flat-plate or flat-plate plus modified helix (depending on hub-tip contours and the $\Psi$ value). High-head inducer blades are a combination of flat-plate, modified helix and vortex-type .

_ *shape :* inducers are classified according to their meridional cross section and are divided into four basic types : (1) cylindrical tip and hub; (2) cylindrical tip, tapered hub; (3) tapered tip and hub and (4) shrouded. Figure 4 gives six examples of basic inducer types : (a) to (d) are low-head inducers whereas (e) and (f) are high-head inducers. Note all the inducers except (c) maintain a constant tip diameter at the inlet for an axial length corresponding to a solidity of 1 or higher. This design practice benefits the suction performance by maintaining optimum conditions until the blade cavity has collapsed. All the cases, except (a), have a ramped hub contour and a reduction in passage height through the inducer. This reduces the tendency of the hub flow to stall at the inducer exit. It is interesting to see that cases (a) to (d), even though they have low-heads, are used in combination with a tandem impeller. Data relative to these inducers [3] shows that low-head inducers have a hub-to-tip ratio at inlet ranging from 0.2 to 0.3. High-head inducers have hub-to-tip ratios of the order of 0.4 .

In his review, Jakobsen also gives very specific details on the inducer design, covering passage design, hub size and shape, blade characteristics (number, profile, thickness, sweep, cant, lead, solidity), fluid thermodynamic effect, cavitation, clearance, surface finish as well as materials. Similar work can be found in [4] .

Current designs are all high-head stages in order to provide a larger part of the pressure rise for the turbopump. Thus, requirements may be allowed to be less restrictive on the following blade rows of the pump. The inducer presented in section 1.0 and studied in this thesis is a high-head inducer, with cylindrical tip and tapered hub .

#### *2.1.2.2 Inducer flow field .*

Inducer flow investigations were first carried out in cryogenic fluids [5,6], but costs and inconveniences mostly caused experiments to be conducted with other fluids. Even though qualitative results are obtained, the flow physics is very well reproduced. Air is usually used when viscous turbulent effects or secondary flows are investigated. When cavitation needs to be studied, water is generally used and gives satisfactory results. However, because of the thermodynamic effect observed in current propellants

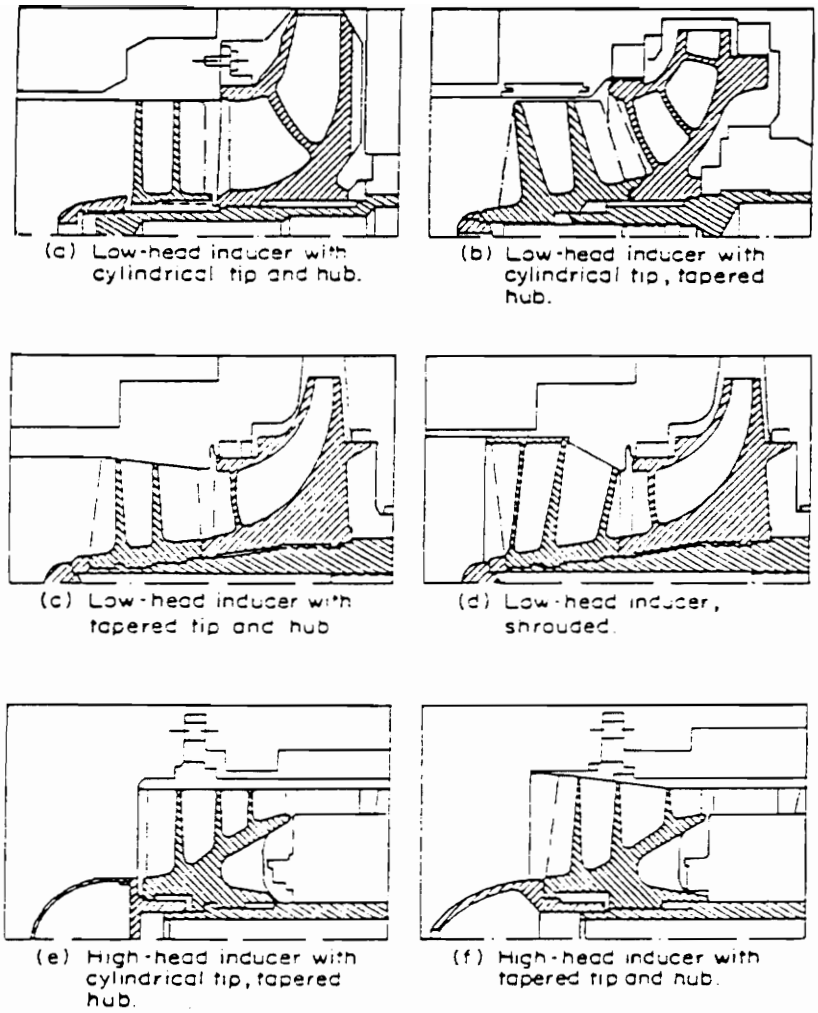


*Figure 4 : Basic inducer types (from [3]) .*

(liquid hydrogen), further sophistication is required and special fluids like Freon are utilized .

Experimental investigations in inducers started in the late 1950's [5-9]. Later, Lashminarayana [10-13] contributed extensively to analytical and experimental research on inducer flow fields. His review [14] provides a very complete summary of the knowledge about inducers flows. Prediction methods are given with ever increasing complexity (radial equilibrium, meridional solution with viscous effects, approximate viscous analysis based on shear pumping effect, 3D inviscid exact solutions, and 3D viscous study). Extended results from experiments are given and detailed investigations are discussed. Out of his results, several conclusions can be drawn on flows in inducers :

_ " real fluid effects are at least equally important to the ideal fluid effects" : the long and narrow passages of the inducer, associated with tip gap flow, generate a highly viscous and turbulent flow .

_ "secondary flow and other interaction effects near the end-wall regions" are very important, causing the flow to be highly three-dimensional, as seen in Fig. 5. Radial velocities are seen to be of the same order of magnitude as axial velocities .

_ "the inner part of the rotor (hub to mid-radius) can be designed from inviscid considerations" whereas 'the design of the outer part (mid-radius to tip) should take into account the shear pumping effects". This difference from hub to shroud depends on the tip gap flow and the high loss fluid that is centrifuged .

_ the total pressure rise is almost constant from hub to mid-radius, but then rises considerably until the shroud where measured pressures are much higher than the inviscid predicted values .

#### *2.1.2.3 Previous computational studies .*

Motivated by ever increasing computer capabilities (memory size and clock speed), computational methods for flows in turbomachinery have increased considerably over the past 15 years. Paradoxically, numerical investigations in inducers remain rather limited, at least in the literature. Lashminarayana [15] developed and tested an improved version of the code from [16], implementing viscous effects in the momentum equations.

Successful 3D turbulent calculations of inducer flow [17] and of tandem-bladed inducer flow [18] have been performed by the MEFP code developed by Moore [19]. The Moore Elliptic Flow Program was successfully used to predict, probably for the first time, the flow inside a rocket pump inducer [20]. Moore et al. [20] detailed the 3D flow and

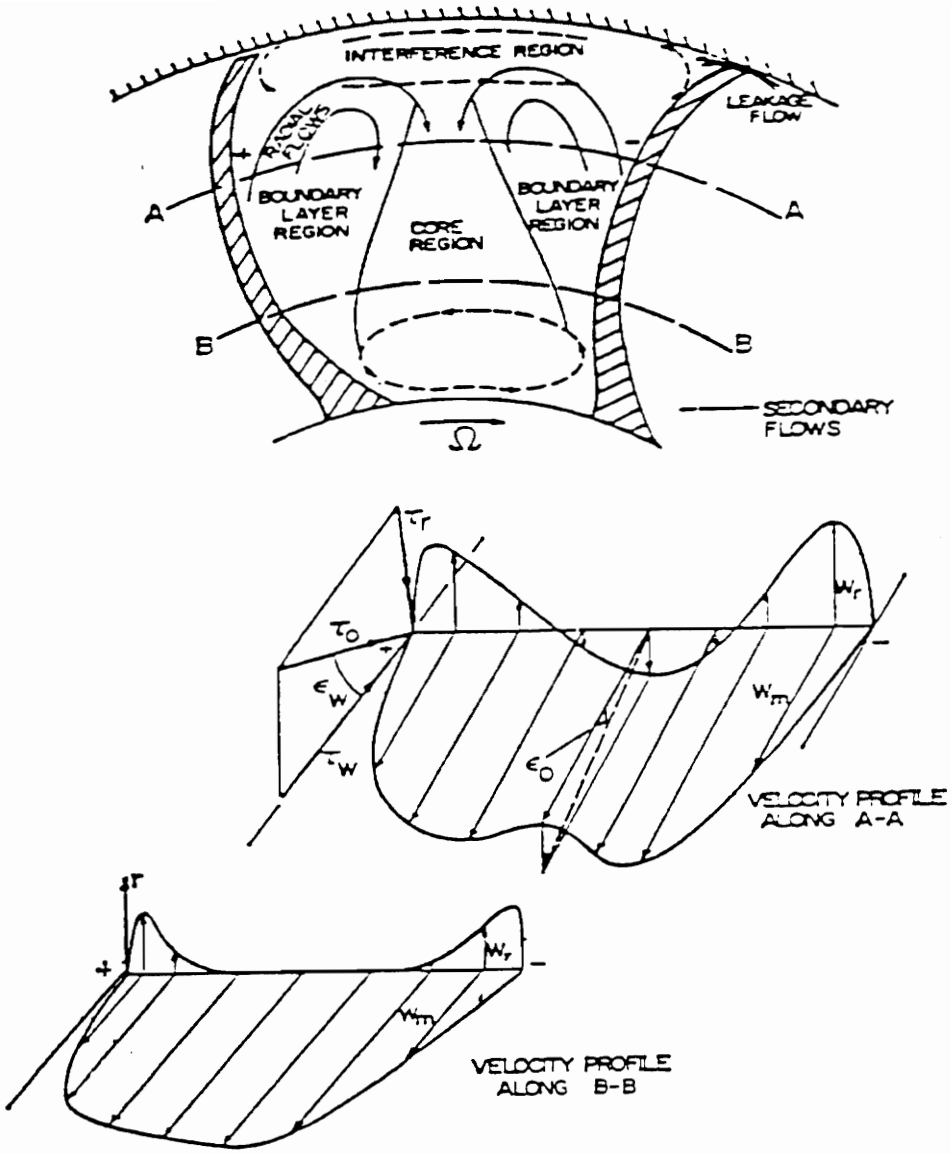


*Figure 5 : Qualitative nature of flow field inside inducer passages : secondary flows (from [14]) .*

performance of the French VULCAIN inducer. The meridional flow with tip leading edge vortex, the secondary velocity vectors, the losses and the tip leakage flow were shown, and the efficiency was predicted. More details can be found in [17] and section 2.3. Results give good agreement with experimental investigations from reference [21] .

More recently, Howard [22] attempted to obtain a 3D turbulent flow solution in a spiral inducer. Discrepancies between numerical and experimental results were mainly attributed to non-modeled tip-clearance effects, grid-dependent results, and choice of the turbulence model. However, Howard acknowledges the high complexity of the geometry (high stagger angle with axial inlet and outlet), leading to highly skewed grids (degradation in accuracy). El Ghazzani et al. [23] proposed a 3D inviscid flow calculation using a distributed loss model .

### 2.1.3 Impellers .

The specific speed $N_s$ is a useful parameter for classifying pump types because it indicates the probable optimum stage geometry. It defines the specific areas where the various pump configurations are best suited for the application. The specific speed is defined by :

$$N_s = \frac{N\sqrt{Q}}{H^{3/4}} \tag{2.6}$$

where :

N is the rotational speed, Q the volumetric flow rate and H is the head rise .

Again in engineering units (rpm, gpm, ft), rocket engine impellers typically have specific speeds in the range from 450 to 2100 .

Impellers are centrifugal pumps that convert the input shaft power into static pressure and kinetic energy. Impellers are required to give a high head rise at a low flow rate, generally with high efficiency (typically 90 to 95%). High head rises and low flow rates result in relatively low specific speed impellers. The latter are also required to minimize weight and size in modern turbopumps but, contrary to inducers, they are not designed to withstand cavitation. According to the desired required pressure for the combustion chamber, several impellers may have to be assembled in series (with turnaround channels in between) as in the SSME High Pressure Fuel Turbopump .

Flows in impellers remain complex because of several factors. An impeller inlet is axial but its exit is radial. Secondary flows, separation, 3D boundary layers, shroud leakage are common problems encountered in impellers. Probably because they were

used earlier, impellers have been more thoroughly studied than inducers. Extensive work can be found in the literature in terms of design techniques, experimental investigations or computational studies of impeller flows alone. But little work is available on detailed impeller performance in combination with an upstream axial inducer .

#### *2.1.3.1 Classification .*

The purpose of this section is to present the major concerns that were involved in the design and the flow analysis of the present impeller. Going into extensive details is well beyond the scope of this thesis .
Impeller designs can be classified in several categories using different criteria :

*1) Shrouded / unshrouded impellers :*

Figure 6.a shows a typical view of both shrouded and unshrouded configurations [4]. Choosing one or the other is a careful compromise between hydrodynamic performance and manufacturing considerations. Hydrodynamics depends on :

_ the rotational speed and the flow rate,
_ the shrouded impeller seal leakage vs. non-shrouded blade clearance losses,
_ reduced head coefficient due to friction losses on the stationary shroud for open impellers .

Shrouded impellers should be selected for maximum efficiency, absence of rubbing (except at the shroud seal) and minimum pump weight [4]. Open face impellers should be selected when tip speeds above 600m/s (2000 ft/s) are required, because shrouded impellers would have increased centrifugal stresses.

Relative performance of the two configurations are given in Fig. 6.b in terms of head and efficiency. Shrouded impellers seem to have higher efficiencies than open impellers for clearances greater than 3%. It also appears that they may produce higher pressure rise than open impellers for clearances greater than about 2%. The efficiency drop in unshrouded impellers seems to be due [24] to tip leakage flow losses. Also, the clearance produces reverse flows at the impeller leading edge, causing the inlet boundary layer to thicken. Shrouded impellers are widely used for small machines because clearance can become large and difficult to control. Unshrouded impellers are easier to

Shrouded titanium impeller - J-2S

Open-face titanium impeller-XLR129

(a) Configurations

(b) Performance

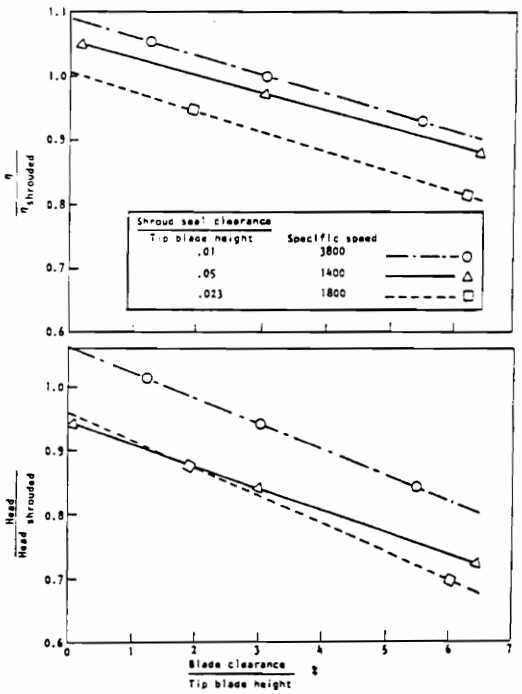


*Figure 6 : Shrouded/unshrouded impellers and their relative performance (from [4]).*

machine. They require thicker blades to withstand deformation, during operating conditions, due to possible rubbing and centrifugal stresses .

From a rotordynamics point of view, unshrouded impellers may have rotor side loads (if the clearance is too small) or generate heat and metal particles. Shrouded impellers permit larger axial and radial clearances except at the inlet shroud seal .

*2) Head coefficient :*

Impeller head coefficients in rocket pumps can have a wide range of values depending on the flow rate, the required suction performance and efficiency, and the head-vs.-flow slope. Centrifugal pump head coefficients typically vary [4] between 0.35 to more than 0.70. High head coefficient impellers are generally used in low specific speed applications to maximize efficiency .

American turbopumps have achieved maximum head coefficients [25] of 0.62 for the Mark 19 LH2 pump of the X-8 engine, and 0.67 for the Mark 3 RP-1 pump of the Atlas and H-1 engines. American designs do not attempt [25] to achieve higher coefficients because the pump head-flow characteristic tends to become very flat at high coefficients, which is detrimental to the engine system stability .

The Japanese are currently developing high head impellers, with an estimated coefficient of 0.65 for the LE7 hydrogen pump [25]. This centrifugal pump produces a head about 3050m (10,000 ft) higher than the SSME HPFTP (66,700 ft). Several high head pumps were successfully tested in Japan [26] .

*3) Blade number and exit angle :*

Low head coefficient impellers are designed with a small number of blades (3 to 5) whereas higher heads require many blades (20 to 60). Current designs [4] are in the 6 to 48 range, generally with a small number of inlet blades (8 or less), but with additional splitter blades. The latter improve flow range [4] by reducing the boundary layer thickness that exists with all full blades. Splitters are used to meet the design head coefficient. The number of blades is a function of head and flow rate. High head impellers often use splitters to avoid blockage at the inlet. For constant head, more impeller blades are required if the impeller discharge flow rate is decreased (slip at the impeller exit) .

Impellers can also be defined by their exit blade angles. Discharge blade angles for rocket impellers usually range from 22.5 to 90 degrees. Impellers with $\beta_2$=90 degrees have radially-ending vanes while those with $\beta_2$<90 have backswept blades. Typical exit angles for current high-head coefficient impellers are $\beta_2$=45 degrees or larger. The

Japanese LH2 pump for the LE-7 engine had $\beta_2$=60 degrees, but this was later increased to 70 degrees in real engine working conditions to gain additional head rise [25]. Backswept impellers with high head coefficient have been found to have a wider high-efficiency range with flow rate than low head impellers [4] .

*4) Impeller tip-speed :*

Classification of impellers [27] defines high tip speed impellers as those with $U_2$ > 300 m/s (1000 ft/s). The tip-speed limit depends on the impeller type (shrouded or not), the manufacturing process (cast or forged) and the materials used. It is a function of blade stress (centrifugal and fluid effects ; higher density fluids require lower tip speed) and blade exit angles. Reference [4] suggested a higher limit value of 425 m/s (1400 ft/s) in 1973, while impellers had been successfully tested with tip speeds up to 875 m/s. Current designs are however more in the range 500 to 600 m/s. The LE7 hydrogen impeller has been estimated [25] to run at a speed of 610 m/s ; the LE7 oxygen impeller runs at 205 m/s .

### *2.1.3.2 Design .*

The design of impellers must produce geometries that are stress resistant, easy to manufacture, and have high aerodynamic performance (no separation). Design procedures for impellers have essentially evolved with computers .

* Formerly, designs were made using an indirect approach. A one-dimensional flow analysis was performed to find the overall dimensions. Empirical charts and knowledge-bases from manufacturers were often used. A general 1D procedure can be found in [4]. Based on these dimensions, a full 3D description of the blades was produced. Modifications of the geometry with successive aerodynamic analyses then occurred. Improvements to the blade geometry were made until the process converged to give a satisfactory design. This indirect approach was very expensive and time consuming .

* Modern designs use a direct approach. It consists in a 3D procedure that directly gives the designed impeller coordinates. The latter can be used on a numerically-controlled machine and produce the final impeller. Several authors have dealt with inverse design techniques [28-32]. The main idea is to adopt a "prescribed blade loading"

[28] which consists in imposing the relative velocity distribution for the pressure side, PS, and the suction side, SS, of the blades. Blade loading techniques can be found in [30]. The distribution must avoid strong velocity decreases which can cause separation. Using the hub and shroud shape (given), the meridional flow is computed using a stream function [31]. Blockages due to the blades and to aerodynamics are taken into account. Using the continuity equation, the tangential velocity is computed. The blade shape is obtained by the inviscid slip condition : the blade must follow the flow. Two different ways can be used to take viscous effects into account : introduction of the aerodynamic blockage throughout the meridional geometry or introduction of a vorticity term related to entropy gradient [31]. The second solution gives much better results. The method is valid for main blades and for splitters .

* The ultimate step of modern design is the use of 3D viscous flow calculations to check the correct design of the impeller and to suggest possible improvements for the redesign. This is the subject of this thesis. Casey et al. [32] give a very good example of this step. Two 3D viscous codes (LOSS3D from Denton, and the Dawes BTOB3D) were used to predict the flow in the Eckardt centrifugal compressor impeller "B". Very good agreement was achieved. Automatic pre- and post-processing enable a flow calculation to be performed, analyzed and evaluated in terms of impeller quality. At the same time, much insight into the flow physics is gained .

## *2.2 Inducer / impeller configurations .*

The previous section detailed the inducer and impeller characteristics separately. In practice, both components are assembled with the inducer feeding the impeller with a pressurized fluid, free of cavitation (ideally) .

### 2.2.1 The different matching solutions .

The inducer/impeller matching can be done in several ways .

#### *2.2.1.1 Separate shafts configuration .*

The inducer and the impeller stages are mounted on two different stages and have their own turbine. This situation can be found (Fig. 7) in the SSME fuel turbopumps [33,34]. An identical configuration is displayed in the oxygen turbopumps. The Low Pressure Fuel TurboPump (inducer driven by a two stage turbine) and the HPFTP (3-stage centrifugal pump driven by a two-stage turbine) run at different speeds to optimize efficiencies and weight. The object of such a disposition is also the improved flow at the impeller inlet due to the optimized low pressure diffuser .

#### *2.2.1.2 In-between inducer/impeller stator vane configuration .*

The inducer and the impeller are mounted on the same shaft driven by one turbine or more. Between the two elements, a stator segment is added with dual purpose of:
_ providing radial support for the pump end bearings,
_ guiding the flow at the proper incidence angle to the first stage impeller .
Such a configuration can be found in [35] in the Rocketdyne hydrogen turbopump ("Advanced Development Program" concept), as seen on Fig. 8 .
Similar dispositions also exist in the SEP turbopumps for the VULCAIN engine .

#### *2.2.1.3 Integral inducer/impeller configuration .*

In this concept, the blading is continuous from the inducer leading edge to the impeller trailing edge, with no inter-row gap in-between. Figure 9 shows a typical

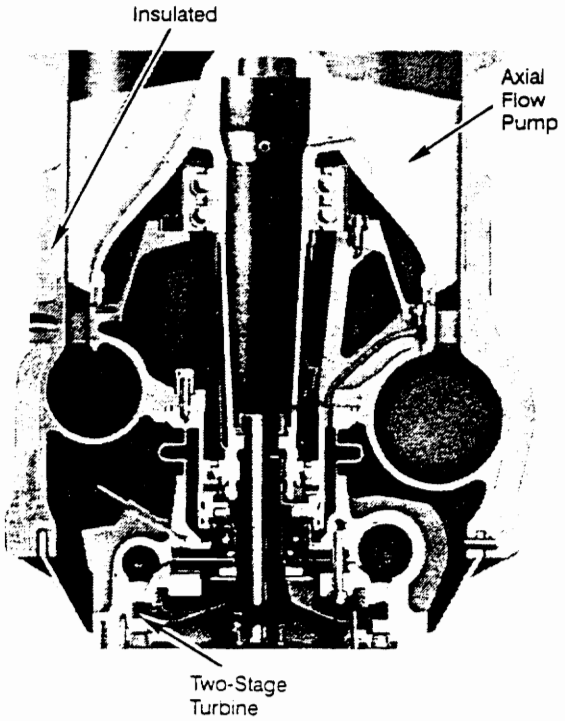


| Key Performance Parameters | FPL (109%) |
|---|---|
| Pump inlet flow rate (lb/s) | 161.9 |
| Pump inlet pressure (psia) | 30 |
| Pump discharge pressure (psia) | 306 |
| Pump efficiency | 0.749 |
| Turbine flow rate (lb/s) | 30 |
| Turbine inlet temperature (°R) | 479 |
| Turbine pressure ratio | 1.34 |
| Turbine efficiency | 0.530 |
| Turbine speed (rpm) | 16,720 |
| Turbine horsepower | 3,520 |

Diameter: 19.1 in.
Length: 18.2 in.
Weight: 177 lb

**SSME low pressure fuel turbopump.**

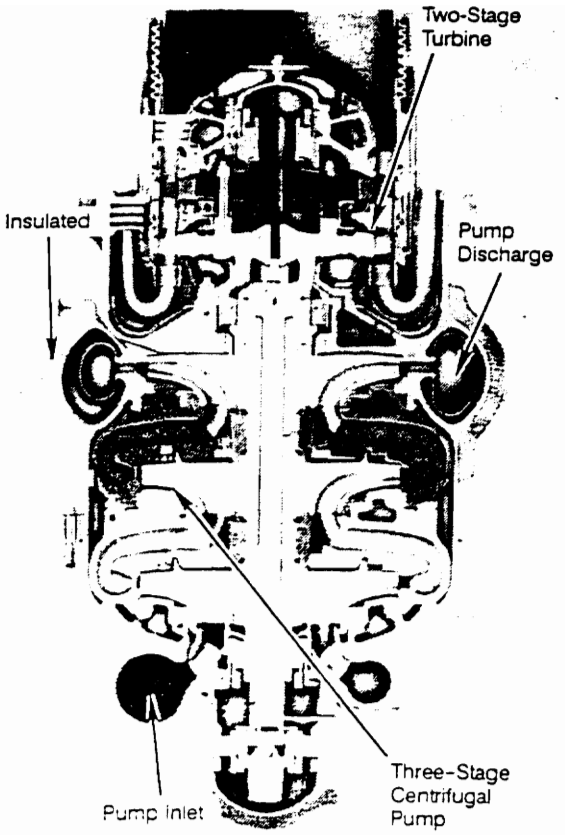


| Key Performance Parameters | FPL (109%) |
|---|---|
| Pump inlet flow rate (lb/s) | 162.5 |
| Pump inlet pressure (psia) | 238 |
| Pump discharge pressure (psia) | 6,872 |
| Pump efficiency | 0.760 |
| Turbine flow rate (lb/s) | 178 |
| Turbine inlet temperature (°R) | 1900 |
| Turbine pressure ratio | 1.400 |
| Turbine efficiency | 0.842 |
| Turbine speed (rpm) | 36,600 |
| Turbine horsepower | 74,900 |

Diameter: 21.7 in.
Length: 37.8 in.
Weight: 775 lb

**SSME high pressure fuel turbopump.**

*Figure 7 : Low and High pressure fuel turbopumps in the SSME (from [36]) .*

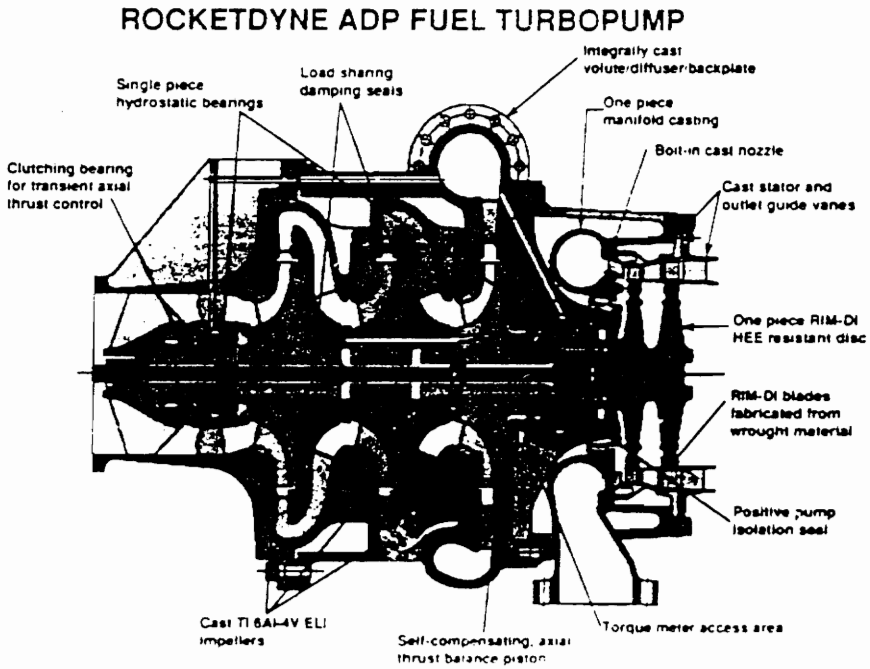


Rocketdyne $LH_2$ Turbopump Mechanical Arrangement

*Figure 8 : Rocketdyne ADP fuel turbopump (from [35]) .*

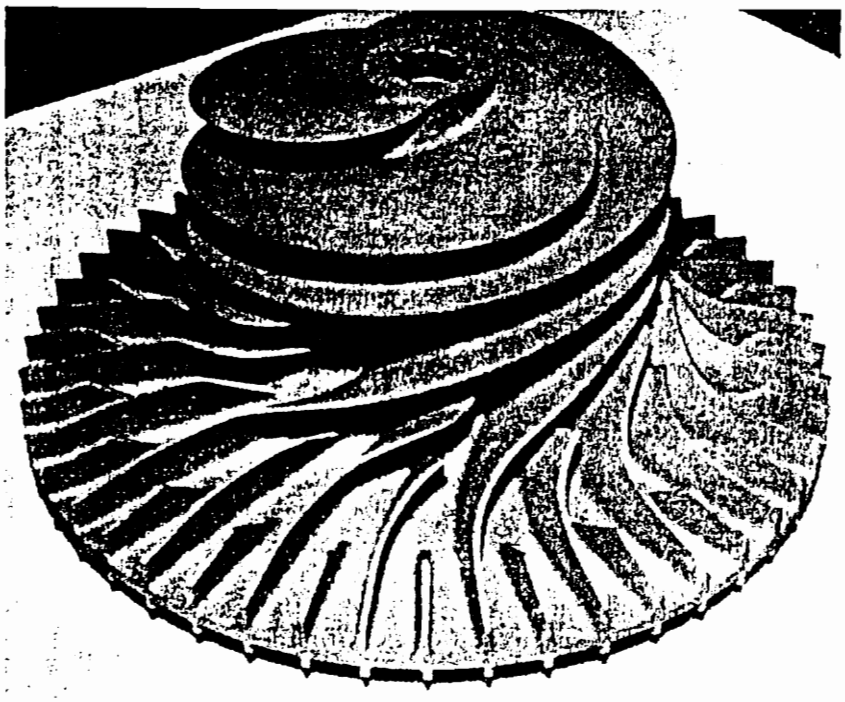

—*Typical unshrouded $LH_2$ pump impeller (NERVA I).*

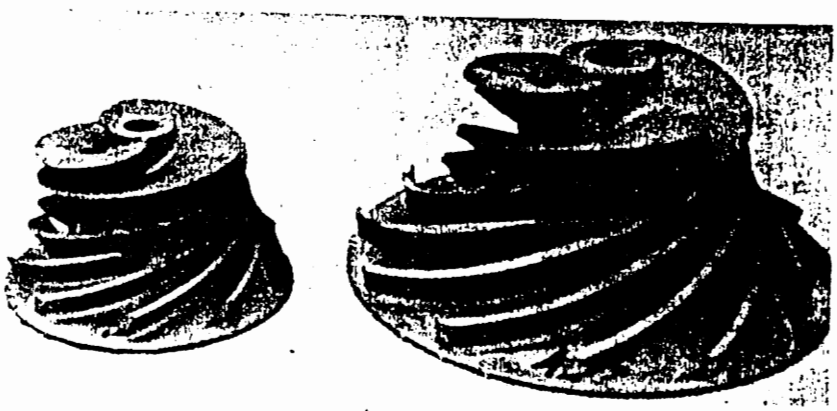

—*Typical conventional density propellant impellers (Titan II).*

***Figure 9 : Integral inducer / impeller (from [27]) .***

example. Campbell et al. [27] suggested that higher efficiencies might be obtained at lower specific speeds for non-shrouded impellers. Even though shrouded impellers are more efficient at high specific speed, an integral inducer / shrouded impeller is not possible because of acute manufacturing problems [4]. Even if open impellers have fabrication and stress advantages, the concept requires increasing shroud clearances to avoid rubbing, but efficiency may drop (see Fig. 5.b) .

#### *2.2.1.4 Tandem inducer/impeller configuration .*

Both elements are mounted on the same shaft, with no stator but a vaneless gap in-between. Advantages and details about this configuration are given in section 2.2.2 . Figure 10 displays several former design cases found in the literature [36]. The earliest turbopumps (cases (a) and (b)) in the Jupiter, Thor, Atlas boosters and the Atlas sustainer needed heavy speed-reduction gear boxes because the speeds of the pumps and turbines were optimized independently. Improvements on the canted inducer (c) enabled the turbine and the pump to run at the same speed on a common shaft. The J-2 engine was the first gas generator cycle to use LH2 and LO2. Because of the small density of hydrogen, separate pumps were required for the hydrogen and the higher density oxygen because the hydrogen turbopump needed to be run at much higher speed. The J-2 TPLO2 (d) was of the tandem type whereas the TPLH2 was a long and heavy axial pump. It can be noted that early tandem technology involved oxygen turbopumps only. Though no specific reason was given, it is believed that suction performance, stress considerations and severe requirements on materials were the reasons why the high speed TPLH2 could not be designed [36] with a tandem inducer/impeller .

Current modern designs (Fig. 11) now also involve tandem geometries in hydrogen pumps, as seen in cases (e) and (f). The two Japanese LH2 turbopumps (LE5 and LE7) are based on this concept as well as the two oxygen turbopumps designed for these two engines. The Aerojet solution for the ALS ("Advanced Launch System) hydrogen turbopump belongs to this configuration, as well as the improved version [37] of the Rocketdyne ADP concept (i.e., Fig. 8 without stator) .

No tandem inducer / unshrouded impeller design (with inter-row gap) was found in the literature .

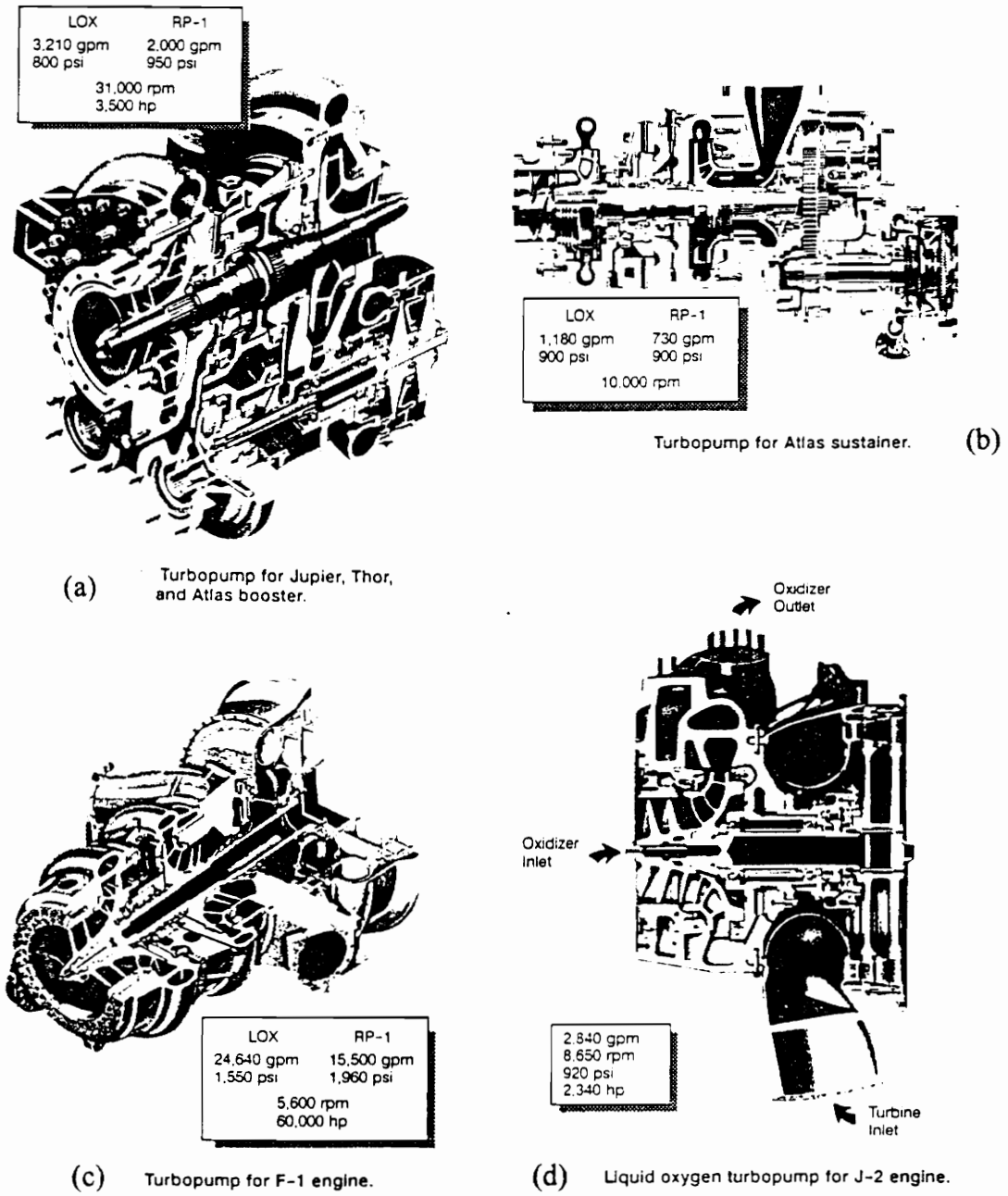


*Figure 10 : Evolution of the Tandem inducer / impeller configuration - Part A . (from [36]) .*

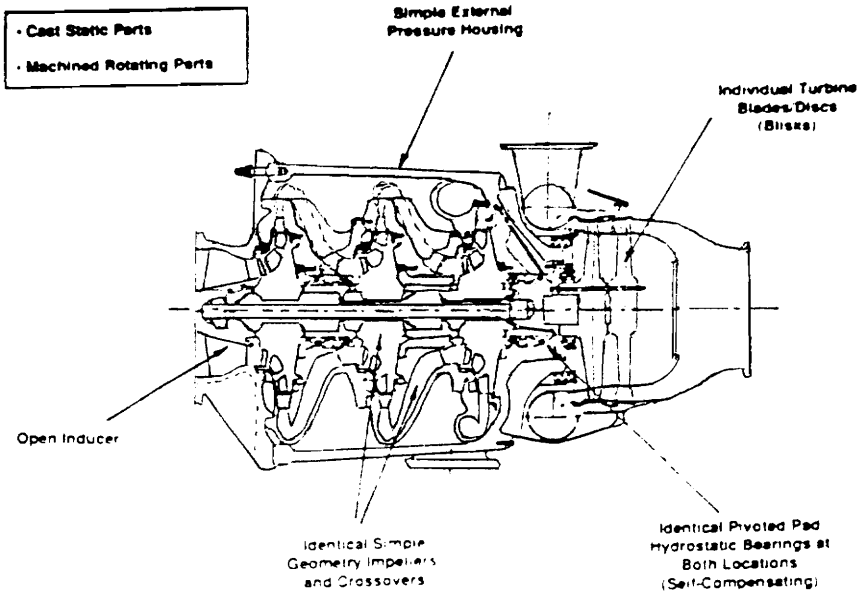


(e) Aerojet Fuel Turbopump Configuration

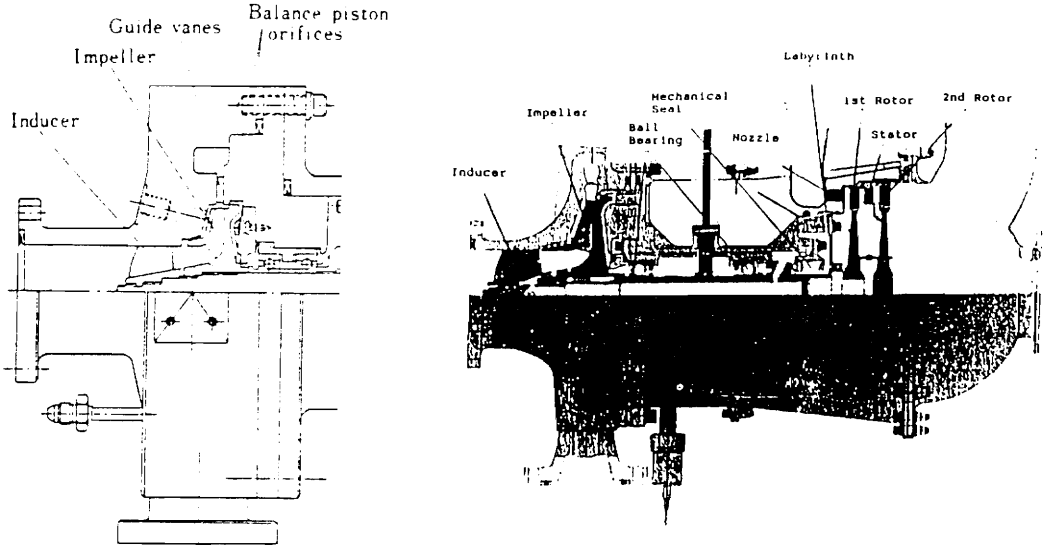


(f) LE-5 Liquid Hydrogen Turbopump

***Figure 11 : Evolution of the Tandem inducer / impeller configuration - Part B . (from [35] and [25]) .***

## 2.2.2 Details about the tandem inducer/impeller combination .

### *2.2.2.1 Advantages .*

_ The separate blade configuration has better performance at higher suction specific speeds [27] .

_ For identical specific speeds $N_s$ , a tandem design can have suction specific speeds as high as 4 times that of the same impeller alone [5] .

_ The blading discontinuity has several advantages :

* the blade boundary layers are not continuous after the inducer trailing edge, TE. Boundary layers in the impeller are therefore thinner, and are thus less likely to cause separation in that stage. This is the main reason why tandem blades have been investigated for impellers. Also, higher blade loadings can be achieved .

* operation at high speeds gives identical performance to conventional designs, but low speed working conditions have better pump performance. Therefore, a wide range of operating conditions can be achieved, as clearly explained by Grohmann [38] .

* the tandem design improves the operating range, the efficiency, cavitation behavior and suction performance .

Grohmann [38] provides a good discussion of the current interest in the tandem configuration :

_ the inducer low NPSH and sufficient head rise favors suction performance and increases the impeller safety margins with respect to cavitation,

_ the tandem geometry has smoother and safer operating conditions than impeller-alone designs because the inducer lowers the required NPSH of the whole pump,

_ even though inducer and impeller are designed with quite different objectives, their disadvantages cancel out when they are assembled. Their advantages reinforce, as can be seen in Table 1 (from [38]) :

***Table 1 : Advantages of the combined inducer/impeller (from [38]) .***

| | Head | NPSH | Efficiency |
|---|---|---|---|
| Impeller | high | high | high |
| Inducer | low | low | low |
| Inducer+Impeller | high | low | high |

#### *2.2.2.2 Flow investigations .*

*1) Experimental :*

Finally, the most interesting experimental results come from investigations done by the Japanese [26] for a new generation of high performance pumps. Eight different pumps are reviewed in terms of performance (efficiency, head, NPSH) with flow rate. The authors' main results showed that higher pump efficiencies were obtained in the range of small stage specific speeds compared with previously reported results. This tendency was particularly remarkable with two-stage centrifugal pumps .

*2) Numerical :*

No numerical investigations were found for the tandem inducer/impeller configuration. The study in this thesis is apparently the first for a rocket pump .

Calculations with tandem blades at the inlet of a centrifugal compressor impeller were performed by Josuhn-Kadner et al. [39]. But their geometry was not that of a tandem inducer/impeller, and their code is very restrictive. The tandem rotors must have the same number of blades and zero axial clearance in-between. Extension to splitters and axial clearances needs more development. Rotors moving relative to one another are scheduled for the next level of their code .

## *2.3 Previous computations for the VULCAIN inducer .*

For three successive computational flow analyses, the MEFP code has been used for computations with ever increasing geometric complexity in SEP pumps. LeFur [17] and Moore et al. [20] performed the first 3D turbulent rocket pump inducer calculation with a Navier-Stokes code. A few years later, Excoffon [18] used MEFP to solve for the first time the flow inside the tandem bladed inducer of the VULCAIN engine (stage similar to the SSME LPOTP). With the research undertaken in this thesis, MEFP is also used for a first calculation of its type by solving the 3D flow in a tandem inducer/impeller.

Before presenting the results relative to this configuration, the main conclusions of the two previous computations are recalled, even though the scopes are different. The previous calculations aimed at providing a CFD flow solution that could be compared with already available experimental air tests results. The objective of the present study is to evaluate the quality of the pump design in terms of its flow features. That way, improvements for a possible redesign may be suggested .

### 2.3.1 Inducer alone calculation [17] .

The main purposes of this calculation were :

_ to use MEFP on an inducer geometry very different from a compressor or a turbine, because of the high skewness of the grid (high stagger angles),

_ to provide insight into the 3D flow .

The results showed the 3D turbulent nature of the flow, as well as the performance of the four-bladed inducer. Figure 12 shows a meridional view of the velocity vectors at mid-passage, near the suction side, and near the pressure side. At mid-passage, the flow behaves rather smoothly. But a leading edge tip vortex can clearly be seen. Near the trailing edge, meridional velocities have a small radially inward component. On the pressure and suction sides, very strong radially outward velocities develop, with radial velocities of the same order of magnitude as axial velocities. Radial movement is caused by the centrifuging of the boundary layers, which is consistent with the flow described by Fig. 4. At the inducer tip, the leading edge vortex generates inlet flow recirculation with backwards velocities. On the pressure side, the tip leakage flow through the gap also has radially outwards velocities .

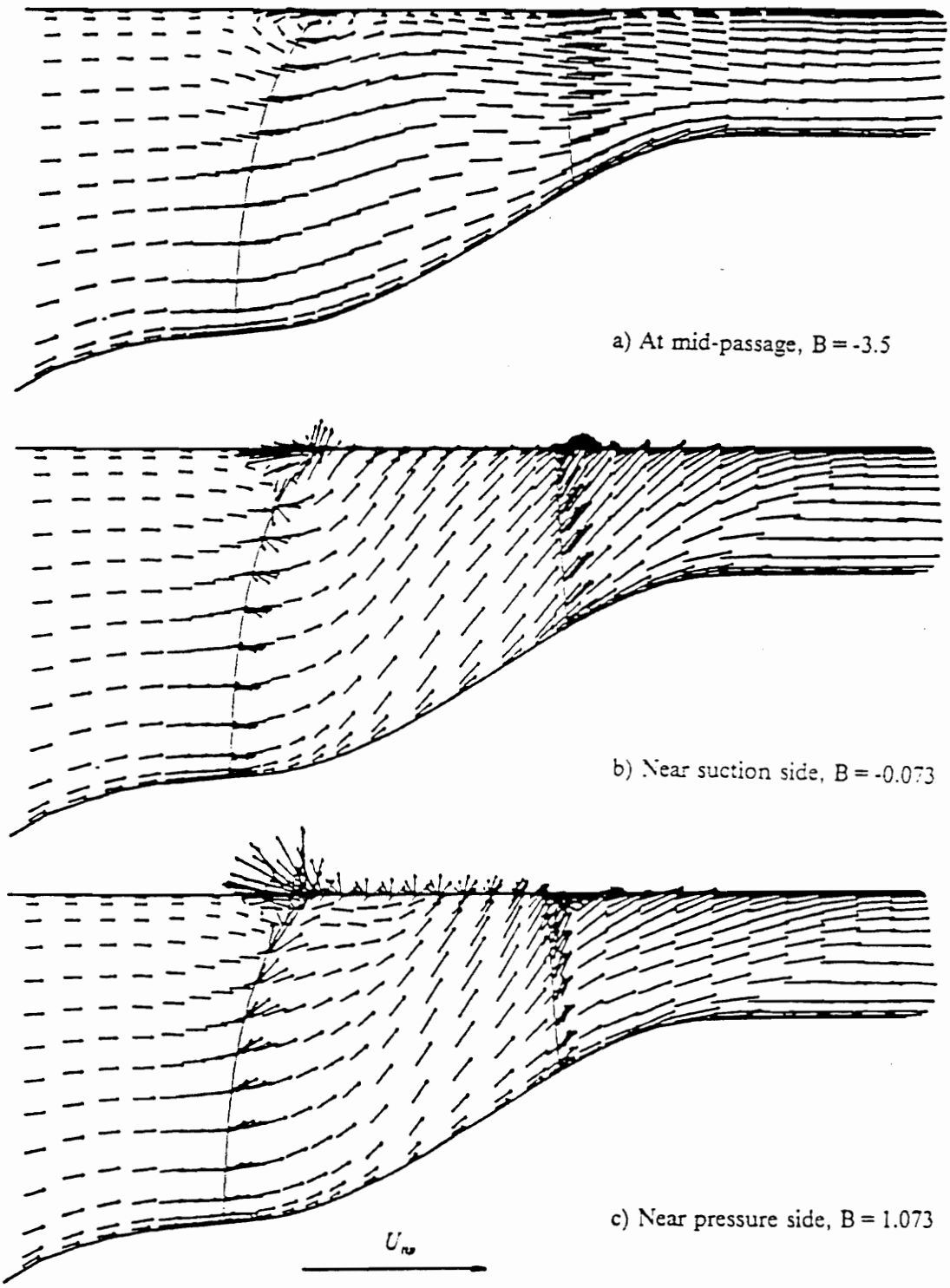


***Figure 12 : Velocity vectors on meridional views of the first blade (from [17]) .***

Similarly with the concern of knowing the nature of the flow at the inducer exit (as an input for the following stage), the radial hub-to-shroud loss distribution was computed (Fig. 13), showing very high losses in the outer half of the passage. The numerical predictions are also seen to have a very good agreement with the experimental data from [21] .

Consistently with section 2.1.2.2, losses are seen to be very low from hub to mid-height, and then increase almost linearly from mid-height to shroud. The calculation gives a clear idea of the flow distribution at the inlet of the second blade row .

### 2.3.2 Tandem bladed inducer calculation [18] .

Results for the tandem blade inducer (4 inducer blades and 12 second row blades) showed that :

_ no major difference occurred in the meridional inducer velocity field, but that the pressure distribution and the blade loading varied slightly. An increased reverse loading at the inducer TE can be noticed in the tandem bladed case with respect to the inducer alone. This can be seen in Fig. 14 .

_ the flow development was different in each passage, due to highly non-uniform flow at the second blade row inlet. The passage receiving the inducer mid-passage flow exhibited a fairly uniform 2D flow, whereas the other two passages were strongly influenced by the inducer wake .

_ the mass flow rate was nearly uniformly split in each of the three passages .

_ the blade loading was very similar for each blade of the second row .

_ the pressure rise was of the same order through each passage .

_ the flow after the second blade row was in radial equilibrium .

Again, a major conclusion from this study was the inducer exit flow distortion. This can be seen on Fig. 15. The radial distribution of the flow properties at the exit of the tandem bladed inducer is still highly non uniform, and it was concluded that the design of a stator able to handle this highly distorted flow might present some difficulties.

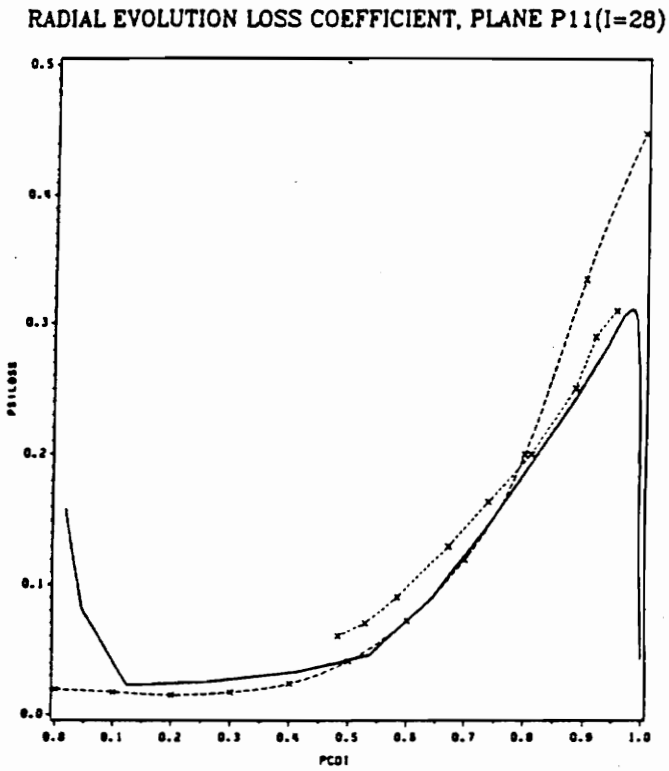


SEP Prototype (Measured).

SEP Prototype (Calculated).

NASA Inducer (Lakshminarayana).

$$PCDI = \frac{r - r_{hub}}{r_{shroud} - r_{hub}}$$

*Figure 13 : Radial distribution of losses at the inducer exit (from [17]) .*

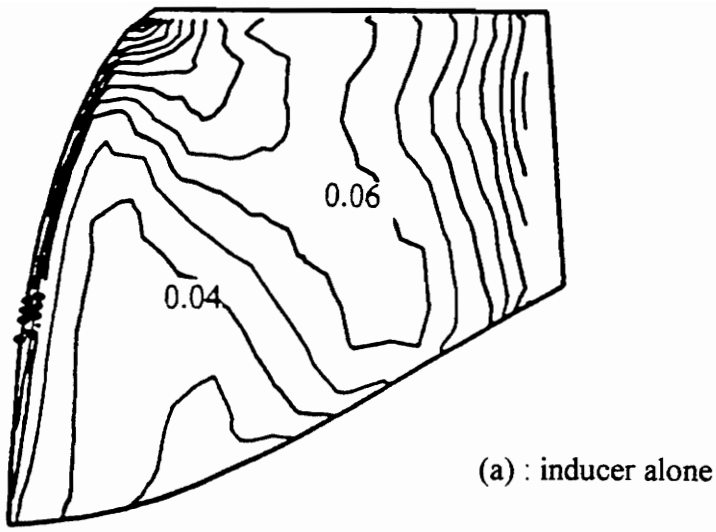


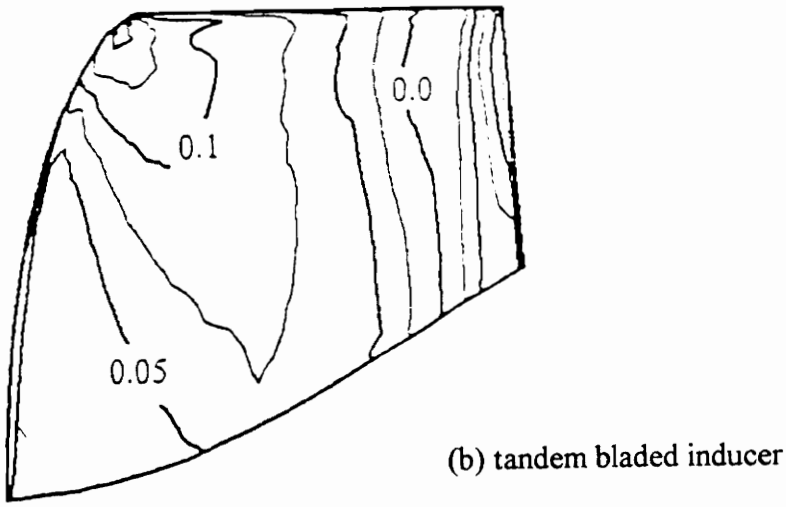


***Figure 14 : Comparison of the blade loadings for the inducer :***
***(a) : alone [17] and (b) : in the tandem bladed configuration [18].***

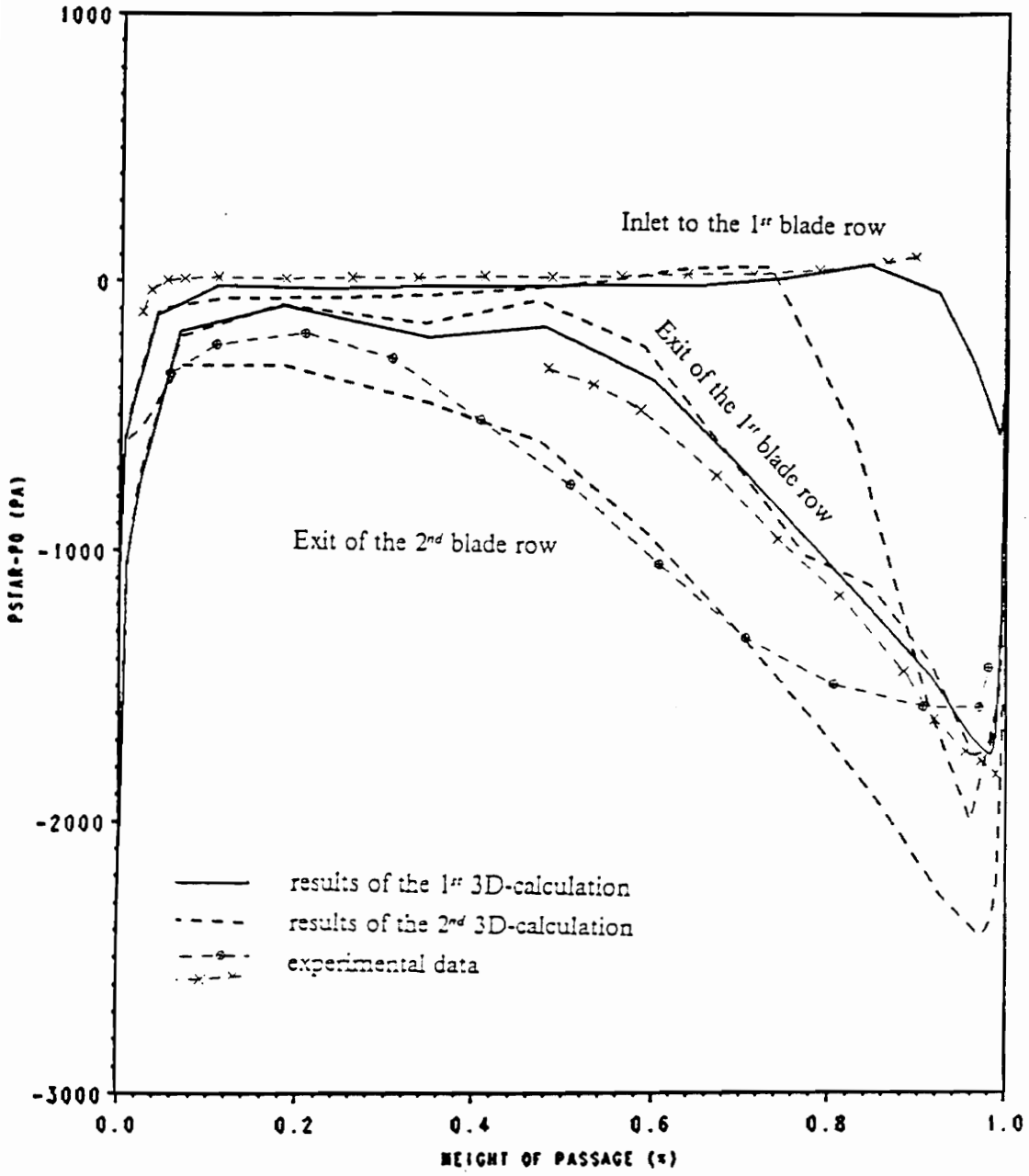


**Inlet and exit stations of the second blade - rotary stagnation pressure: $P^*$**

***Figure 15 : Radial distribution of losses in the tandem bladed inducer (from [18]) .***

## 2.4 *The Moore Elliptic Flow Program (MEFP).*

The Moore Elliptic Flow Program is written to handle steady turbulent compressible or incompressible flow in turbomachinery. The flow is described by the following Steady Flow Conservation Equations (written in the rotating reference frame, i.e. in terms of the relative velocity vector **W**) :

Mass :

$$\nabla \bullet \rho \mathbf{W} = 0 \tag{2.7}$$

Momentum :

$$\rho \mathbf{W} \bullet \nabla \mathbf{W} - \nabla \bullet \mu \nabla \mathbf{W} = \nabla \bullet \mu (\nabla \mathbf{W})^T - \nabla p - 2\rho \Omega x \mathbf{W} - \rho \Omega x (\Omega x \mathbf{r}) \tag{2.8}$$

Equation of state :

$$p = \rho RT \tag{2.9}$$

Rothalpy (energy) :

$$\rho \mathbf{W} \bullet \nabla H - \nabla \bullet \mu \nabla H = 0 \tag{2.10}$$

$$H = c_p T + \frac{1}{2}(\mathbf{W} \bullet \mathbf{W}) - \frac{1}{2}(\Omega x \mathbf{r}) \bullet (\Omega x \mathbf{r}) \tag{2.11}$$

Second law of thermodynamics :

$$s - s_0 = c_p \, ln(\frac{T}{T_0}) - R \, ln(\frac{P}{P_0}) \tag{2.12}$$

The momentum equation is used to solve for the three components of the relative velocity vector **W** ; the energy equation is used for the rothalpy H ; the definition of the rothalpy for the temperature T, and the second law equation for the entropy s. The Moore 3D viscous flow program is a pressure-correction calculation procedure, and thus, the continuity equation is used to solve for the pressure p while the equation of state gives the density ρ. In time-marching methods, the unsteady continuity equation gives the density and the equation of state the pressure .

For incompressible flows, only the mass and momentum equations are used, the state equation being replaced by ρ=constant .

For the turbulent flow calculation performed, the flow equations are coupled with a Prandtl mixing length model of turbulent viscosity, with a van Driest correction as described below :

$$\mu = \mu_{laminar} + \mu_{turbulent} \tag{2.13}$$

$$\mu_{turbulent} = \rho L^2 \frac{du}{dy} \tag{2.14}$$

with $$\frac{du}{dy} = \sqrt{(\nabla \mathbf{W} + (\nabla \mathbf{W})^T) : \nabla \mathbf{W}} \tag{2.15}$$

where L is the smaller of : 0.08 times the width of shear or boundary layer,
0.41 times distance to nearest wall .

van Driest correction : $$L = 0.41 y (1 - exp \frac{-y\sqrt{\rho\tau}}{26\mu_{laminar}}) \tag{2.16}$$

where y is the distance to the nearest wall .

Near-wall correction : $$\mu = \sqrt{\mu_{laminar}} \cdot \sqrt{\mu_{laminar} + \mu_{turbulent}} \tag{2.17}$$

MEFP uses an upwind control volume discretization for the momentum equations. The code uses an elliptic pressure correction solution procedure similar to the SIMPLER algorithm of Patankar. The discretization of the equations and the details of the application of the pressure-correction method for an elliptic calculation are given in Moore [19,40] .

The upwind control volume approach and mixing length turbulence model can be used over relatively coarse and non-uniform grids [19,40]. Grids are generally required to have spacing factors from one cell to the next of less than 5, preferably around 2. The aspect ratios of cells in the free streams are preferably less than 10 with some cells on each plane of the order of 1. The grid methodology, near-wall spacing and turbulence model are the same used for the previous studies by LeFur [17] and Excoffon [18]. For example, the near-wall grid spacing in the inducer was chosen to be one percent of blade-to-blade distance, the same as in the previous studies. These earlier studies both gave good agreement with the loss measurements downstream of the inducer and downstream of the tandem axial blade row (see Figs. 13 and 15) .

# 3.0 SCOPE AND OBJECTIVES OF THIS RESEARCH .

**The need for improved numerical methods for turbopump design .**

Producing reliable and high performance turbopumps with ever lower costs and manufacturing times requires very sophisticated design techniques. The development of 3D Navier-Stokes codes enables pump manufacturers to predict the flow inside their pumps without having to go through the expensive and time-consuming process of producing a prototype that will then have to be experimentally investigated. Working in that way, the flow in the tandem inducer/impeller design produced by SEP is computed using the Moore Elliptic Flow Program. This thesis studies the numerical investigations of flow field in this geometry. Emphasis is given to determine the possible design problems that might be encountered in the turbopump. In particular, attention will be given to the flow in the impeller. Possible stall inception will be investigated, as well as a proper flow split in the impeller passages. Also, the gap between the inducer and the impeller will be carefully studied in terms of interactions and matching between the two blade rows. Flow distortion at the inducer exit will be studied to better understand the impeller inlet flow .

**The calculation conditions .**

A turbulent full-3D flow calculation for the MCA tandem inducer/impeller geometry has been run at the nominal design flow conditions with liquid hydrogen. The calculation, performed in actual engine operating conditions (no similitude), also has the originality of being a high Reynolds number computation .

The flow calculations used a 3D elliptic procedure including viscous effects and developed by Joan G. Moore and John Moore at the Virginia Polytechnic Institute and State University. The code has been successfully tested on turbines, centrifugal compressors, and more recently, on inducers. This was the first time that such a highly complex geometry as the tandem inducer/impeller configuration was handled by the program, and no previous work of this type could be found in the literature .

**Analysis of the results .**

Several 3D flow calculations were performed for the MCA geometry. A calculation was first done for the tandem inducer/impeller combination itself. Two additional 3D calculations for the inducer-alone were then performed using two different inducer exit geometries. The flow in the inducer-alone cases will be compared with the inducer flow in the tandem geometry .

In the tandem inducer/impeller calculation, the general objective is to produce a detailed flow analysis inside the turbopump. The results should stand as a reference for future investigations. The results are studied in terms of velocity and pressure fields. From the study of pressure, a qualitative prediction of the regions where cavitation inception is likely to occur was performed .

In the inducer-alone calculations, the flow field in the inducer alone was investigated with two different exit geometries. An axial exit (similar to the VULCAIN engine) and a radial exit (the one from the tandem geometry) were compared to determine the influence of geometry on the inducer flow field. These two inducer calculations are then compared with the results from the inducer used in the tandem configuration (first calculation). This way, it is intended to expose the influence of the impeller on the inducer flow field, and determine if uncoupling the two elements (inducer and impeller) can be performed or not .

Finally, the most important results from these numerical investigations will be reviewed, with possible steps suggested for the turbopump redesign .

# 4.0 GENERATION of 3D FINITE DIFFERENCE CALCULATION GRIDS .

The successive steps for creating a 3D finite difference calculation grid for the tandem inducer/impeller configuration is first described. Using this 3D grid, two additional grids with fewer grid points are then derived for the inducer-alone geometries .

## *4.1 Data provided .*

The design made at Vernon, France, produced the basic geometry for the inducer/impeller combination shown in Fig. 2. The files available were :

_ a meridional definition of the hub and shroud contours for the whole pump,
_ a meridional 2D grid for the whole pump,
_ the inducer pressure and suction surfaces definition,
_ the impeller main blades PS and SS definition,
_ the impeller splitter blades PS and SS definition .

Considering the nature of the pump, the blades are defined in the cylindrical coordinates system (r,θ,z). The z-axis is the rotation axis oriented downstream. The tangential direction chosen defines a right-hand coordinate system .

Using the axisymmetry of the pump, only one inducer blade has to be defined. For each inducer blade, a set of 2 impeller main blades with 4 splitters (2 per main blade passage) corresponds .

### 4.1.1: The initial meridional 2D grid :

The initial 2D grid consists of 16 layers in the k-direction. Each layer is defined by 127 points in the i-direction. This grid contains the approximate locations of all the blade leading and trailing edges in a single grid. Therefore it will be used as the starting place for the construction of the 3D MEFP grid .

Figure 16 represents the meridional view of this 2D grid. The inducer is gridded from line i=16 to line i=40. The impeller main blade is gridded from i=46 to i=86, the splitter blades from i=59 to i=86, and the diffuser blades from i=92 to i=98 .

### 4.1.2: The inducer :

Figure 17.a presents the initial inducer definition (29x2x16 grid). This axial view of the pressure side shows the swept leading edge of the blade and the 270 degrees of wrap (at the hub).

Figure 17.b shows a meridional view of both the pressure and suction surfaces. Note that each side of the blade has been defined at different meridional locations .

### 4.1.3: The impeller :

Figure 18 shows both sides of the impeller main blade and splitter blade in the meridional view. Both splitters have the same geometry, but are simply rotated by 15 degrees. All the impeller blades are defined by 29x2x16 grids .

Note that the meridional locations of both sides of the blades are different. Note also that this meridional grid is quite different from the 2D meridional grid given in section 4.1.1 .

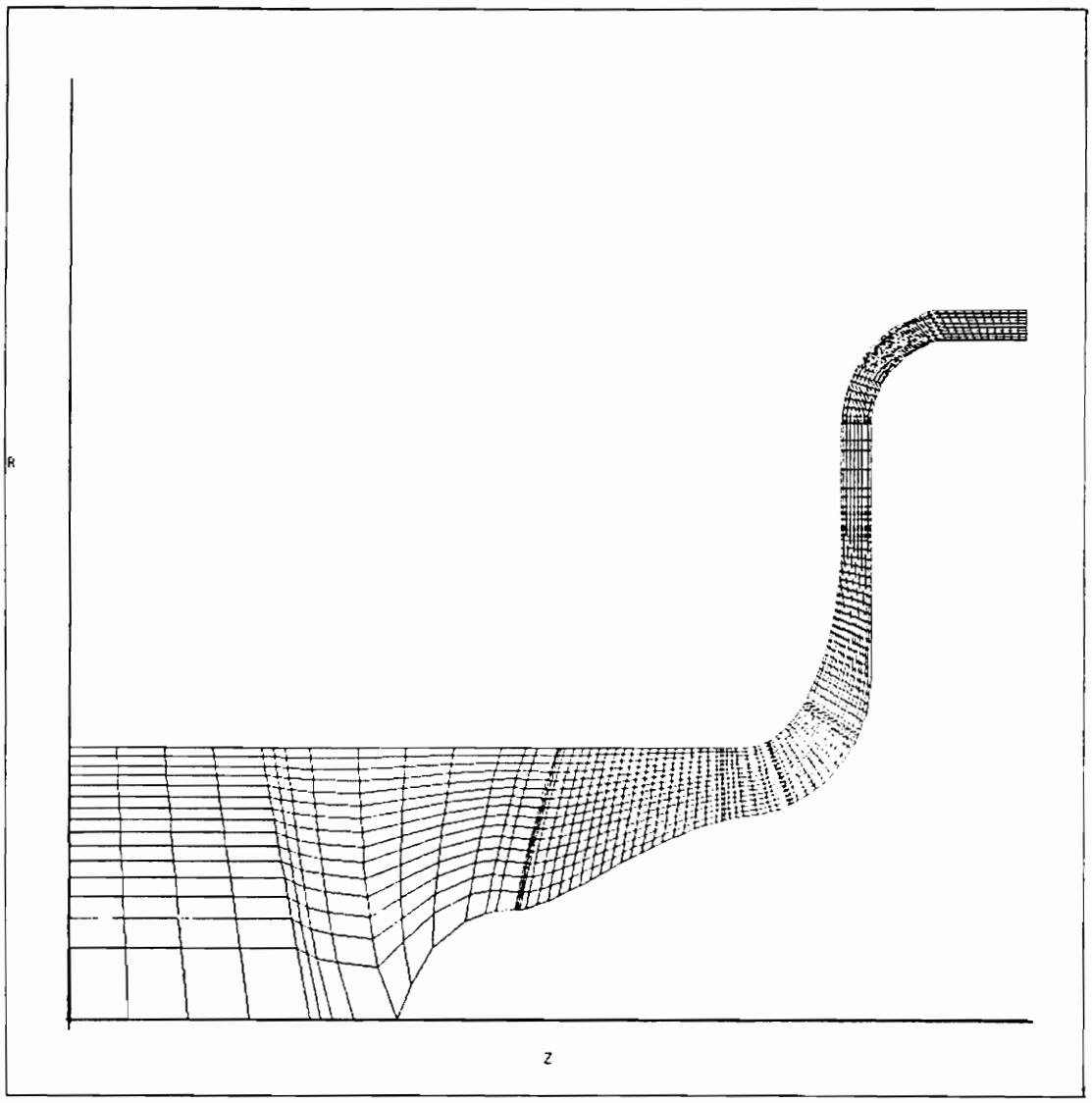


*Figure 16 : Meridional view of the initial grid .*

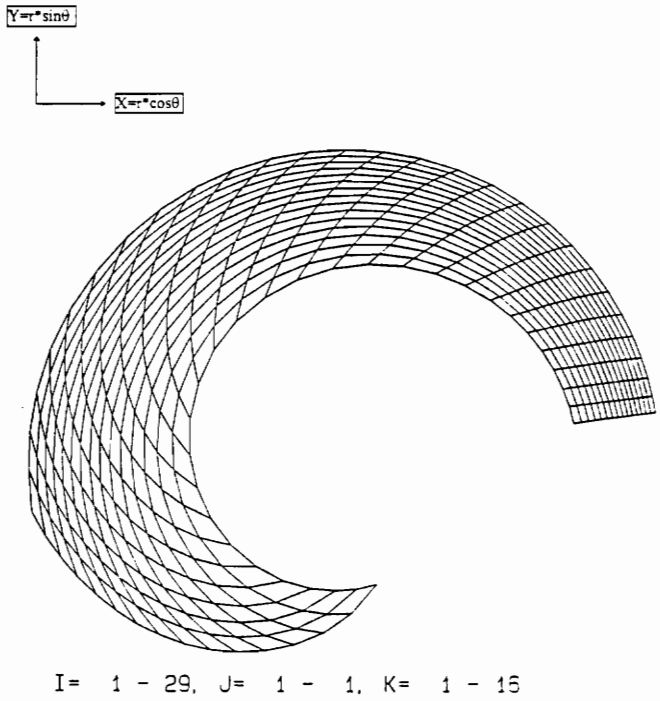


*Figure 17.a : Axial view of the inducer (pressure surface).*

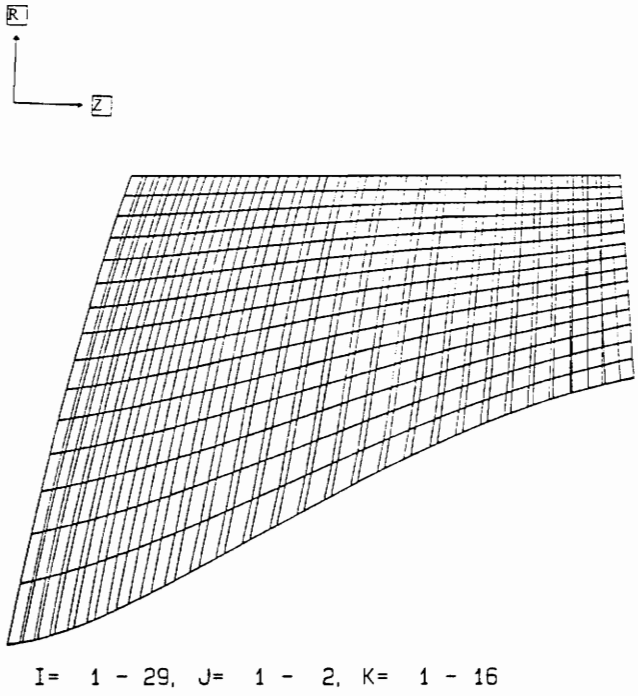


*Figure 17.b : Meridional view of the inducer (both surfaces) .*

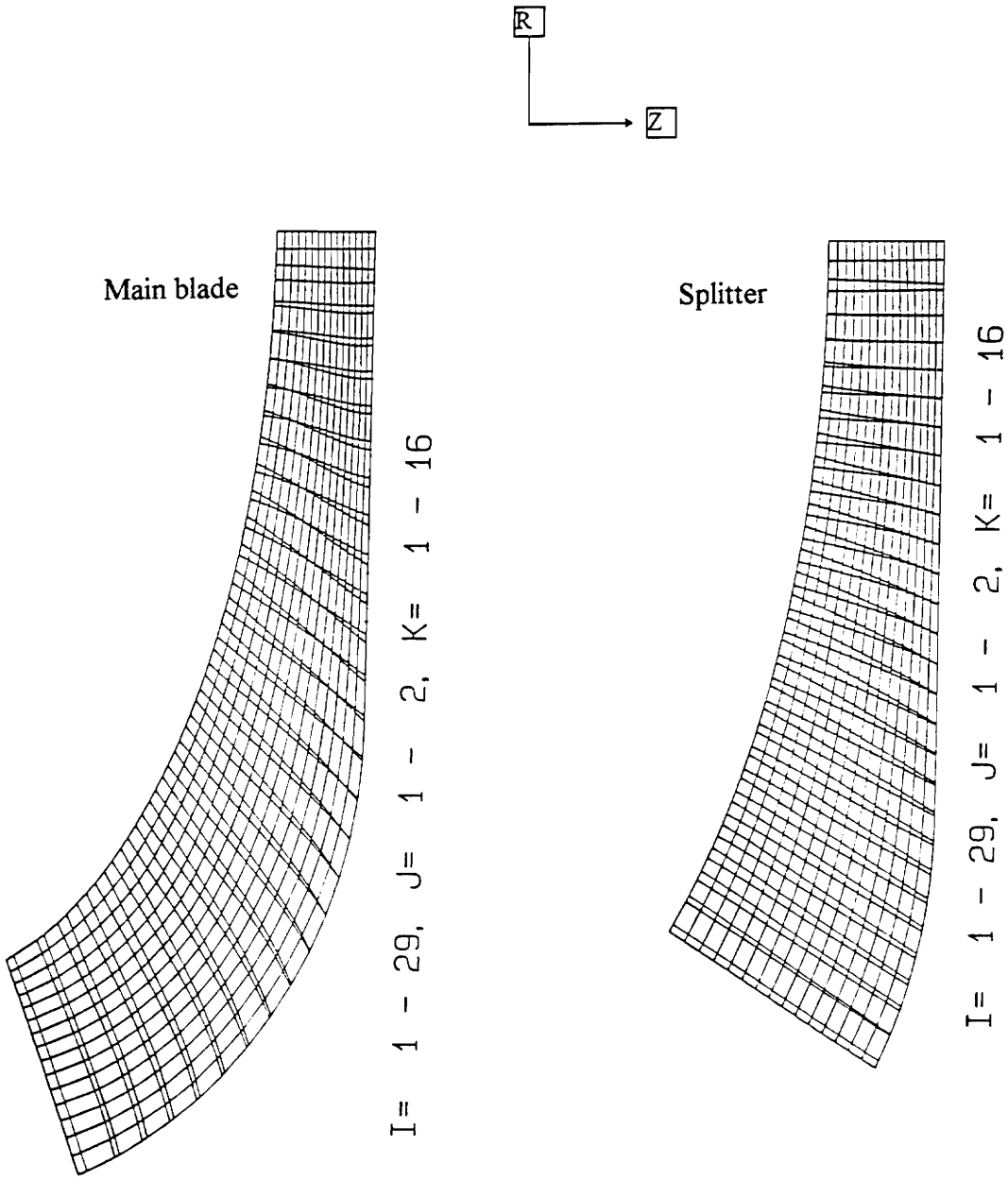


*Figure 18 : Meridional view of the impeller main and splitter blades (both surfaces) .*

## *4.2 Blade Interpolation .*

### 4.2.1: Why interpolate the blades ? :

It may be seen from Section 4.1 that the blades are not defined by the same number of points in the basic grid and in their own files. Also, the pressure side and the suction side of each blade are not defined by the same points in the meridional view, which creates connectivity problems since two corresponding points are not linked by a straight z=constant line in the blade-to-blade view. Moreover, the k-layers of the blades do not match with the ones of the basic grid .

Finally, the MEFP format requires single zone 3D i-j-k grids with coordinates and point types given for each grid point .

For these four reasons, there is clearly a need for a single grid on which everything will be defined. This final interpolating grid will be obtained in the next section. All the blades will be redefined on this new grid using interpolation procedures described in section 4.2.3 .

### 4.2.2: The interpolation grid :

The generation of the interpolation grid required several steps :

*_Spinner shape correction :*

The spinner nose in the initial grid was much too roughly defined (see Fig. 16). Using the exact shape of the spinner provided by the 2D meridional hub and shroud contours file, the spinner shape for the basic grid was redefined. Furthermore, some more points have been added to refine the spinner shape, and the corresponding grid lines have been added in the i-direction .

*_Inlet pipe section correction :*

The initial inlet section has the same radius as the tip radius of the inducer because the design calculations were made for a zero tip clearance. Geometric specifications require a finite non-zero tip gap, so that the effective inlet section has been modified to include the inducer tip gap .

For MEFP calculations, the hub radius of the inlet section (upstream the spinner) has also been changed from r=0 to r= $10^{-3}$ m. This is to prevent multiple points from having the same location. An "inviscid wall" boundary condition is used on the centerline upstream of the spinner .

_ *Modification of the diffuser shape :*

Downstream the impeller, the initial grid was made for a vaned diffuser, followed by a 90 degree bent channel that was primarily designed to match the following stages of the turbopump. This part of the grid is now replaced by a vaneless shrinking-area diffuser starting at radius $R_0$=1.0485 $R_2$, where $R_2$ is the impeller exit radius. The diffuser exit section $A_f = 2\pi.R_f.b_f$ is such that $A_f = 0.95\ A_0$, where $A_0 = 2\pi.R_0.b_0$ is known .

_ *LTE shape :*

Because they are not designed with a cusped shape, the LTE have been redefined with a square or chamfered shape. The square shape obtained can be seen in section 4.2.3, Fig. 20 .

For the inducer, this shape gives a maximum sharpness. The presence of a sharp angle on the suction side allows cavitation control by promoting this physical phenomenon .

For the impeller (main blades and splitters), LTE will be redefined for the final 3D grid (see section 4.4.2.5). A round shape is preferred to allow different flow incidences that might result from different flow rate conditions .

After all these modifications, the Final Interpolating Grid (FIG) is a 115x2x16 grid, as shown in Fig. 19 .

### 4.2.3: The interpolation procedure :

An accurate procedure was developed to interpolate each of the four blades onto the FIG. Basically, the procedure works in such a way that a set of 4 points from the blade surface are sought so that they define a quadrangle control surface which surrounds *one* grid point from the FIG. Once this set is found, a double linear procedure is used to interpolate the value $\theta$ of the tangential location of the blade. This all procedure is executed for each side of the blade. The complete scheme is given in Appendix 1 .

Figure 20 shows the comparison between the initial blade and the interpolated blade for the hub layer of the impeller main blade. Hub and shroud are the only layers where comparisons can be made since they are the only ones for which the blade definition matches the grid. The comparisons give a perfect agreement .

The figure also shows the sharp chamfered LTE of the blade .

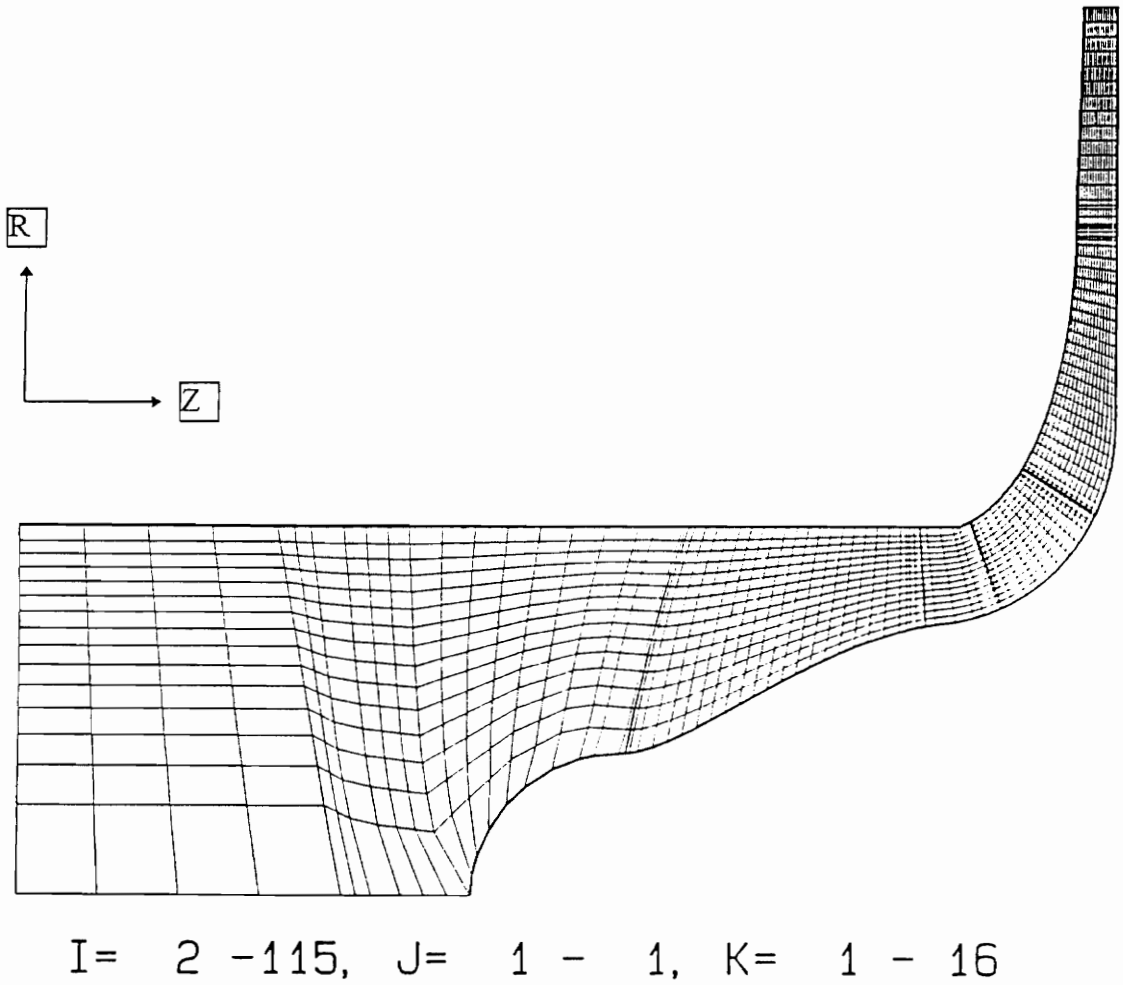


*Figure 19 : Final Interpolating Grid .*

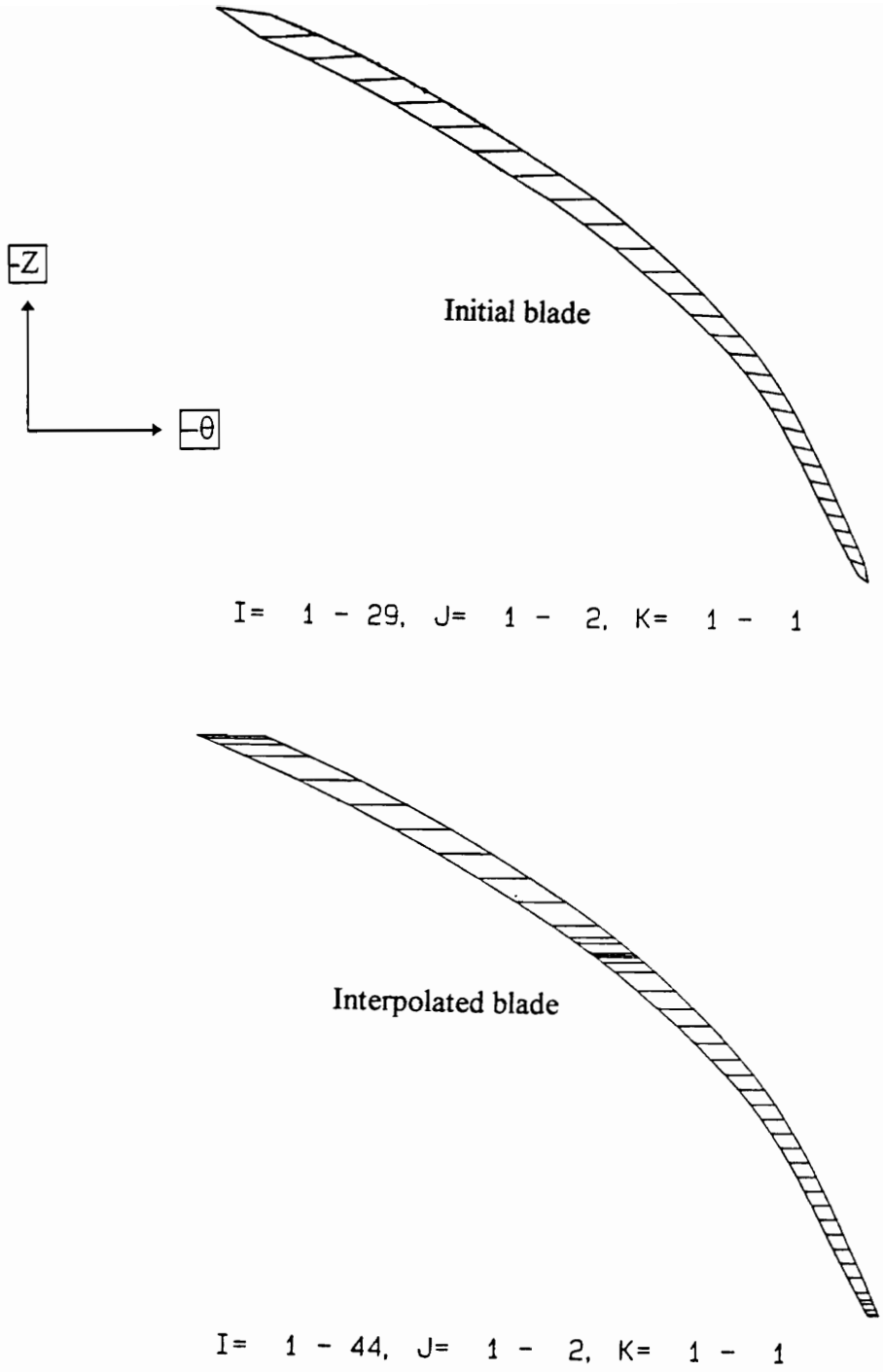


***Figure 20 : Comparison between the initial and the interpolated blade . (hub layer of the impeller main blade) .***

## *4.3 3D file generation for the different regions .*

### 4.3.1: The impeller :

The inducer has 4 blades. The impeller has 8 main blades and 16 splitters (two per main blade passage). The axisymmetry condition allows the whole geometry to be defined in a $\pi$ / 2 tangential segment. In that segment, there will therefore be 2 impeller main blades and 4 splitter blades for one inducer blade .

The 3 impeller blade types (one main blade and two splitters) are assembled and translated by $\pi$ / 4 . For each of the 17 hub-to-shroud layers (*see note*), the following operations have been done in the blade-to-blade direction :

_ 2 circumferentially repeating conditions are added such that their spacing is $\pi$ / 2 .

_ grid lines are generated from the splitter blades leading edges to the impeller main blade LE. These lines are parallel to the tangential boundary conditions .

_ three grid lines are added per splitter blade passage in a 10% / 50% / 90% distribution scheme (as a percent of the tangential passage width) .

This gives us a total of 31 lines in the j-direction.

The assembled impeller is a 44x31x17 grid, and is named *implr3D* .

<u>*Note :*</u>

The 17 layers of the impeller are the 16 layers from Section 4.1.3 to which an extra k-line (corresponding to the inducer tip) has been added to make the connectivity with the inducer file (see Section 4.3.2) .

### 4.3.2: The inducer :

Two circumferential boundary condition lines are generated with a tangential spacing of $\pi$ / 2 . The 31 lines of the impeller grid have to connect to 31 lines in the inducer grid :

_ 2 are used to define the inducer pressure and suction sides .

_ 2 are used to define the boundary conditions .

_ 3 are added within the inducer blade (25% , 50% , 75%) .

The remaining 24 lines are placed on each side of the inducer, where an equally spaced grid is adopted .

Shroud tangential definition .

The inducer blade is defined by 29x2x16 points. In order to take the inducer tip gap into account, the shroud surface has to be defined and incorporated in the inducer file. In order to have a tangential definition of the shroud in the main grid, $\theta$ is linearly interpolated at the shroud using the inducer tip. We therefore get the projection of the inducer on the shroud, so that the latter is actually considered as the fictitious 17th layer of the inducer (i.e. boundary conditions and the additional 24 lines are generated in the same way) .

The assembled inducer is a 25x31x17 grid, and is stored as *ind3D* .

### 4.3.3: The upstream region :

Using *ind3D*, we generate the tangential definition of the region upstream the inducer. For each of the 31 j-lines, we use :

$$\left(\frac{d\theta}{dz}\right)_{\text{upstream}} = \text{constant} = D \qquad (4.1)$$

D was initially taken to be $\left(\frac{d\theta}{dz}\right)_{\text{LE,PS}}$ inducer . Though this value looks appropriate, the resulting upstream grid gives very poor area ratios for the grid, and a correction of the inlet angle needed to be made. Therefore, the constant D was parametrically studied and chosen so that the grid showed good area ratios for better flow calculation accuracy .

The assembled upstream region is a 21x31x17 grid, and is stored as *up3D* .

### 4.3.4: The downstream region :

After reading *implr3D*, we generate the tangential definition of the region downstream the impeller. For each of the 31 j-lines, we use :

$$\left(\frac{d\theta}{dr}\right)_{\text{downstream}} = \left(\frac{d\theta}{dr}\right)_{\text{TE,PS impeller}} = \text{constant for all j and k .} \qquad (4.2)$$

The assembled downstream region is a 18x31x17 grid, and is stored as *down3D* .

### 4.3.5: The inducer/impeller gap region :

After reading *ind3D* and *implr3D*, we generate the tangential definition of the gap region. For each of the 31 j-lines and 14 k-lines, we use :

$$\left(\frac{d\theta}{dz}\right)_{gap} = \frac{\theta_{LE\,imp} - \theta_{TE\,ind}}{Z_{LE\,imp} - Z_{TE\,ind}} \text{ (j,k) = constant(j,k)} \qquad (4.3)$$

The assembled gap region is a 7x31x17 grid, and is stored as *gap3D* .

Note : All these 5 files are written in the MEFP format .

## *4.4 Construction of 3D calculation grids .*

### 4.4.1: *goptw* : A tool to manipulate grids :

*goptw* is the windows version of GEOMI, software that had previously been used by [17],[18]. *goptw* reads MEFP format grids and offers different options to modify grid features. The options we basically used were line addition or deletion, grid smoothing, grid visualization and storage .

The MEFP format is such that a new double indexation is added to each grid point in either rectangular or cylindrical coordinates. The first one accounts for the physical nature of the point : stationary wall point, rotating wall point, flow point or inner solid point. The second indexation is related to the application of *goptw* functions, and defines a new 3D representation of the grid with A(i), B(j), C(k) as relative reference locations. More details are given in Appendix 2 .

### 4.4.2 : Turbopump assembling - Grid refinements :

The 5 previous files are assembled to give a 115x31x17 3D grid in which the following improvements are to be made :

#### *4.4.2.1 : Changes in the i-direction :*

The impeller blades are over-defined in the i-direction and about one in every two lines has been deleted. In the diffuser, two lines out of three have been suppressed. Unnecessary extra lines near LTE have been deleted or moved. Finally, some lines were rearranged to make the grid spacing more uniform .

#### *4.4.2.2 : Tip gap definition :*

Three lines have been added in the k-direction to have allow flow in the inducer tip gap (25%,50%,75% of the gap). The LT values of these lines were corrected to be flow lines (LT=1) .

#### *4.4.2.3 : Changes in the k-direction :*

Lines have been moved or deleted such that the final distribution of the k lines is given by:

| | | |
|---|---|---|
| 0 % | : | hub |
| 1% , 3% , 10% , 30% , | | |
| 50% , 70% , 90% , 97% | : | blade definition |
| 99 % | : | tip |
| 99.2% , 99.5% , 99.8% | : | tip gap definition |
| 100 % | : | shroud . |

These percentages are expressed in terms of the inducer meridional exit section. We therefore finally have 14 lines in the k-direction. A particular attention has been given to the near shroud smoothing in the k-direction at the exit of the inducer as well as through the impeller. The grid spacing has been made approximately similar to the near hub k-spacing to avoid long and thin volumes in the impeller .

#### *4.4.2.4 : Smoothing in the j-direction, in the inducer :*

In order to have the same near wall spacing on the inducer as for the grids where the inducer is alone (see section 4.5.2), the smoothing in the j-direction made the near wall spacing 1% of the inducer passage .
The j-smoothing has also been performed in the impeller main passages .

#### *4.4.2.5 : Impeller leading edges correction :*

Because they are usually designed that way, and because we want to let the flow incidence vary with mass flow rate, the impeller LE have been rounded. This rounded shape is obtained by moving the grid lines at the LE so that the points belong to a circle .

#### *4.4.2.6 : Grid smoothing in the j-direction, in the impeller :*

Because of the previous operations (rounding of the LE and smoothing), the grid spacing in the j-direction for constant i-planes is not uniform. Using *goptw*, the grid has been smoothed in order to have a uniform j-spacing in the impeller main passages for each section i of the grid in a j-k plane. This smoothing has been done in the blade-to-blade view. No smoothing was necessary in the splitters passages .

## *4.5 Final 3D grids .*

### 4.5.1 : Tandem inducer/impeller 3D grid :

#### *4.5.1.1 : Grid definition :*

The final 3D calculation grid for the tandem configuration is a 85x31x14 grid .

Figure 21 shows a meridional view (z-r plane) of the grid. The locations of the inducer, the impeller main blades and the splitters blades LTE are shown. The 3D calculation inlet plane is also shown (see tab (2) on Fig. 21). Thus, the calculation grid (72x31x14) is shorter than the grid that has been defined previously because it was found that the 3D calculation could be started on the spinner. Note that the diffuser has been modeled as vaneless with a slightly contracting area ratio to eliminate backflow on the exit boundary .

Figure 22 shows the grid in an unrolled blade-to-blade view (θ-s planes, with s = unrolled meridional distance, where ds = $\frac{\sqrt{dr^2 + dz^2}}{r}$) for the mid-height constant k-surface. This unrolled view preserves blade angles but not meridional distance. This geometry contains two impeller main blades and four splitters (2 per main blade passage) for each inducer blade. The view shows two repeats in the θ-direction. Of particular interest are the inducer upstream grid angle and the definition of the inducer and impeller leading and trailing edges. The indexing of the inducer TE with respect to the impeller main blades LE can be seen. This figure also defines the nomenclature for the impeller blades as :

_ MB1, MB2 : impeller main blades
_ SP1, SP2 : splitter blades in the MB2-MB1 passage
_ SP3, SP4 : splitter blades in the MB1-MB2 passage

MB1 is the impeller main blade that is almost lined-up with the inducer blade. MB2 splits an inducer passage into two .

#### *4.5.1.2 : A,B,C grid parameters :*

This section describes the grid characteristics in terms of the A,B,C parameters which will constantly be referred to in the following analysis .

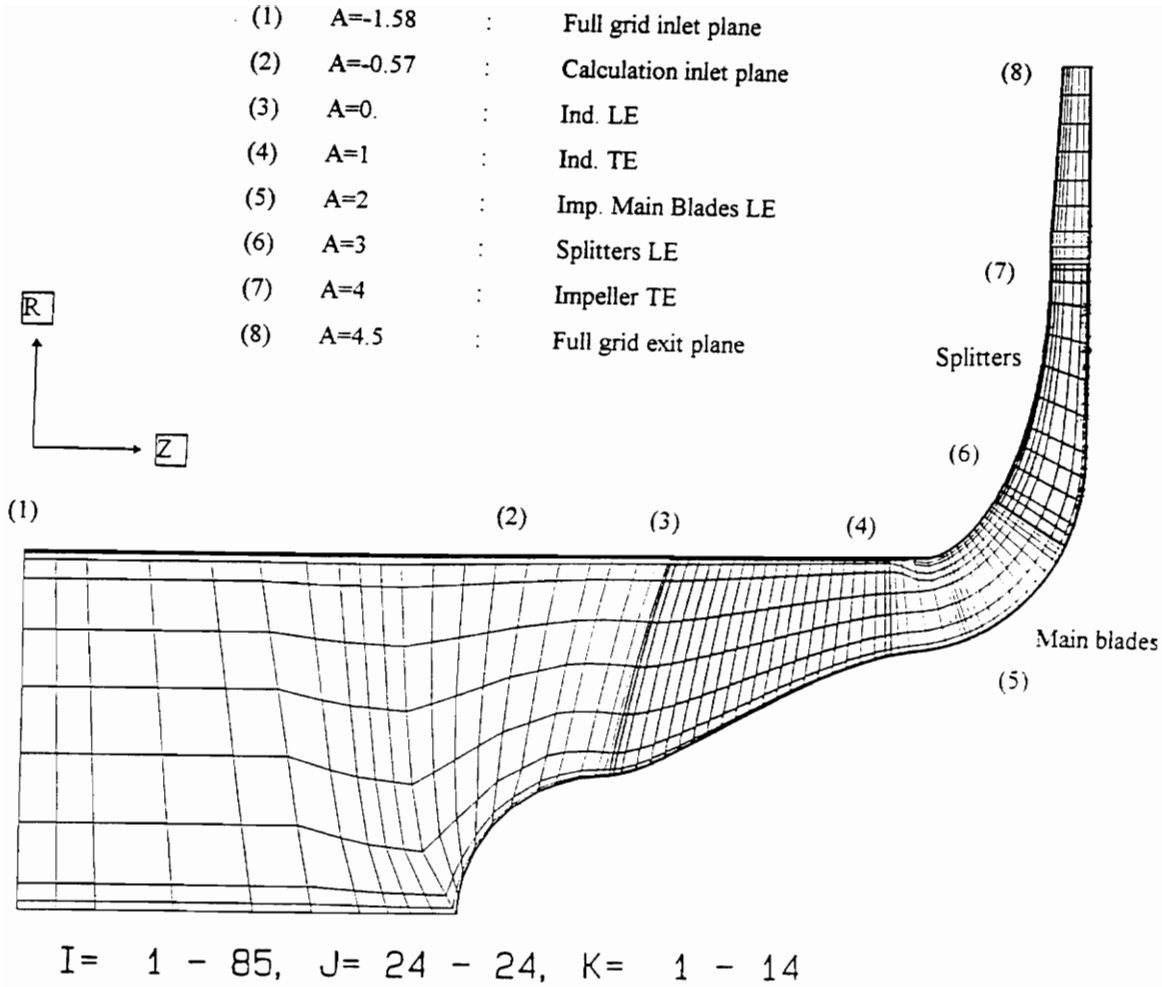


*Figure 21 : Meridional view of the 85x31x14 calculation grid .*

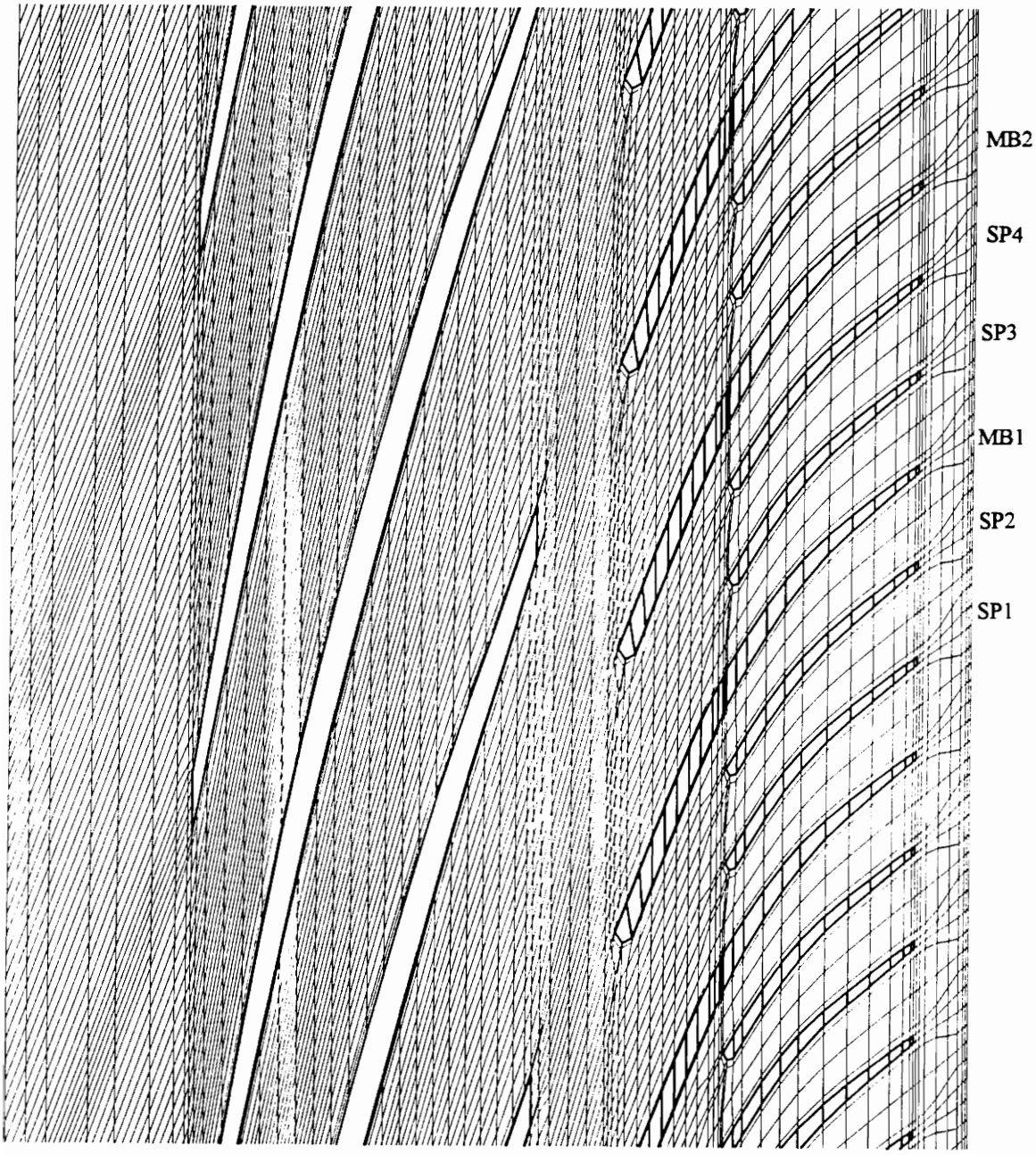


***Figure 22 : Unrolled blade-to-blade view of the full tandem inducer/impeller grid (85x31x14) .***

_ A is the streamwise parameter representing the meridional distance (see Fig. 21 for the corresponding planes) :

| | | | |
|---|---|---|---|
| * A= | -1.58 | : grid inlet | plane (1) |
| * A= | -0.57 | : calculation inlet plane on the spinner | plane (2) |
| * A= | 0.0 | : inducer LE | plane (3) |
| * A= | 1.0 | : inducer TE | plane (4) |
| * A= | 2.0 | : main blade impeller LE | plane (5) |
| * A= | 3.0 | : splitter blade LE | plane (6) |
| * A= | 4.0 | : impeller TE | plane (7) |
| * A= | 4.5 | : diffuser exit | plane (8) |

_ B is the blade-to-blade parameter (B=j) :

| | | |
|---|---|---|
| * inducer pressure side (PS) | : | j=20 |
| * inducer suction side (SS) | : | j=24 |
| * PS of the impeller main blades | : | j=13 & 28 |
| * SS of the impeller main blades | : | j=14 & 29 |
| * PS of the impeller splitter blades | : | j=8 & 23 |
| * SS of the impeller splitter blades | : | j=9 & 24 |
| * PS of the impeller splitter blades | : | j=3 & 18 |
| * SS of the impeller splitter blades | : | j=4 & 19 |
| * repeating boundaries | : | j=1 & 31 |

*Note :* The B parameter is usually made proportional to the blade spacing. Though this might have been done for the inducer, no possible solution could have been obtained for the impeller because of the connectivity that has to be made between the inducer and the impeller. Thus, B was simply kept to equal j throughout the whole geometry .

_ C is the hub-to-shroud fractional distance parameter. It corresponds to the hub-to-shroud distance on the inlet plane, plane (1) in Fig. 21. The hub-to-shroud distance varies as follows (Table 2) :

*Table 2 : Definition of the C parameter .*

| C parameter | Hub-to-shroud inducer exit | Hub-to-shroud impeller exit | Location |
|---|---|---|---|
| 0. | 0. | 0. | hub |
| 0.024 | 0.0074 | 0.0066 | inducer blade definition |
| 0.073 | 0.0225 | 0.020 | |
| 0.2428 | 0.075 | 0.066 | |
| 0.4335 | 0.219 | 0.200 | |
| 0.6204 | 0.423 | 0.400 | |
| 0.78 | 0.638 | 0.625 | |
| 0.9215 | 0.854 | 0.739 | |
| 0.975 | 0.941 | 0.825 | |
| 0.9912 | 0.9678 | 0.909 | inducer tip |
| 0.9932 | 0.9753 | 0.949 | tip gap |
| 0.9956 | 0.984 | 0.982 | |
| 0.998 | 0.9927 | 0.997 | |
| 1.0 | 1.0 | 1.0 | shroud |

## 4.5.2 : Inducer-alone 3D grids :

In order to analyze the possible influence of the impeller on the inducer flow, a grid has to be generated for the inducer alone. Since the influence of the downstream geometry on the inducer is also of interest, a grid will be constructed with an axial exit after the inducer .

Since the impeller has been removed for the comparative study of the inducer-alone calculations ( IAC), the 3D grids for the inducer alone require less grid points .

### *4.5.2.1: New grid spacing in the j-direction :*

The analysis of the inducer flow does not require all the lines that are necessary to define the impeller. A new spacing is defined for the inducer alone .

The basic grid is the one defined in section 4.5.1 . All the j-lines are removed except the inducer blade lines and the repeating boundaries. Using *goptw*, some new j-lines are inserted so that the spacing now becomes :

| | | |
|---|---|---|
| B = | -0.73 ; -0.5 ; -0.3 ; -0.15 ; -0.07 ; -0.03 ; -0.01 | : pressure side, |
| | 0 ; 0.5 ; 1.0 | : inducer, |
| | 1.01 ; 1.03 ; 1.07 ; 1.15 ; 1.27 | : suction side . |

That j-spacing, defined by 15 lines, is proportional to the inducer passage. The near wall lines are located at 1% .

The k-spacing at the exit of the inducer is modified in the same way as it was for the full grid so that the near wall spacing looks like the hub one .

The new grid is intended to give an initial estimate of the 3D flow for the inducer/impeller configuration. Two extra lines were found to be necessary to improve the accuracy of the flow definition at the nose of the spinner. These two extra lines have been added at A = -1.015 and C = 0.1579 .

#### *4.5.2.2: Radial-exit grid :*

The 83x15x15 basic grid for the inducer alone was built, and is identical in its meridional view (Fig. 23) to the full 3D tandem inducer/impeller grid, except that the impeller blades have been removed. Also, an extra line has been added in the k-direction near the hub to better define the flow near the spinner.

The impeller hub and shroud contours have the same boundary conditions as the tandem configuration : the shroud is stationary except where the impeller would be, and the hub rotates until the location of the impeller exit .

In the blade-to-blade view (Fig. 24), fewer grid lines (15 instead of 31) were required to define the flow passage. Again, the inducer near-wall lines are located at 1% of the inducer passage as for the full 3D grid, thus allowing accurate comparison on near-wall PS and SS .

#### *4.5.2.3: Axial-exit grid :*

This grid is derived directly from the radial-exit grid by changing the inducer exit geometry:

_ the shroud radius is kept constant throughout the whole geometry ,
_ at the inducer exit, the hub radius is also taken to be constant. This radius corresponds to the inflection point radius in the full grid. Thus, it is intended that no geometrical defect be introduced in the geometry that might create unexpected physical phenomena .

Figure 25 shows the axial geometry in the meridional view. The shroud is kept stationary throughout the whole geometry. At the hub, the wall is rotating from the spinner till the beginning of the axial exit. At that point (A=1.451), the hub is stationary, thus reproducing identical conditions as in the tandem bladed inducer calculations from Excoffon [18]. The inducer near-wall lines are also located at 1% of the inducer passage .

Both the calculations for the Inducer in the Tandem Configuration, ITC, and the Inducer-Alone in the Radial Configuration, IARC, were started on the inlet plane located on the spinner. The calculation for the Inducer-Alone in the aXial Configuration, IAXC, was made over the whole grid .

The ITC calculation results are presented in the next section, 5.0 . The calculation results for the Inducer-Alone Configurations, IAC, are presented in section 6.0 .

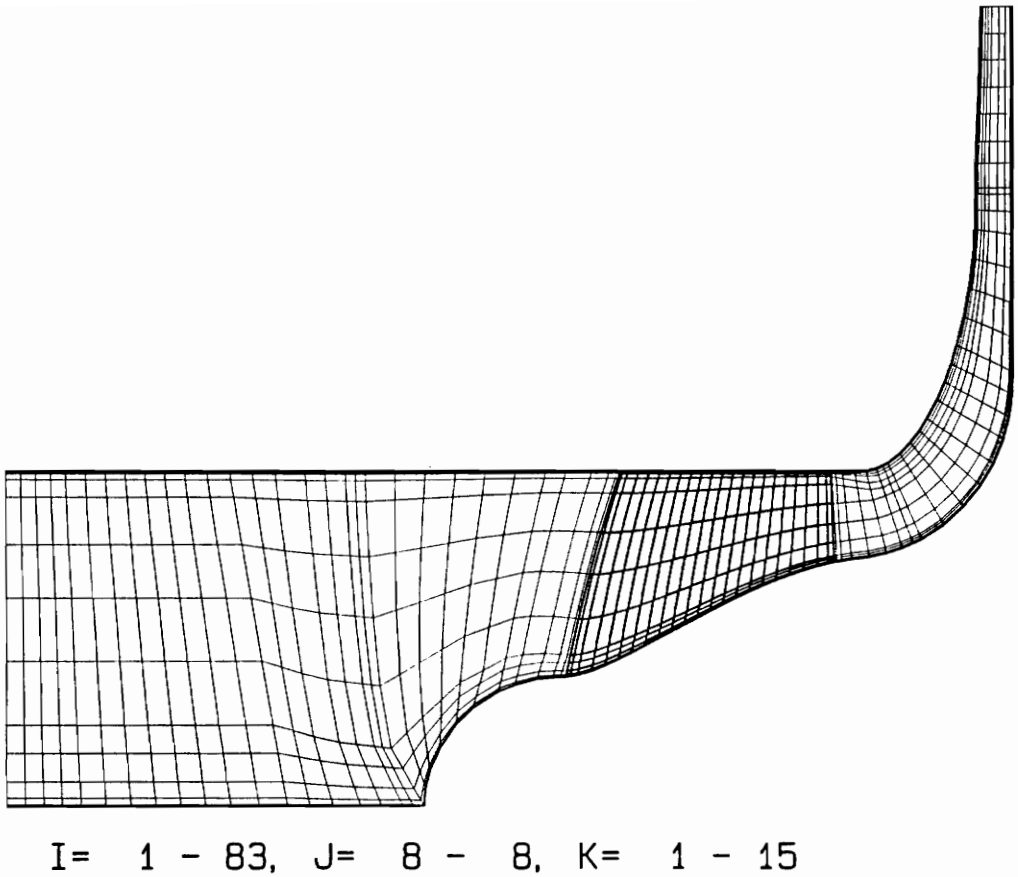


*Figure 23 : Meridional view of the IARC grid (83x15x15) .*

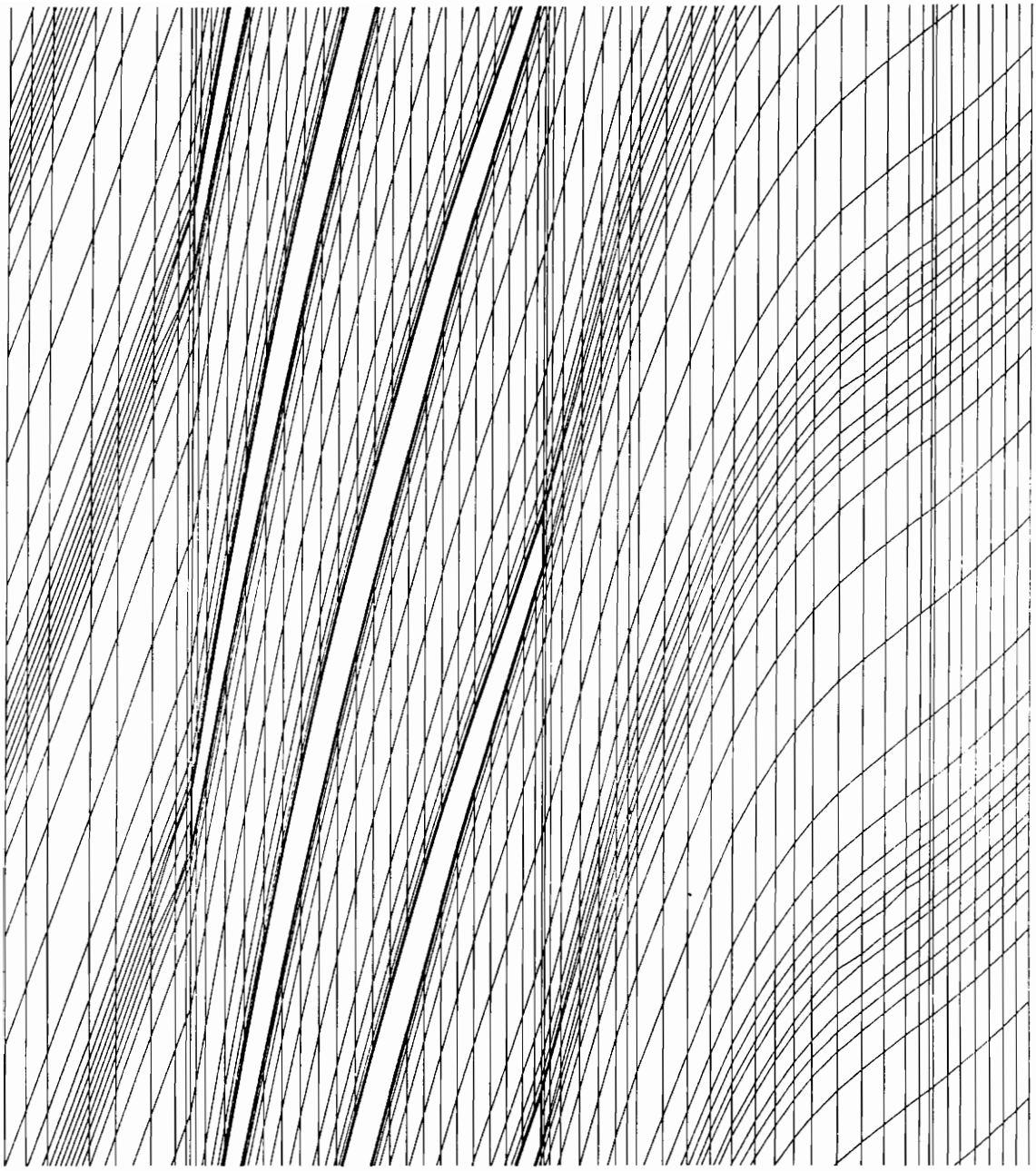

*Figure 24 : Unrolled blade-to-blade view of the IARC grid (83x15x15) .*

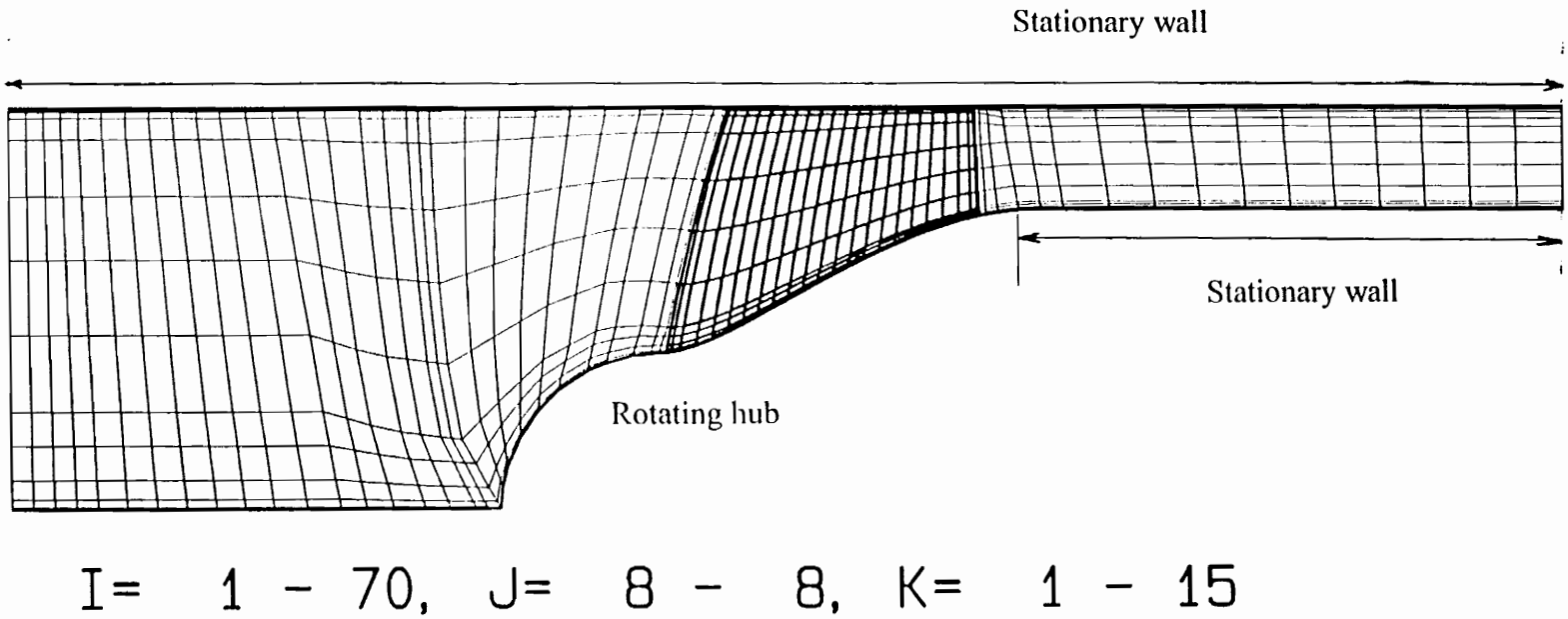


*Figure 25 : Meridional view of the IAXC grid (70x15x15) .*

# 5.0 RESULTS of THE TANDEM INDUCER-IMPELLER 3D FLOW CALCULATION.

## *5.1 Introduction .*

A turbulent full-3D flow calculation for the MCA tandem inducer/impeller geometry has been run at the nominal design flow conditions with liquid hydrogen :

_ inlet flow coefficient : $\phi = \frac{V_{ax}}{U_{tip}} = 0.0867$ .

_ inducer Reynolds number : $Re = \frac{\rho U_{tip} D_i}{\mu} = 188x10^6$ .

This section presents the results of the first high Reynolds number 3D flow calculation for a rocket pump inducer at nominal design conditions, and probably the first tandem inducer/impeller calculation :

_ The main features of the flow (pressure rises, impeller flow split) are first discussed .

_ The flow analysis is then detailed in terms of meridional results and performance of the inducer (velocities, losses, leading edge vortex, and blade-loading) .

_ A blade-to-blade analysis will provide insight into the physics of the tandem configuration, thus enabling a loss build-up study to be performed. In particular, a link between the flow split and the loss distribution will be shown .

_ The meridional velocity field in the impeller will be discussed, followed by the impeller blade loading analysis .

_ Finally, cavitation inception will be analyzed both in the inducer (as expected) and in the impeller where this phenomenon is not usually of concern .

## *5.2: Calculation procedure and details :*

In a pipe representing the upstream inlet of the inducer, the developing 2D flow was calculated for the design flow rate. The velocity profile corresponding to 3 percent blockage (due to the shroud boundary layer) was then used as an input for the 2D meridional calculation (with no blades) which, in turn, was the input for the 3D inducer alone calculation .

Both the 2D-meridional and the 3D inducer-alone calculations showed that a plane of nearly uniform static pressure could be found on the spinner. That plane was taken to be the inlet of the full 3D calculation after checking that this plane was far enough upstream of the inducer leading edge vortex .

Finally, the results of the 3D inducer-alone run, together with a better first estimation of the impeller flow, were used to start the 3D tandem inducer/impeller calculation. The exit boundary conditions for all the calculations imposed a uniform pressure gradient (dP/di = constant, with i = streamwise grid index, see section 4.0) and fixed the mass flow rate .

For the tandem inducer/impeller 3D calculation (72x31x14 grid points), MEFP took 66 hours of CPU time to compute the 200 iterations on a HP720 workstation.

A comparison of calculations for the inducer,
a) the tandem inducer/impeller calculation with 31 grid lines blade-to-blade,
b) the inducer alone calculations with 15 grid lines blade-to-blade,
showed no significant grid dependence .

## 5.3 *Calculation main results.*

### 5.3.1: One-dimensional Mass-averaged pressures :

Figure 26 shows the mass-averaged pressure coefficients plotted against the A parameter through the whole geometry. The pressures are defined as follows :

_ t : total pressure $\quad p_t = p + \frac{1}{2}\rho V^2 \quad (5.1)$

_ s : static pressure $\quad p$

_ * : rotary stagnation pressure $\quad p^* = p + \frac{1}{2}\rho W^2 - \frac{1}{2}\rho r^2\omega^2 \quad (5.2)$

_ r : reduced pressure . $\quad p_r = p - \frac{1}{2}\rho r^2\omega^2 \quad (5.3)$

where V is the absolute velocity and W is the relative velocity .

The reference pressure level is given by : $p_{t,max,inlet} = p_0 = 0$. The pressures are non-dimensionalized by the inducer-tip dynamic pressure $\frac{1}{2}\rho U_{ind.tip}^2$. The non-dimensionalized pressures therefore become pressure coefficients $P_t$ , P , P* and $P_r$ :

$$P_t = \frac{p_t - p_0}{\frac{1}{2}\rho U_{ind.tip}^2} \qquad P = \frac{p - p_0}{\frac{1}{2}\rho U_{ind.tip}^2}$$

$$P^* = \frac{p^* - p_0}{\frac{1}{2}\rho U_{ind.tip}^2} \qquad P_r = \frac{p_r - p_0}{\frac{1}{2}\rho U_{ind.tip}^2} \qquad (5.4)$$

Figure 26 shows that both static and total pressures are rising through the inducer, with static and total pressure coefficients at the inducer exit of $P_s$=0.3, $P_t$=0.4. At the exit of the inducer, the blade is slightly unloading, as will be seen in section 5.4.4. In the inducer/impeller gap, the total pressure remains relatively constant while the static pressure falls. Each section (A=-0.5,1 ; A=1,2 ; A=2,3 ; A=3,4) generates about the same amount of loss -ΔP*=0.04 and it can be seen that losses associated with the impeller are mainly generated at leading and trailing edges (Fig. 27). Overall, the losses are small compared with the total pressure rise .

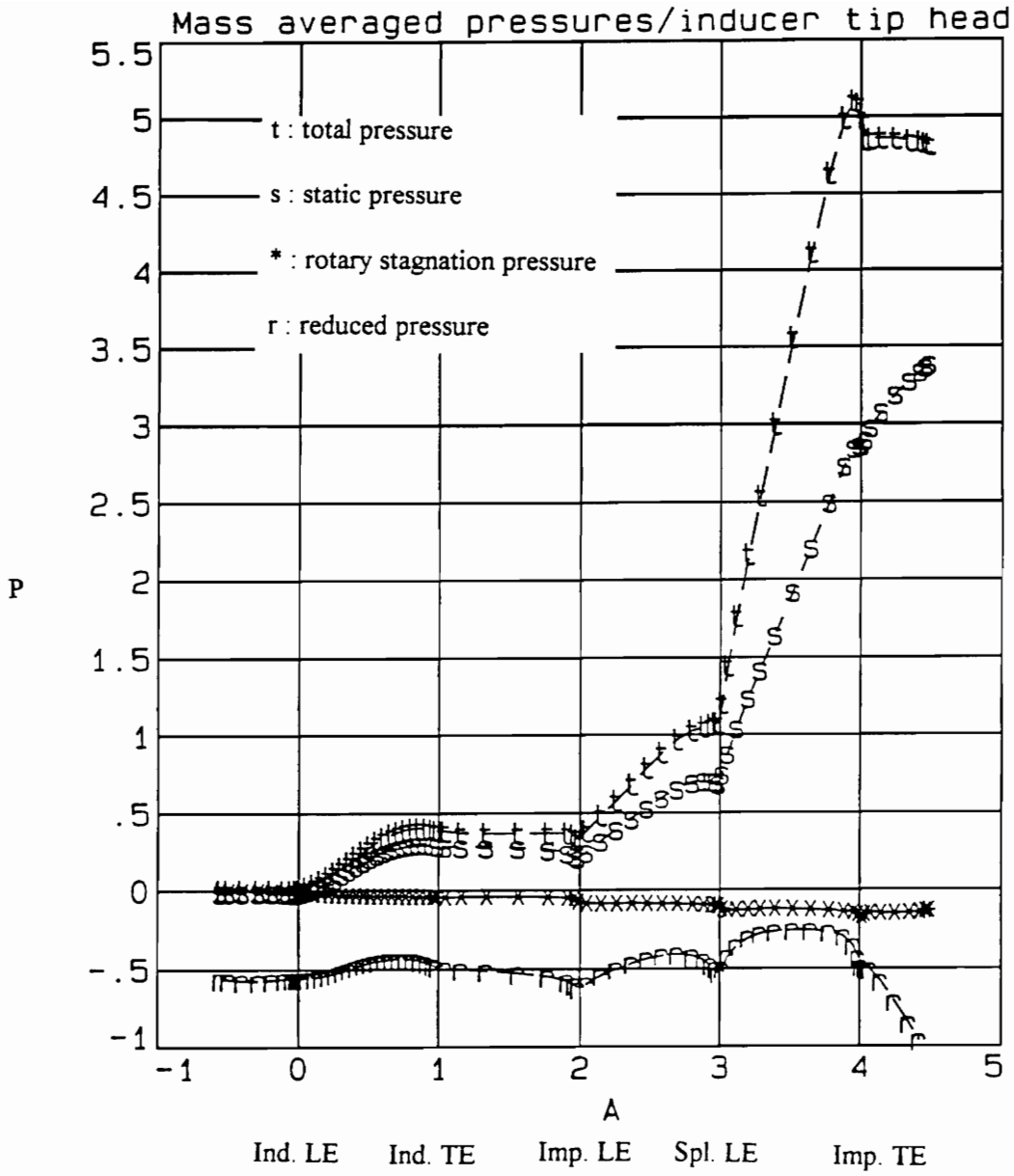


*Figure 26 : Mass-averaged pressure coefficients .*

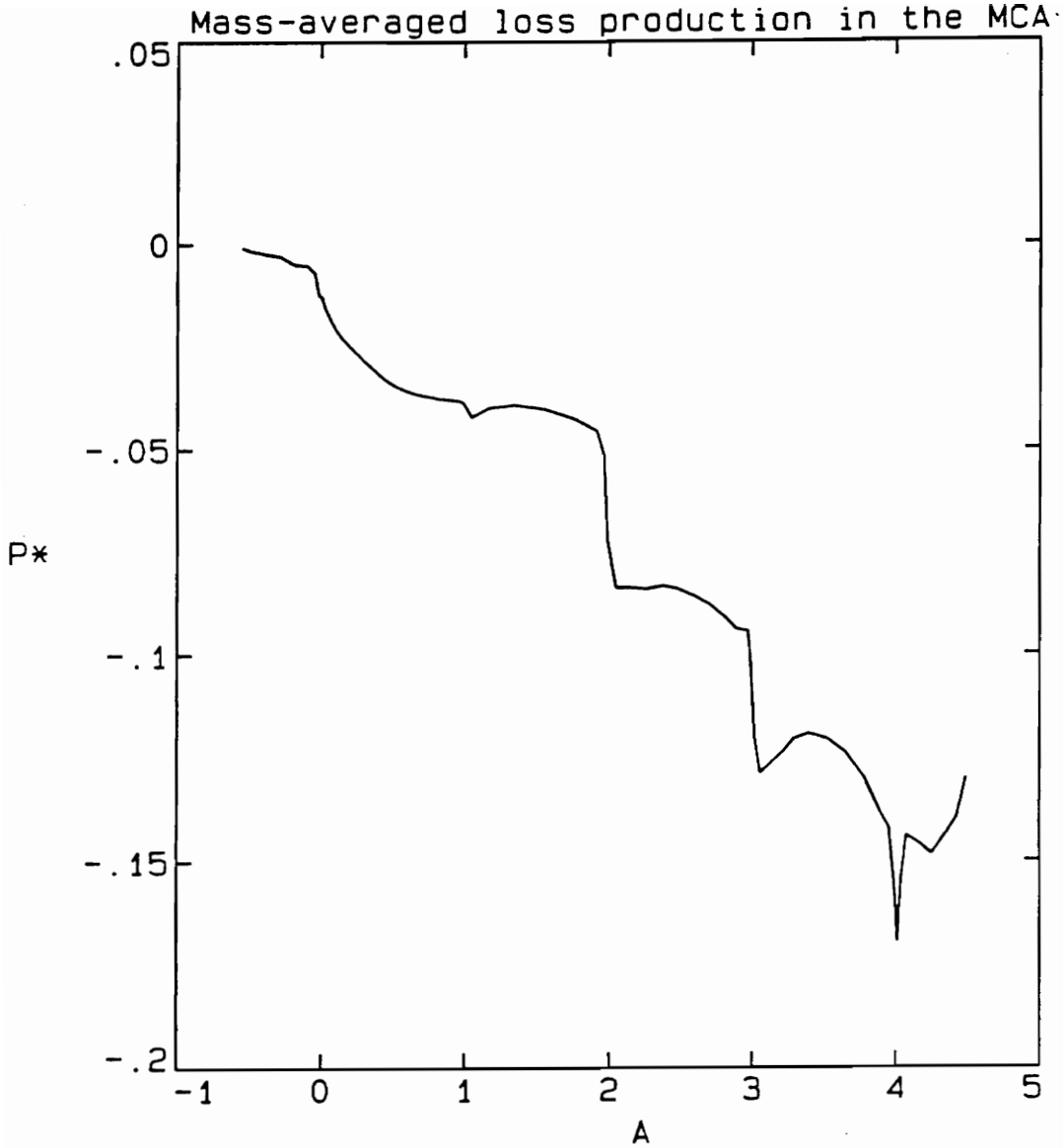


*Figure 27 : Mass-averaged losses throughout the MCA configuration .*

From the impeller main blades LE to the splitters LE, the impeller has achieved approximately 17 percent of the impeller static pressure rise, and 17 percent of the total pressure rise. As can be seen from Fig. 26, most of the static and total pressure rises are achieved in the splitter section, mostly by centrifugal effects. At the impeller exit, a slight reduction in the total pressure can be seen .

### 5.3.2: Flow split in the impeller :

Figure 28 shows the distribution of the flow rate through the impeller .

A very good flow split is obtained between the main blade passages with each passage fed with half the total flow rate. In the splitters, the flow split is more irregular :

_ passages (MB2-SP1) and (SP3-SP4) have close to the ideal flow rate (16.7 percent),

_ passages (SP2-MB1) and (SP4-MB2) see 25 percent more than the ideal distribution,

_ passages (SP1-SP2) and (MB1-SP3) see approximately 25 percent less flow than the ideal case .

The following table (Table 3) gives the numerical details of the flow split in the impeller :

***Table 3 : Flow split in the impeller .***

| | | | |
|---|---|---|---|
| | | MB2-SP1 | 16.000 % |
| Main passage I | 50.375 % | SP1-SP2 | 13.888 % |
| | | SP2-MB1 | 20.487 % |
| | | MB1-SP3 | 12.776 % |
| Main passage II | 49.625 % | SP3-SP4 | 15.202 % |
| | | SP4-MB2 | 21.647 % |

As will be seen in section 5.6, this flow split is highly dependent on the loss distributions in the inducer, the inducer/impeller gap, and the impeller itself .

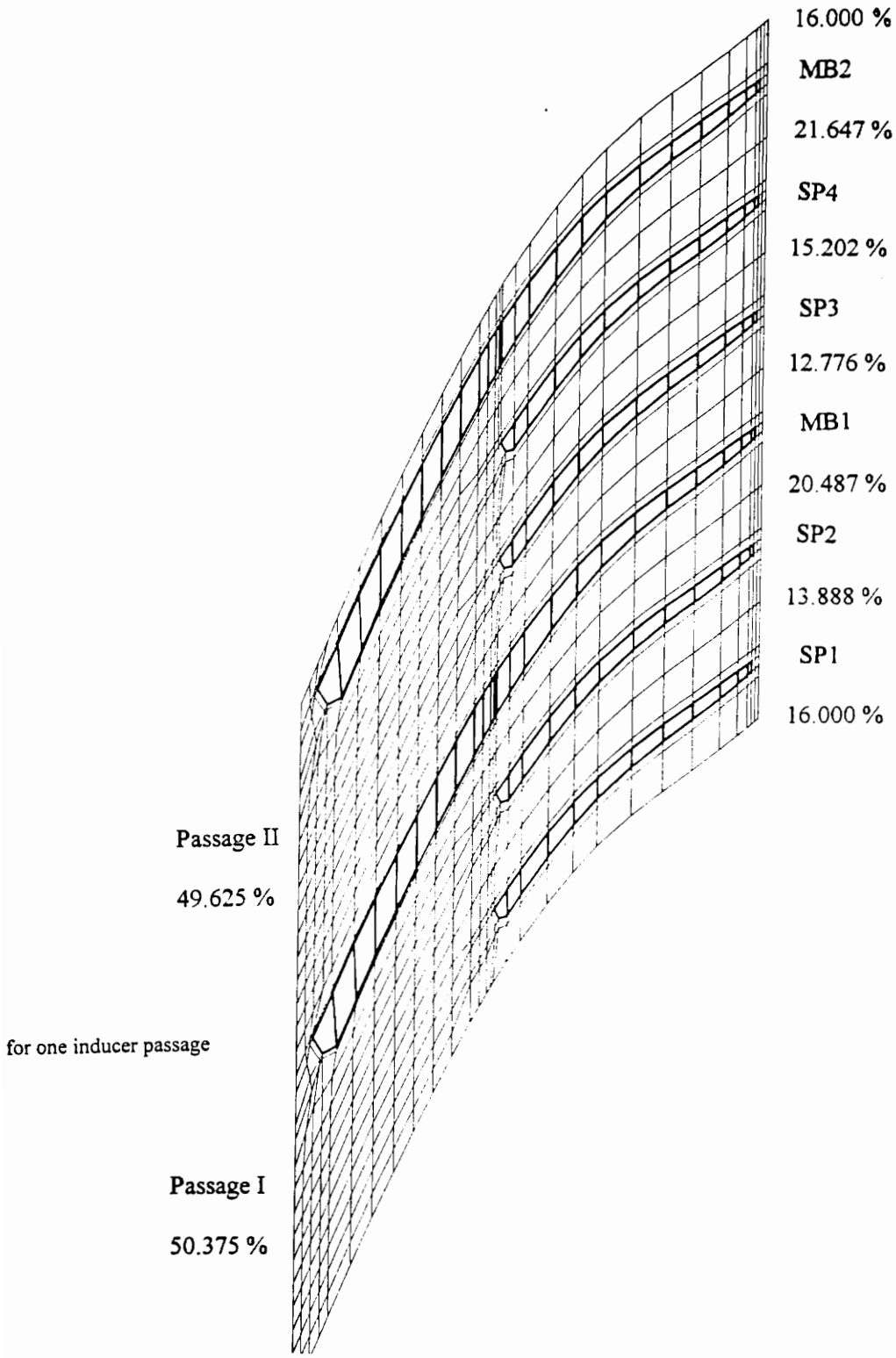


*Figure 28 : Flow split in the impeller .*

### 5.3.3: Efficiencies :

The efficiency was computed [20] as :

$$\eta = 1 - \frac{\Psi_{loss2} - \Psi_{loss1} + \Psi_{TSs}}{\Psi_{E2} - \Psi_{E1} + \Psi_{TSs}} \qquad (5.5)$$

In this formula :

_ inducer efficiency computation :

(1) is the grid inlet plane and (2) is just downstream of the inducer exit (A=1.338) .

_ impeller efficiency computation :

(1) is the just downstream of the inducer exit (A=1.338) and (2) is just downstream of the impeller exit (A=4.0125) .

_ MCA pump efficiency computation :

(1) is the grid inlet plane and (2) is just downstream of the impeller exit (A=4.0125) .

_ Moment of momentum coefficient : $\Psi_E = \Psi_t + \Psi_{loss} = \frac{p_t - p_0}{\frac{1}{2}\rho U^2_{ind.tip}} + \Psi_{loss}$ (5.6)

_ Loss coefficient : $\Psi_{loss} = - P^* = - \frac{p^* - p_0}{\frac{1}{2}\rho U^2_{ind.tip}}$ (5.7)

_ Dissipated moment of momentum due to the wall-shear stresses on the stationary shroud : $\Psi_{TSs}$

_ For the inducer and the pump, $\Psi_{E1} = 0$ at the inlet plane because the flow is not prewhirled .

_ For the impeller, $\Psi_{E1\ impeller} = \Psi_{E2\ inducer}$ , $\Psi_{loss1\ impeller} = \Psi_{loss2\ inducer}$ .

_ For the MCA pump, $\Psi_{TSs}$ is taken at the impeller LE .

The following table (Table 4) details all the terms that were used to compute the efficiency $\eta$ for the inducer, the impeller and the whole pump .

***Table 4 : Relative importance of the different terms in the efficiency computation for the MCA elements .***

| | $\Psi_{E1}$ | $\Psi_{E2}$ | $\Psi_{loss1}$ | $\Psi_{loss2}$ | $\Psi_{TSs}$ | $\eta$ |
|---|---|---|---|---|---|---|
| **Inducer** | 0. | 0.4106 | 0.00034 | 0.0396 | 0.0028 | 0.8983 |
| **Impeller** | 0.4106 | 5.0034 | 0.03960 | 0.1556 | 0.0001 | 0.9747 |
| **MCA Pump** | 0. | 5.0034 | 0.00034 | 0.1556 | 0.0029 | 0.9685 |

*Note :* The inducer and pump efficiency calculations include the losses due to the LE vortex since the changes in work and loss were taken relative to the grid inlet and not the inducer inlet plane. No dissipated moment of momentum due to wall-shear stresses on the stationary shroud exists inside the impeller itself since it is shrouded. However, some losses exist ($\psi_{TSs}$=0.0001= $\psi_{TSs)A=1.88}$ - $\psi_{TSs)A=1.338}$ ) in the gap between planes A=1.338 and A=1.88 (the impeller rotating shroud starts before the LE). They are very small compared to the already small losses. For the high Reynolds numbers of the present 3D calculations, the dissipated moment of momentum due to the wall shear stresses on the shroud is small compared to losses and work .

The calculation inducer efficiency is 89.8 percent. The work in the impeller is 11 times the work in the inducer, while the losses are 3 times larger. Thus, the efficiency of the impeller is significantly higher, 97.5 percent. The overall efficiency of the tandem inducer/impeller is 96.9 percent .

The head coefficients, $gH / U_2^2$, corresponding to the results in Table 4, are 0.69 and 0.74 for the impeller and the tandem inducer/impeller, respectively .

## *5.4 Inducer meridional results analysis .*

### 5.4.1: Velocity vectors :

Figure 29 shows respectively the inducer mid-passage (B=10), the inducer near-wall suction surface SS (B=25) and the inducer near-wall pressure surface PS (B=19) meridional velocities from the inlet plane till the impeller LE .

The mid-passage flow follows the grid lines over most of the blade height. At the shroud, the first half of the inducer chord has negative velocities resulting from the tip leakage. The backflow ends in a vortex just upstream of the LE. The second half of the inducer has streamwise oriented velocities .

On the SS, the LE tip vortex is clearly seen upstream and extending slightly into the passage. Secondary flows near the hub, shroud and in the second half of blade chord move the flow radially outward. The radial component is at most of the order of the meridional velocity. This outward behavior results from the radial reduced static pressure distribution (lower at the shroud than at the hub) and the centrifuging of the boundary layer .

On the pressure side, velocities show a strong radially outward and backward behavior at the shroud due to the inducer tip leakage (pressure drop between the PS and the SS). At the LE, strong backwards velocities contribute to the tip vortex that can be seen on each figure. This vortex is circumferentially quite uniform (see 5.4.3) as the velocity pattern shows, and it does not extend very far upstream of the LE. On the last third of the inducer chord, velocities depart from the streamwise direction over the entire blade height and are more radially outward .

The outward pattern of the velocities is much weaker than that observed by LeFur [17] and Excoffon [18] in the VULCAIN inducer with the air test conditions. The intensity of the LE vortex is also weaker. These differences are probably due to the much higher Reynolds number in the present case ($188 \times 10^6$) than in the previous studies ($1.1 \times 10^6$) .

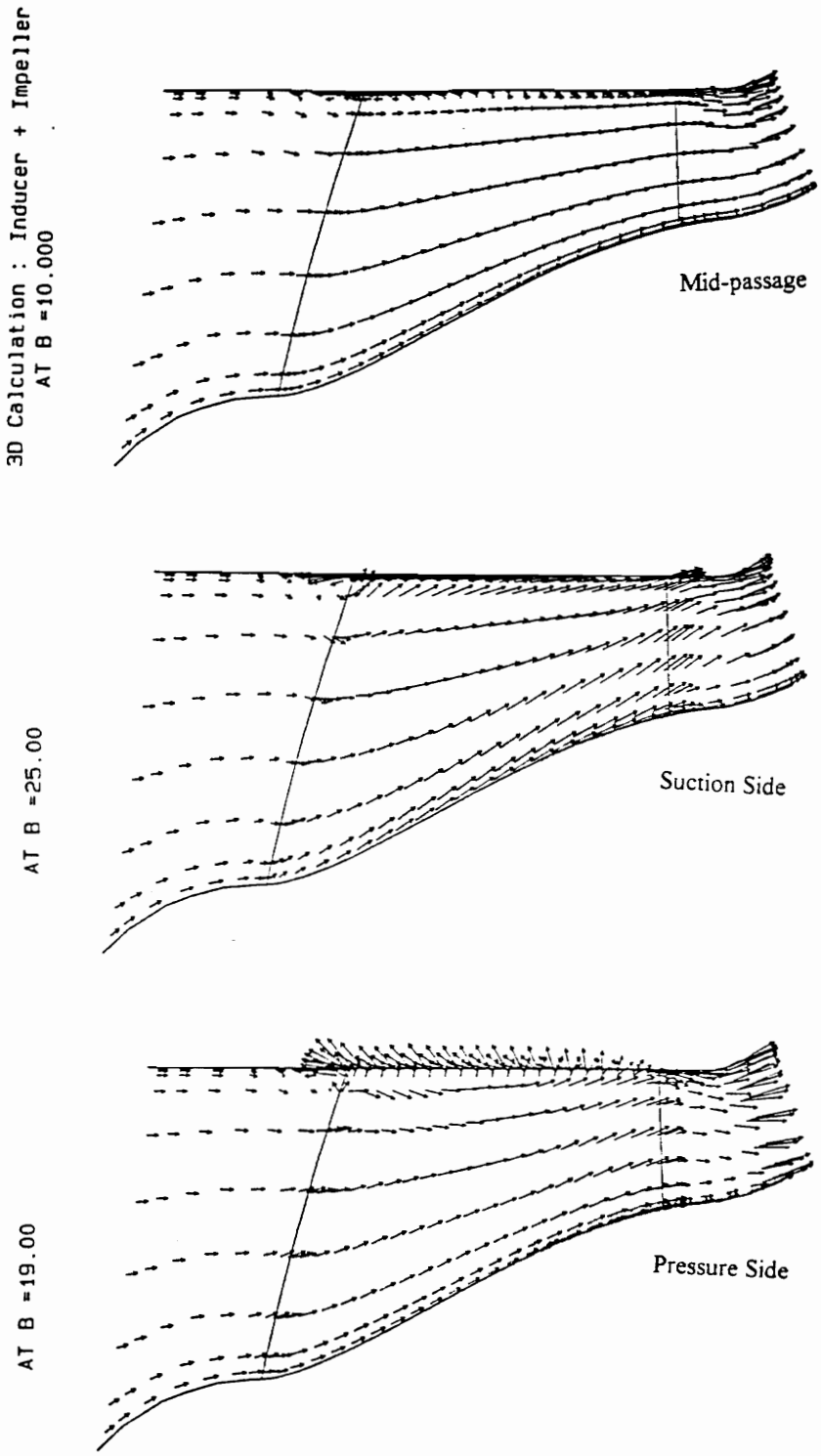


*Figure 29 : Meridional view of velocities in the inducer .*

### 5.4.2: Rotary stagnation pressure :

Figure 30 shows meridional views of the rotary stagnation pressure at the inducer mid-passage, the near-wall SS and the near-wall PS .

On each of the three planes, the extent of the LE vortex upstream of the LE is clearly seen in the loss contours. On the SS, the tip vortex also extends a short distance into the passage .

The SS shows a high loss fluid region in the tip gap where losses are generated. Tip gap secondary velocities behave as a jet that convects losses across the passage from tip SS to tip PS. Because all the high loss fluid does not go through the gap, some of these losses accumulate at the tip PS and are even convected from the tip PS towards the hub PS. As can be seen from the velocity vectors (Fig. 29), this radially inward movement on the PS does not extend below one fourth of the blade height from the tip. Thus, losses coming from the PS tip meet losses coming from the lower part of the blade (centrifuging of the boundary layer), accumulate at the meeting region on the PS and generate the gradual distribution that is observed .

Eventually, losses are convected by the streamwise primary flow and contribute to the losses downstream of the inducer .

### 5.4.3: Inducer Leading Edge vortex :

Figure 31 shows the circumferential variation of the inducer LE vortex in cross-sectional views ($\theta$,R views) .

At the first plane (A=-0.13), the pronounced axisymmetry of the LE vortex can be noticed. This circumferential uniformity is barely affected by the inducer blade (2nd plane) : the rotary stagnation pressure coefficient P* remains circumferentially uniform. Just upstream of the LE, the presence of the blade is felt and a loss core appears at the Suction Side (SS) with P*~-0.4. Right after the LE, the vortex still looks circumferentially uniform with a high loss core at the SS tip. The LE vortex looks like a stationary ring of shear where no streamwise convection occurs in the inducer blade passage, i.e., the primary convection is not strong enough to affect the induced velocities. Because of non-zero incidence (see vectors section 5.5.2) and high rotation speed, a region of high blade-loading is present at the swept-back inducer tip LE. That strong pressure difference between PS and SS generates strong backward velocities of up to

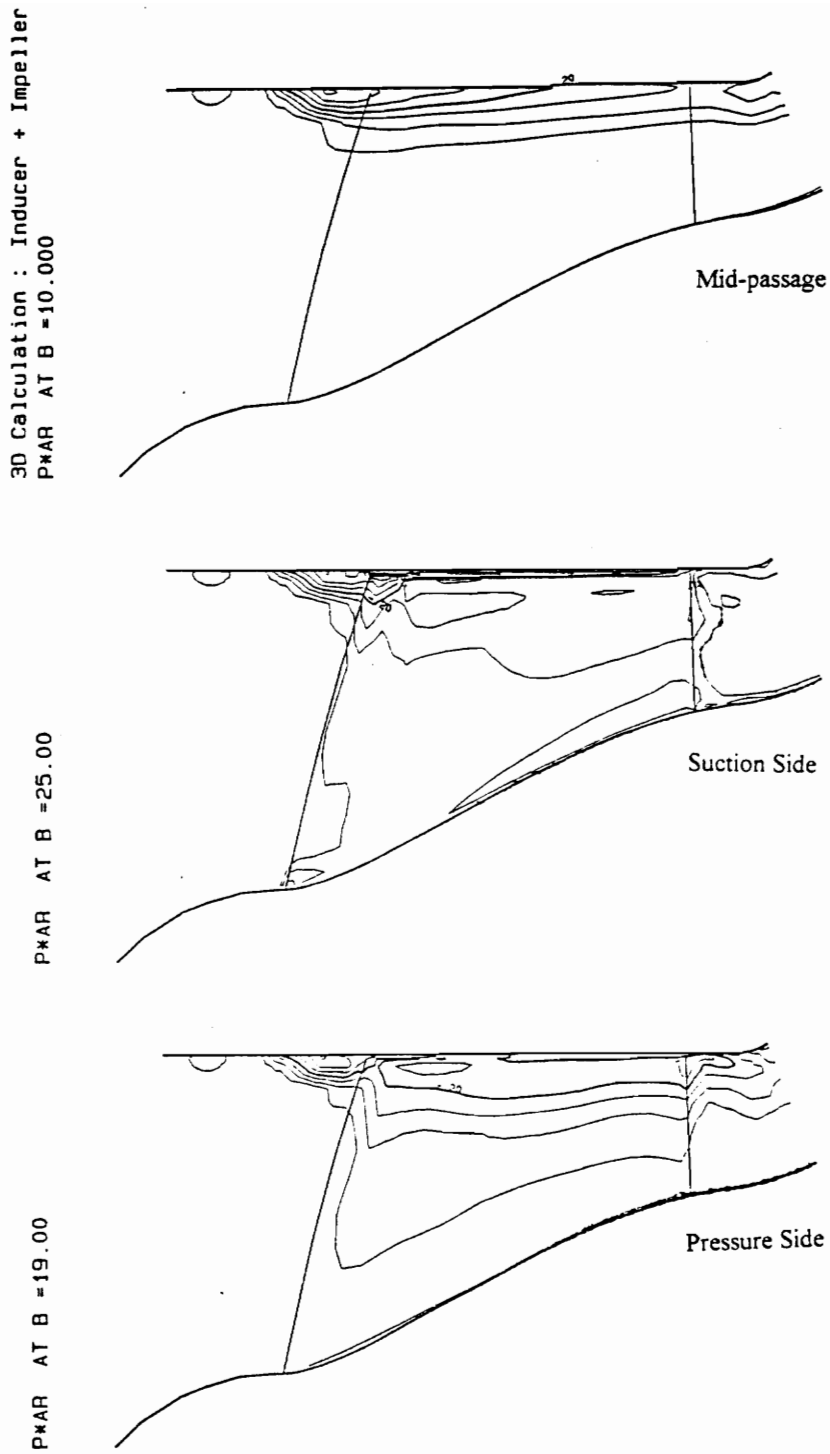


***Figure 30 : Meridional view of rotary stagnation pressure, P*, in the inducer . Contour interval 0.05,0.2 .***

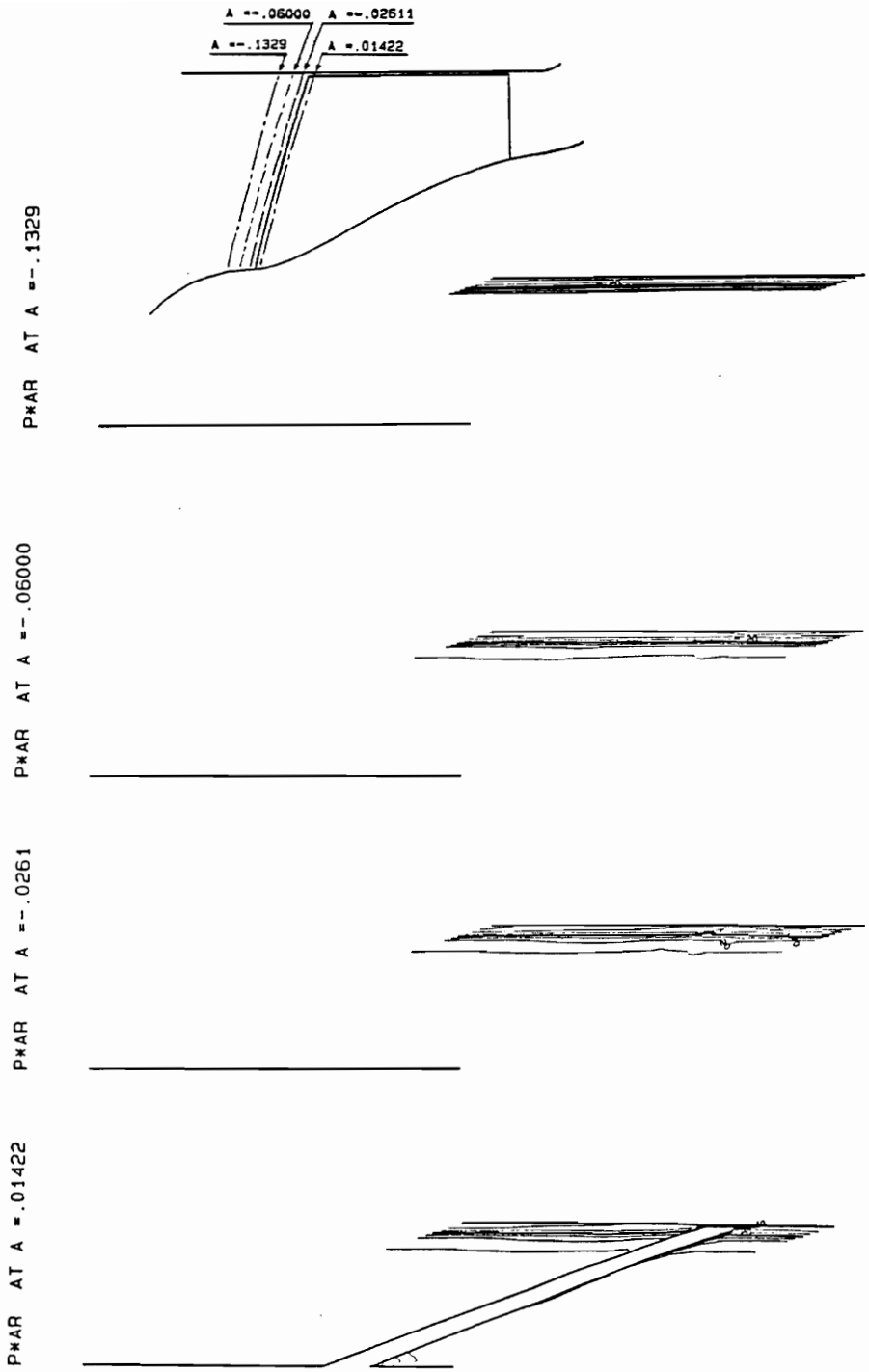


*Figure 31 : Cross-sectional views of the inducer leading edge vortex .*

approximately 100m/s. These velocities are large compared with the mean axial convection .

### 5.4.4: Static pressure and blade-loading :

Figure 32 shows the static pressure coefficient P at mid-passage, on the SS and the PS of the inducer .

On the PS, the static pressure increases from about 0.05 to 0.3 in the middle of the blade, and then slowly decreases towards the TE with a minimum of 0.2 . This region where the static pressure decreases corresponds to the uncovered part of the blade in the blade-to-blade view (see section 5.5.4) .

On the SS, the pressure rises continuously from about -0.05 at the LE to 0.35 at the TE. At the LE, the tip section has very low static pressures. This region where P is lower than -0.05 (possibility of cavitation inception) is not emphasized here since it will be discussed and detailed in section 5.8 .

Figure 33 shows the static pressure difference between the PS and the SS of the blade, i.e. the blade loading. The static pressure difference rises from 0.04 at the hub LE to 0.22 at the tip LE. This strong pressure peak contributes to the formation of the LE vortex (see 5.4.3) because the flow is forced to go around the blade by a strong pressure gradient .

From LE to TE at the hub, the blade loading rises from 0.04, reaches a maximum of 0.14 at mid-length, and decreases towards the TE. In the tip region, the loading is very high before the middle of the blade with a maximum of 0.24. After 2/3 of the blade chord, the loading decreases uniformly towards the TE, and is constant from hub to tip. The last 6th of the blade is negatively loaded with a minimum of -0.12 at the inducer TE. This suggests that more pressure rise would be achieved by the inducer if the last third of its length was kept with a constant or increasing blade loading. The negative loading at the TE implies that the SS now becomes a pressure side, and vice-versa for the PS .

As a comparison with previous SEP results [17,18], this inducer is much more highly loaded, with an average factor of 3 with [17] and 2 with [18]. The loading pattern is different in the sense that the present loading is much more regular, but the TE unloading coefficient is approximately the same (-0.1). The core of the high-loaded region (near tip, first third of the blade) is more pronounced in this case .

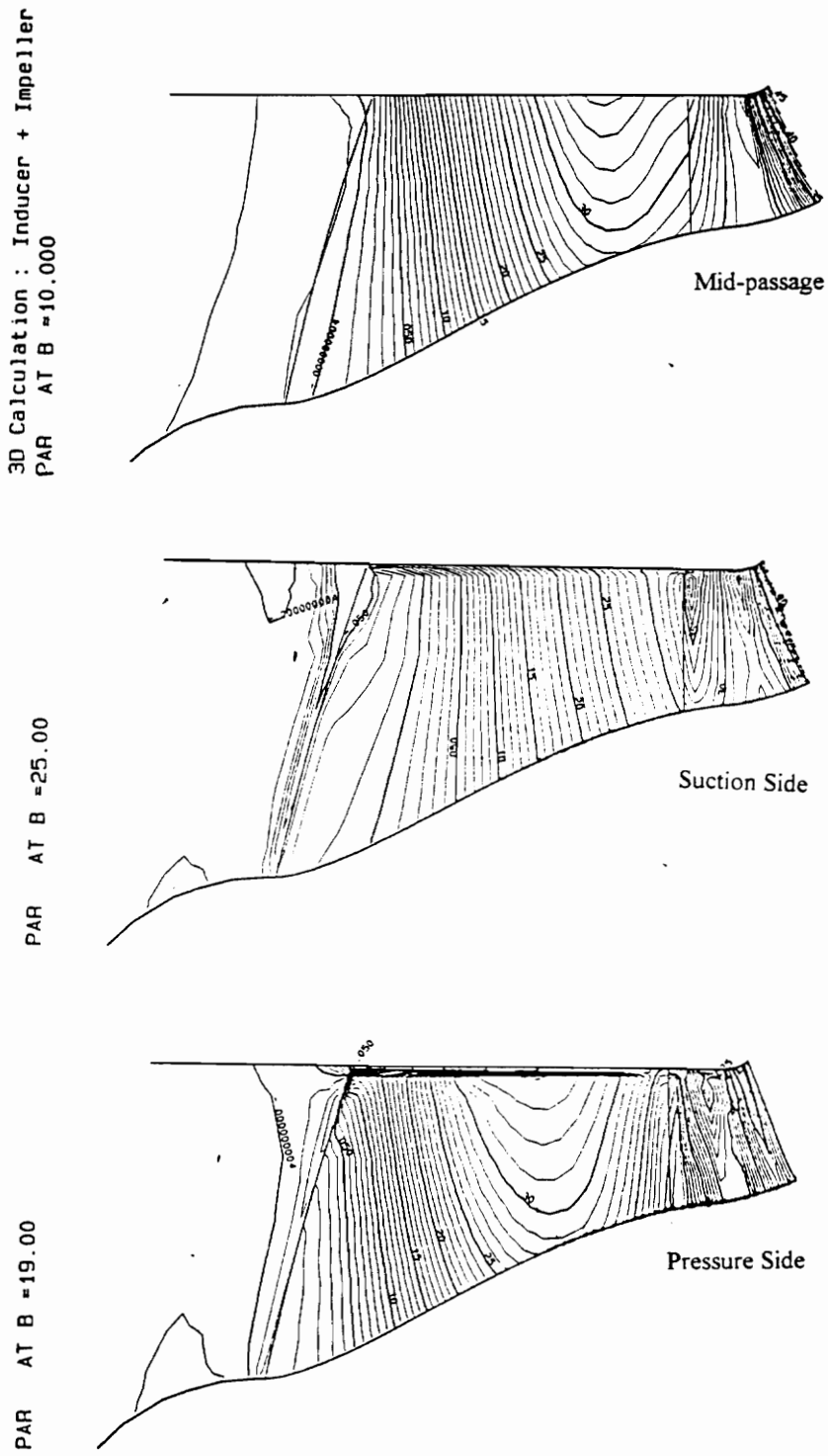


***Figure 32 : Meridional view of the static pressure, P, in the inducer . Contour interval 0.01,0.05 .***

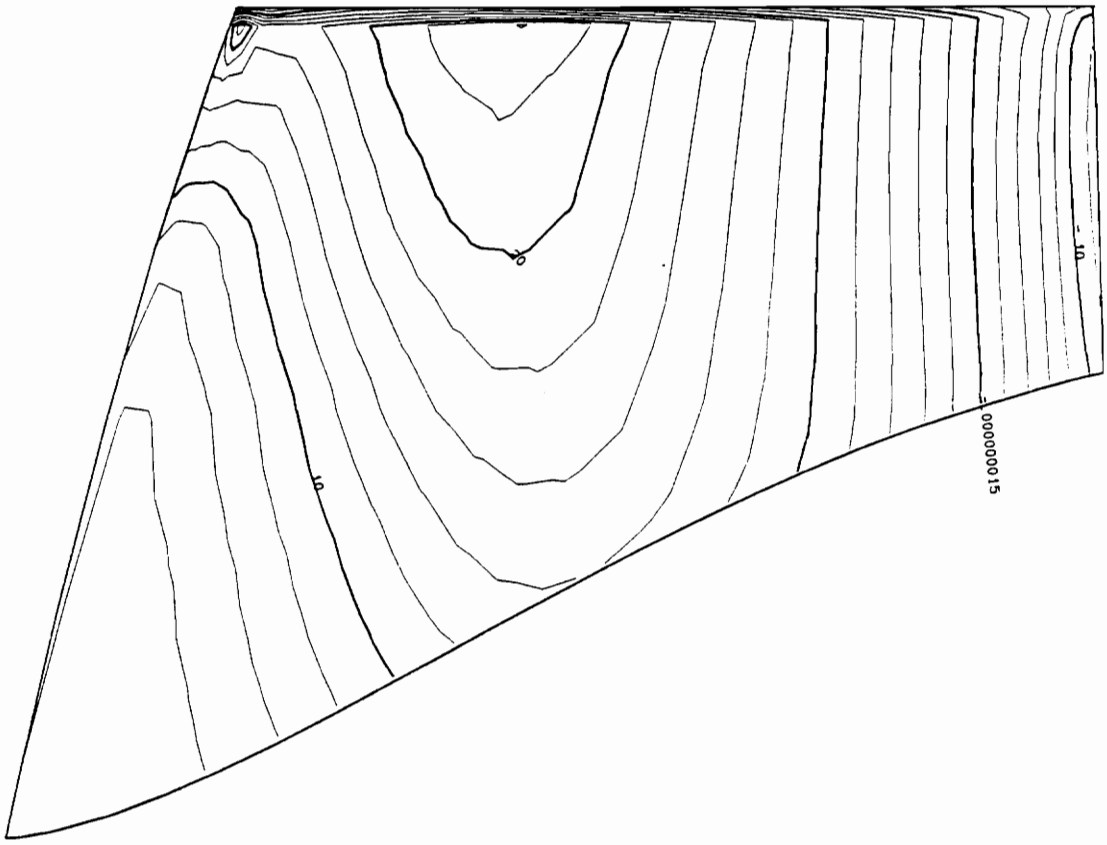


*Figure 33 : Meridional view of the inducer blade loading .*
*Contour interval 0.02,0.1 .*

Also of interest is the behavior of the blade loading at the inducer tip section where unloading occurs. This phenomenon is due to the fall in pressure at the pressure side tip corner sucking the flow into the tip gap (Fig. 32). The pressure drop is expected to occur over about one tip gap height on the pressure surface [41]. Here, the pressure drop is captured over one grid cell, between the tip grid line at k=10 and the k=9 line which is about one tip gap height back on the blade (see Section 4.5.1.2) .

## *5.5 Blade-to-blade results for the Inducer and the Impeller .*

### 5.5.1: Definition of the unrolled blade-to-blade view :

The following analyses are based on unrolled blade-to-blade views (θ,s planes) for different k-layers (C=0.024 : near-hub ; C=0.62 : near mid-height ; C=0.9912 : inducer tip). The unrolled meridional distance s is defined by :

$$ds = \frac{\sqrt{dr^2 + dz^2}}{r} \qquad (5.8)$$

Two θ repeats are used so that the flow trend can be better appreciated .

### 5.5.2: Velocity vectors :

Figures 34 to 36 show the velocities from hub to tip in the blade-to-blade view.

At hub and mid-height, velocities upstream the inducer LE are fairly uniform and oriented towards the blade LE. Very little deviation occurs when velocity vectors go around the blade, i.e., no backward flow is observed. For the inducer, the incidence is approximately 2.5 degrees at the hub, 2.8 degrees at mid-height and 4.8 degrees at the tip.

Inside the inducer blade passage at hub and mid-height, the flow behaves smoothly with lower relative velocities on the PS, and slightly higher velocities on the SS. Upstream of the tip, the velocities are essentially tangential in the LE vortex. As the tip is approached, the axial component of the velocity becomes more negative as the flow spills upstream due to the high blade loading. Downstream of the leading edge, the velocities again become tangential, and they finally have a positive axial component near the TE .

At the inducer exit, the flow provides the impeller with a quite uniform inlet distribution. Both main passages see approximately the same inlet flow, so that the flow split is 50%/50% .

There is a tendency of the flow to spill from pressure side to suction side just upstream of both impeller main blades, and especially through the inducer/impeller gap. The flow then accelerates around the suction sides of the leading edges as it enters the impeller passages. At hub and mid-height, the more tangential flow between the inducer TE and the leading edge of MB1 may be partly due to the inducer/impeller interaction .

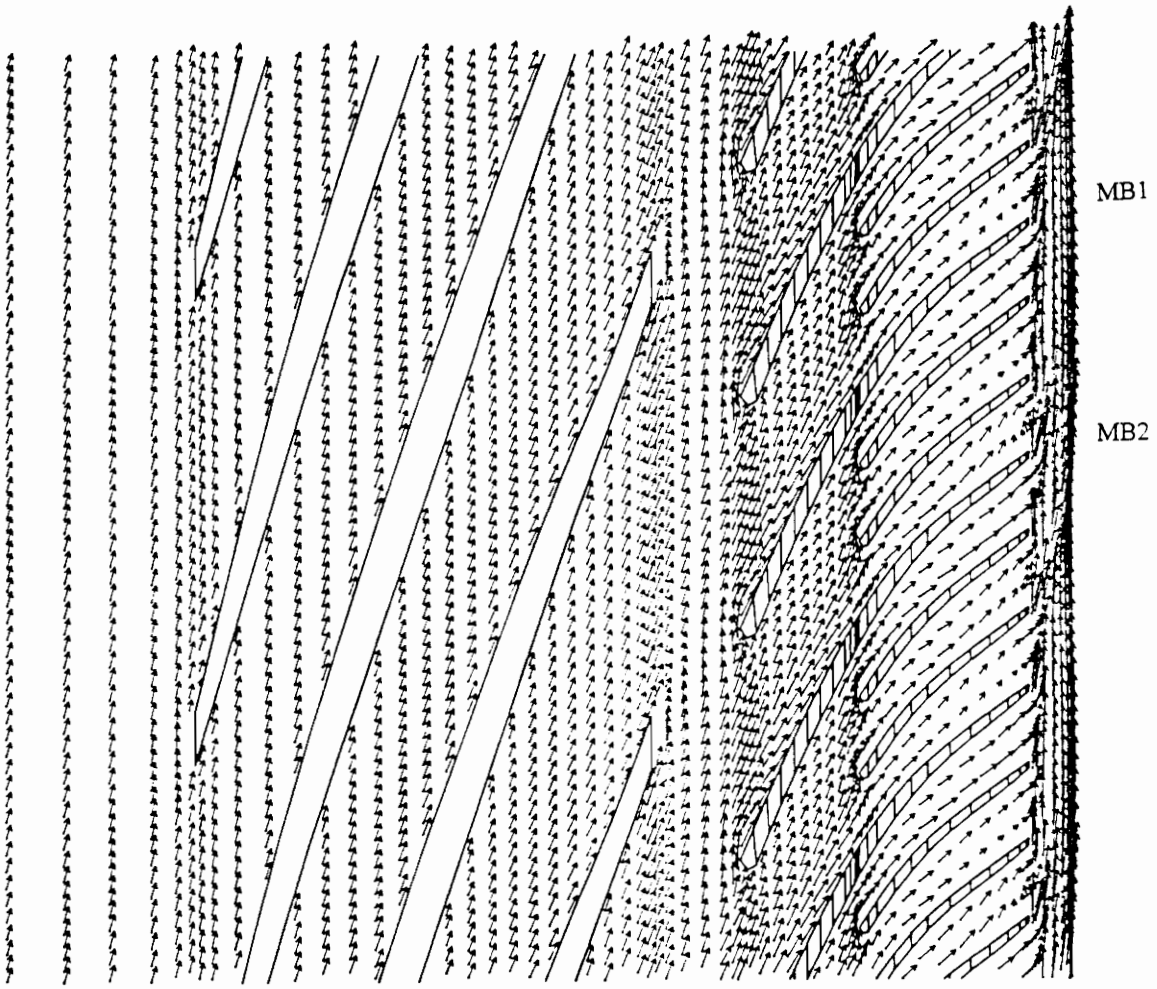


*Figure 34 : Blade-to-blade view of velocity vectors through the inducer and the impeller, near the hub .*

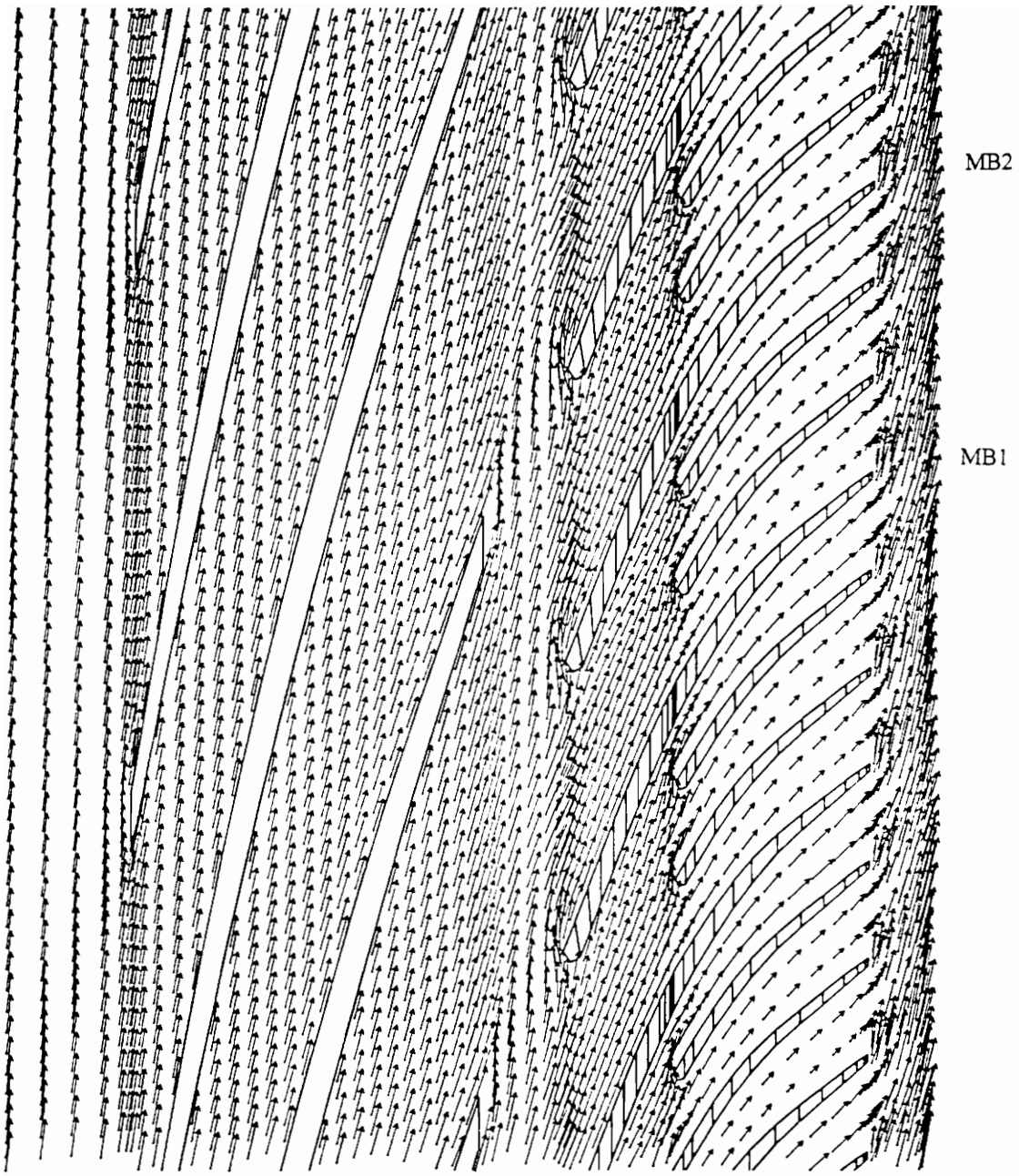


***Figure 35 : Blade-to-blade view of velocity vectors through the inducer and the impeller, near mid-height .***

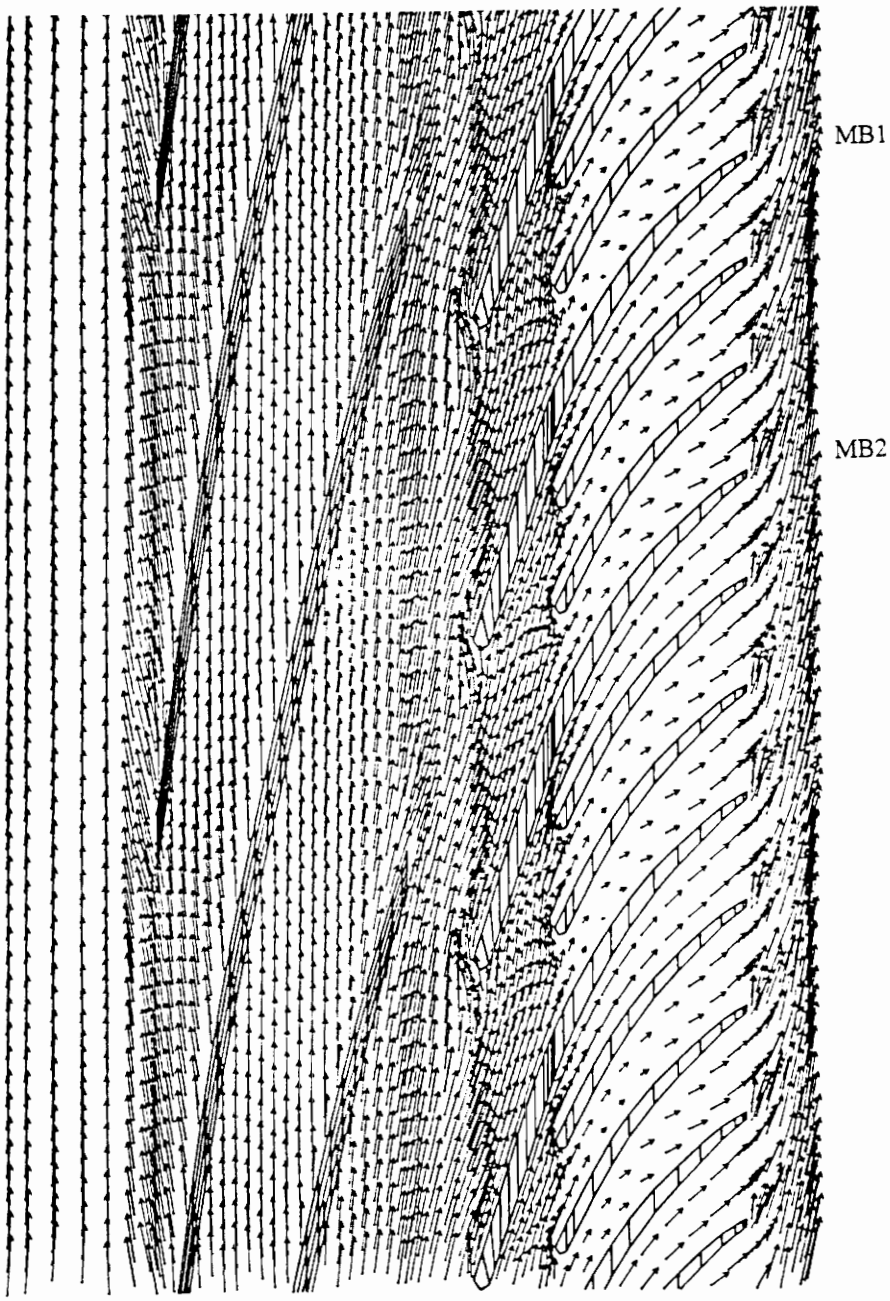


*Figure 36 : Blade-to-blade view of velocity vectors through the inducer and the impeller, near the tip .*

In the main blades passages, the flow behaves smoothly from hub to mid-height with high relative velocities at the SS, and smaller ones on the PS .

In the splitter blade passages, there is considerable variation in the velocities. At the hub, there are near-stall conditions on the suction side of the lowest flow passages, (MB1-SP3 and SP1-SP2), towards the TE. These same passages have near-stall conditions near the shroud SS at about one third of the splitter blade chord. The highest flow passages, next to the pressure sides of the main blades, show little secondary flow. The lower flow passages show secondary flow movement on the shroud from pressure to suction side, and some smaller secondary flow movement from suction to pressure side at the hub .

At the impeller exit, the flow leaves the impeller with high deviation angles, as expected .

### 5.5.3 : Rotary stagnation pressure :

Figure 37 shows a blade-to-blade view of rotary stagnation pressure at mid-height.

Upstream of the inducer, the flow is loss free. The inducer mainly develops a boundary layer on each of its sides, with thicker development on the suction side .

In the inducer/impeller gap, the mid-height flow is again almost loss-free .

Loss generation at the impeller main blades LE and splitter blades LE can clearly be seen, and is mainly due to high incidence and blade thickness. Losses accumulate mostly on the SS of the passages .

The impeller has low losses upstream of the splitters LE except on the main blades suction sides. At mid-height, the passages adjacent to the PS of the main blades have very low losses compared to the other splitter passages .

The impeller main blades LE losses cover the blades SS, which implies low flow rates for the splittered channels MB1-SP3 and MB2-SP1. Channels which seem unaffected by this loss development (SP2-MB1 and SP4-MB2) have the highest flow rates (as seen in Fig. 28) though their inlet areas are smaller compared to the other passages. This realignment of the flow causes incidence on the splitter blades, especially SP1 and SP3, which in turn causes the loss generation on the SS of the splitter blades LE. This can be seen in Fig. 37 .

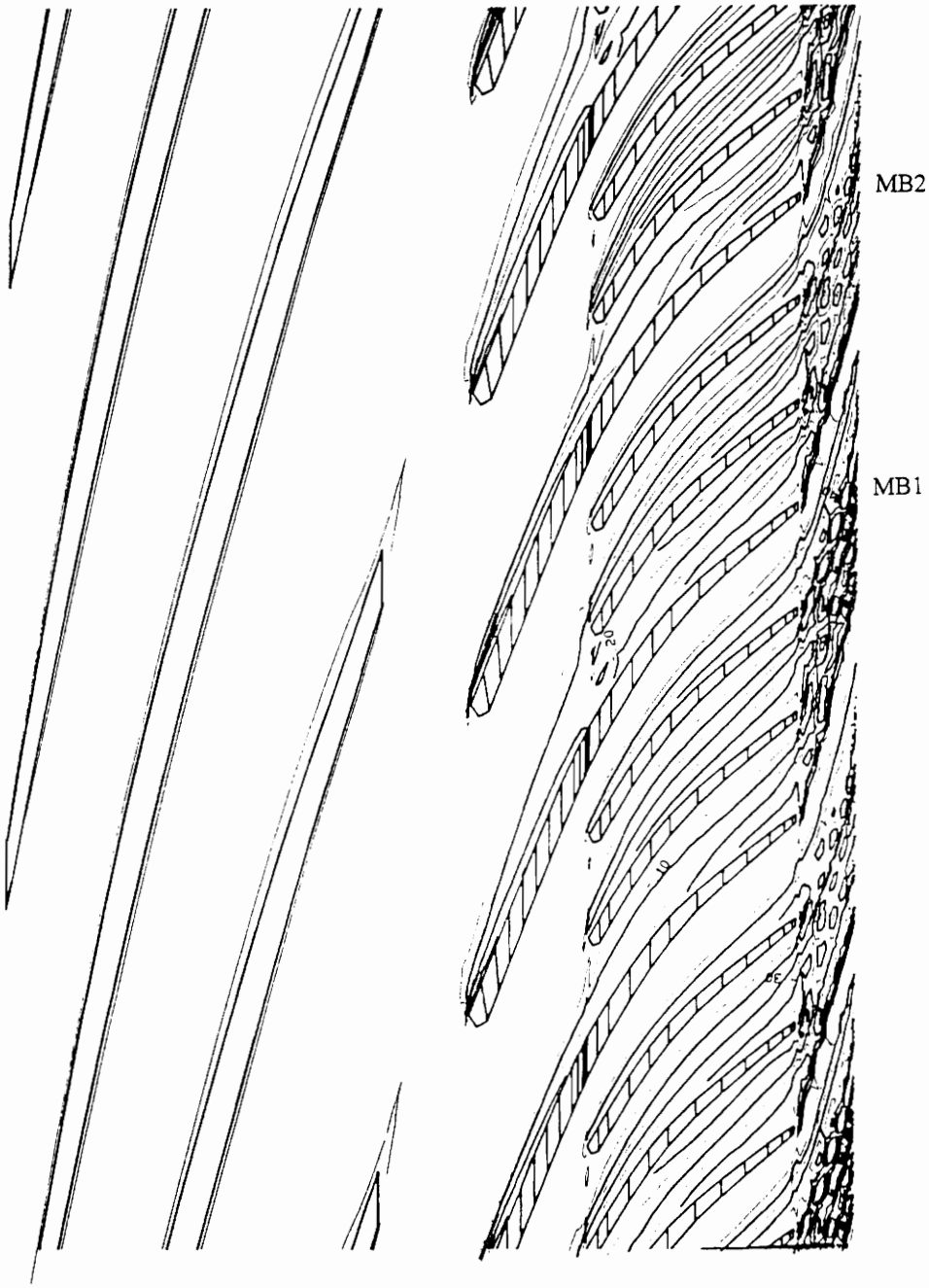


***Figure 37 : Blade-to-blade view of rotary stagnation pressure through the inducer and the impeller, near mid-height . Contour interval** 0.05,**0.1** .*

### 5.5.4 : Static Pressure at the Exit of the Inducer : Influence on the Inter-Blade Gap .

Figures 38 to 40 show the static pressure in the unrolled blade-to-blade view at the hub, mid-height, and inducer tip sections .

As was seen in section 5.4.4, the static pressure on the SS of the inducer keeps rising till the TE is reached. On the PS, the pressure keeps increasing till the pressure surface is no longer covered by the SS of the previous inducer blade. Thereafter, the pressure slowly decreases, so that the net loading of the blade decreases and even becomes negative at the TE .

The blade loading level can be seen by plotting (Fig. 41) the isentropic relative velocity on each side of the blade (near-wall grid lines) for different heights. Relative velocities are mostly greater on the SS than on the PS, except at the TE where the negative loading occurs, i.e., the PS becomes the SS and vice-versa .

The inducer blade TE has a suction peak on the PS and a pressure peak on the SS at the hub and at mid-height. This is caused in part by the chamfered TE shape. Correspondingly, the blade wake at these heights is more tangential as shown in Figs. 34 and 35. This is due to the local pressure gradient that is normal to the flow at the inducer TE (on the PS) and which causes the flow to turn around the inducer TE .

For both main blades, the flow going around the LE generates low pressure peaks on the SS. These peaks which are due to high incidence (section 5.5.2) and high LE blade loading (see section 5.7.2) might results in impeller LE cavitation (see section 5.8)

The high loading of the impeller blades sets up the pressure distribution for the second half of the inter-blade gap. Pressure contours that start on the impeller LE and turn and go back into the impeller extend upstream only about half the gap distance. Some pressure contours extend from the inducer TE and go through the impeller. The influence of the impeller on the inducer pressure distribution will be the subject of section 6.0 comparing the inducer results with and without the impeller .

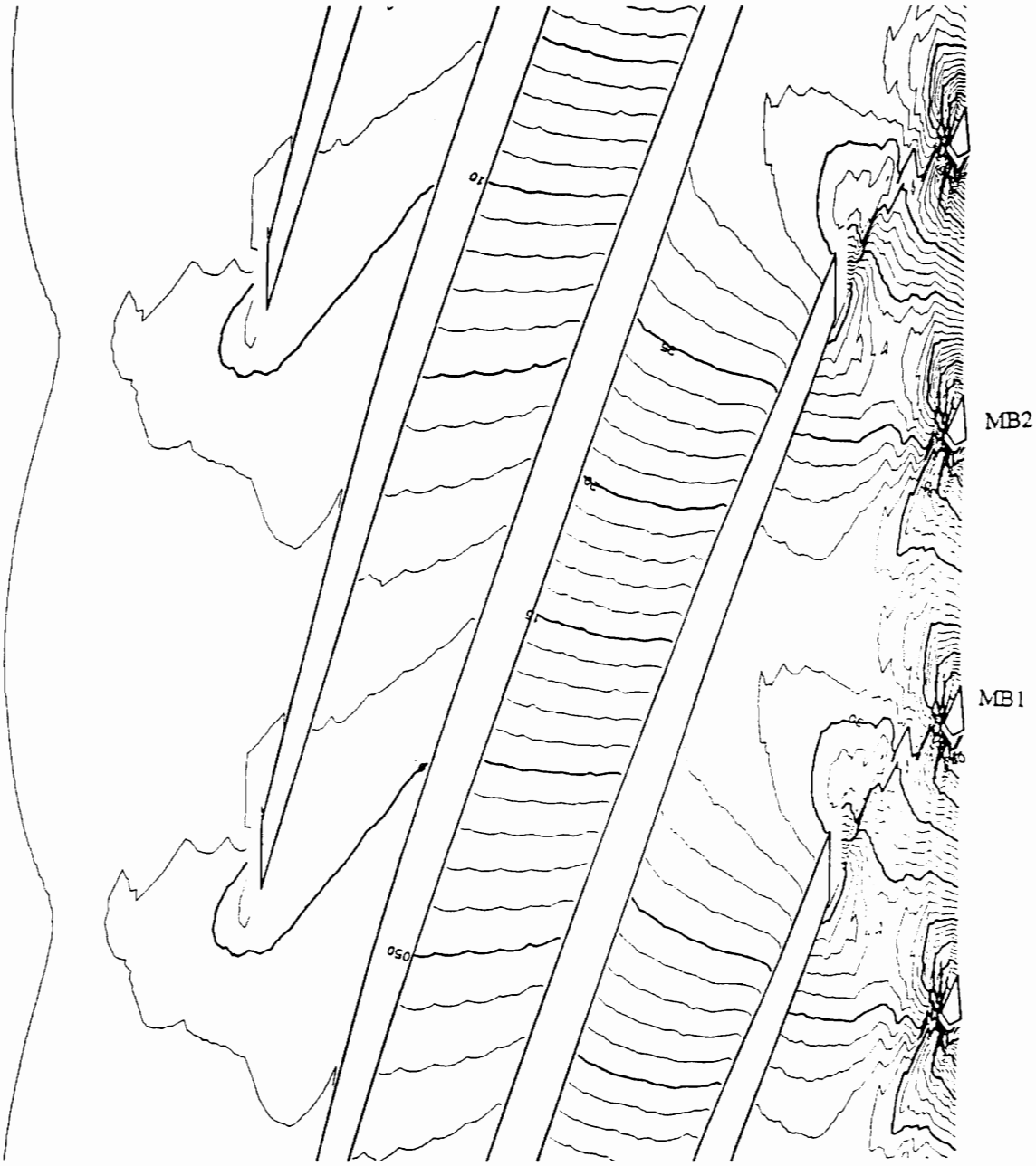


***Figure 38 : Blade-to-blade view of the static pressure in the inducer and the inter-blade gap (hub) . Contour interval 0.01 , 0.05 .***

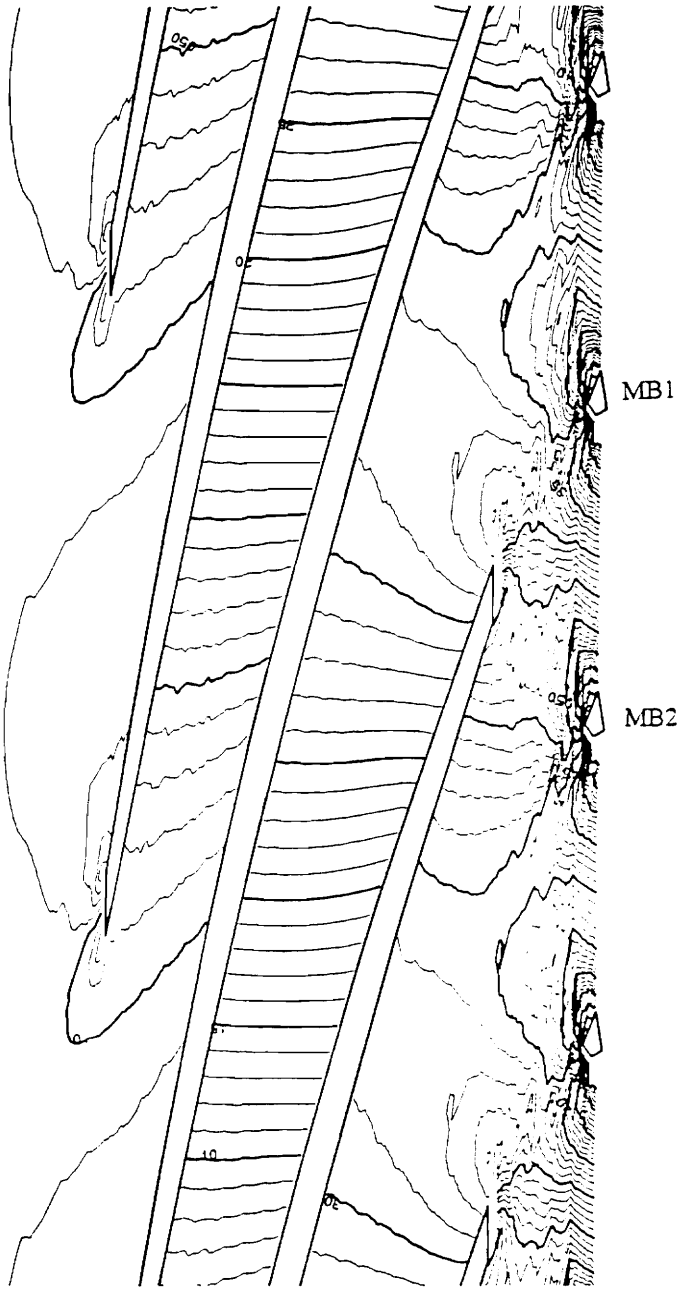


*Figure 39 : Blade-to-blade view of the static pressure in the inducer and the inter-blade gap (mid-height) .*

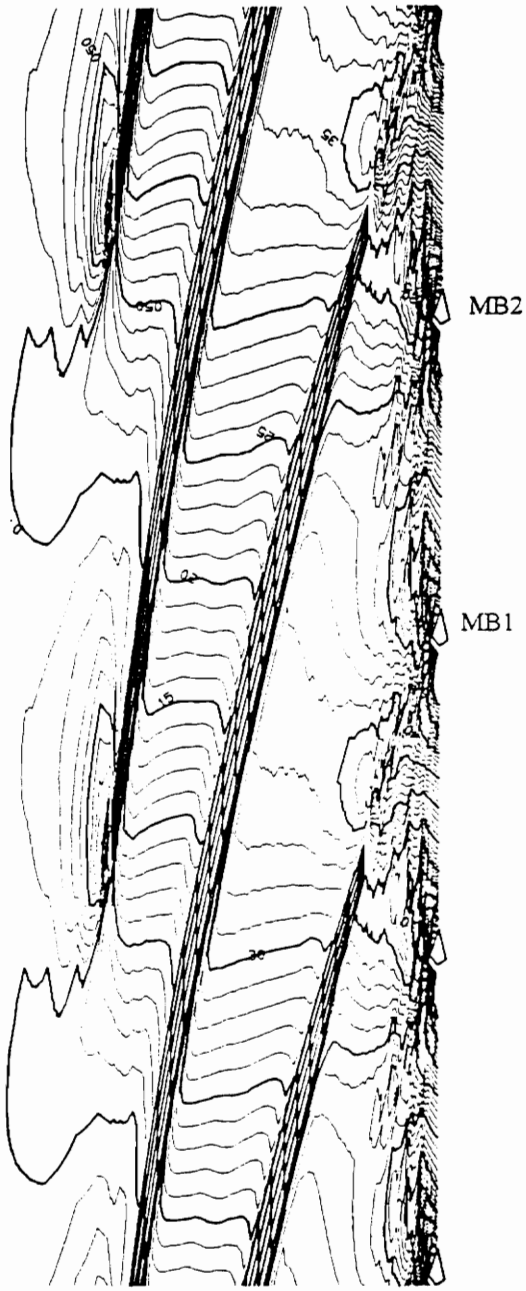


***Figure 40 : Blade-to-blade view of the static pressure in the inducer and the inter-blade gap (tip) .***

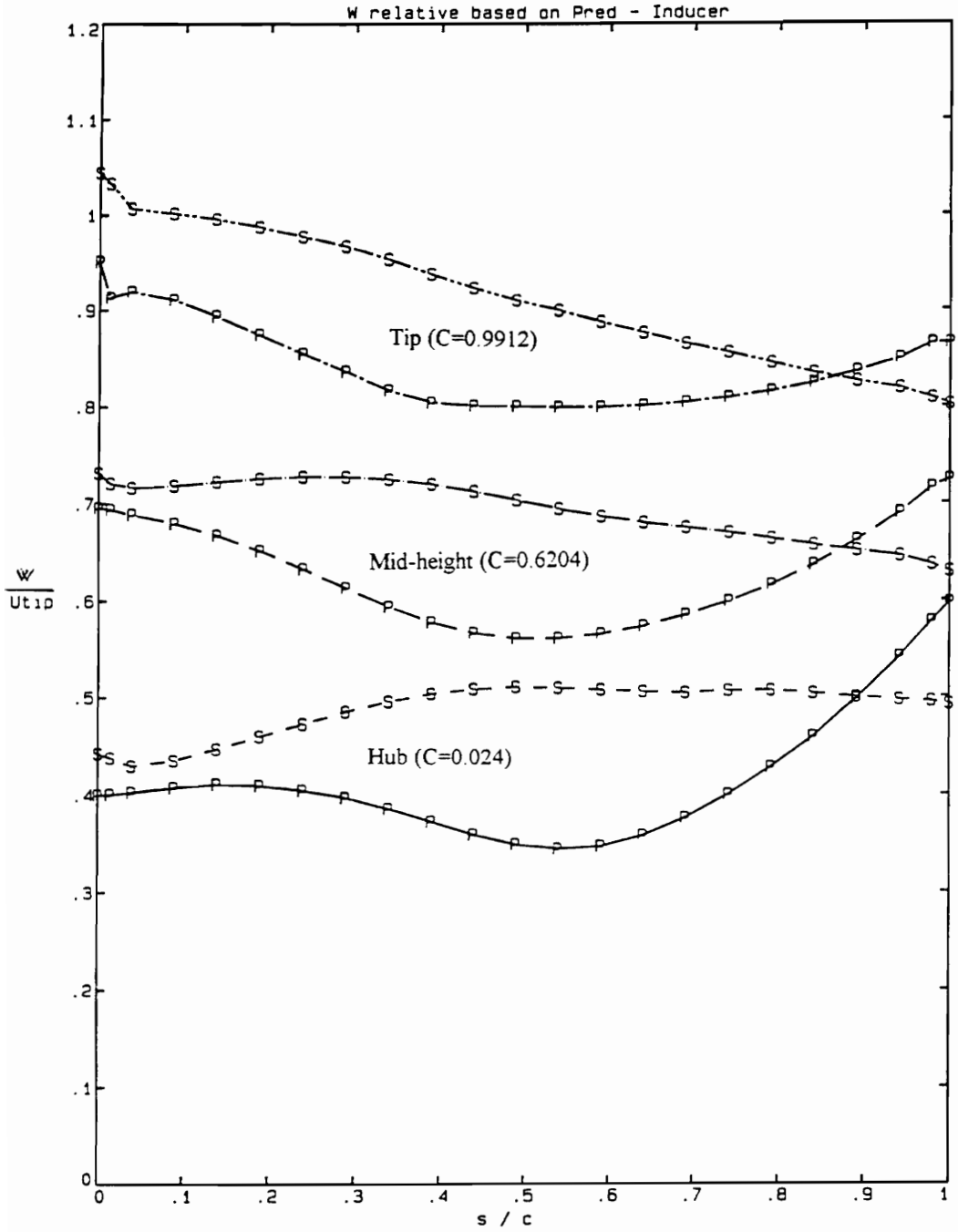


*Figure 41 : PS and SS isentropic relative velocity in the inducer .*

## *5.6 Loss Build-up through the Tandem Inducer/Impeller .*

Figure 42 shows how the losses develop and convect throughout the inducer and impeller flow field. Losses are shown on nine cross-sectional i-planes from the pump inlet to the diffuser .

At locations of particular interest :

* At the inlet plane on the spinner, the boundary layer losses are not seen because they are very small compared with losses generated in the inducer and the impeller .

* At the inducer LE, the losses at the shroud are due to the circumferential tip vortex. There is a small loss core due to incidence in the hub SS corner .

* At the inducer TE, losses accumulate on the shroud towards the PS because of the combined effect of the centrifuging of the boundary layer (radially outward meridional velocities on Fig. 29) and the tip-leakage flow that convects losses across the passage from tip SS to tip PS. This mechanism also explains the reduction of losses on the SS near the tip .

* In the inducer/impeller gap, the loss distribution changes very little. Losses remain at the shroud and there is little evidence of a blade wake .

* At the impeller LE, the previous losses are fairly equally split between both impeller main passages. Losses are also generated due to high incidence on the SS of both impeller main blades .

* Just before the splitters' LE, losses are mainly concentrated on the shroud and SS of the main blades. Pressure sides are low loss regions .

* At the splitters LE, the high losses on the SS of the main blade MB1 create a low flow rate in passage MB1-SP3 (see 5.3.2, Fig. 28). Passages SP2-MB1 and SP4-MB2 are on the pressure sides of the main blades and are low loss channels, and therefore have high flow rates. The middle splitter passages surprisingly appear to behave differently relative to the main blades SS passages. Passage SP1-SP2 has 13.9 percent flow compared to 16.0 percent for passage MB2-SP1, while passage SP3-SP4 has 15.2

percent compared to only 12.8 percent for passage MB1-SP3. Passage MB2-SP1 appears to have more loss at the inlet than SP1-SP2. However, on a mass-averaged basis, it has less loss, as shown in Table 5 :

***Table 5 : Relationship between losses and flow split.***

| Passage | Flow rate | $P^*_{inlet}$ | $P^*_{exit}$ |
|---|---|---|---|
| MB2-SP1 | 16.000 % | -0.123 | -0.169 |
| SP1-SP2 | 13.888 % | -0.150 | -0.186 |
| SP2-MB1 | 20.487 % | -0.092 | -0.126 |
| MB1-SP3 | 12.776 % | -0.172 | -0.213 |
| SP3-SP4 | 15.202 % | -0.143 | -0.184 |
| SP4-MB2 | 21.647 % | -0.072 | -0.098 |

* At the splitters' LE, losses were seen to be mainly near the shroud and SS. As the flow goes through the splitter passages, losses are convected and swirled from shroud to SS to hub, so that the SS and hub SS of the blades are now the high loss regions. Losses increase due to mixing and spread across each passage. Table 5 shows that the mass flow rate per passage increases monotonically with both inlet and exit mass-averaged loss .

* In the diffuser, six high loss cores appear from the wakes of the impeller TE. They are in groups of three, each group being separated from the other by a zero loss region coming from the PS of each impeller main blade .

From the loss distribution in Fig. 42, the three dimensional flow development has been inferred. This is confirmed by the impeller velocities presented in 5.7.1 .

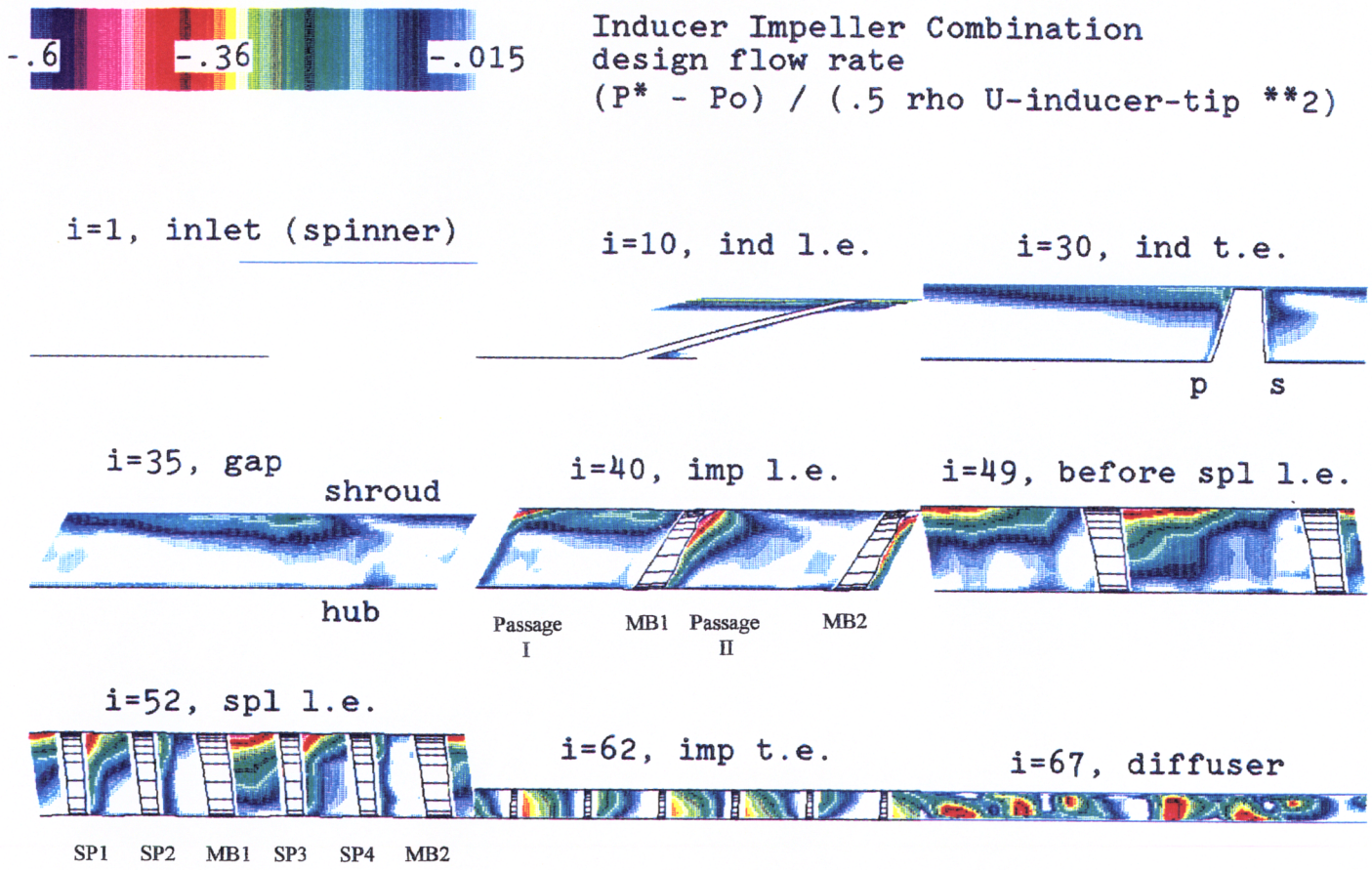


*Figure 42 : Loss build-up through the tandem inducer/impeller combination .*

## *5.7 Flow Analysis in the Impeller .*

### 5.7.1: Meridional Velocities .

Figure 43 shows the meridional velocities for each blade (PS and SS), in the order (bottom left to top right) defined by Fig. 22 (bottom to top). The traces of the LE and TE of the splitters and the main blades have been drawn to locate the impeller .

This figure shows the non-uniformity of the flow for corresponding blades (SP1-SP3, SP2-SP4, MB1-MB2), due to different loss distributions across each passage (see section 5.6). The impeller MB show strong counter-streamwise velocities as the flow goes around the LE. Such a phenomenon does not appear on the splitter blades where the passage flow is more confined. That difference can also be seen in the blade-to-blade velocity vectors, section 5.5.2 .

At the inlet of the impeller, velocities are fairly uniform from hub to shroud for each j-plane. This can be thought of as the results of two opposite phenomena :

_ the high losses near the shroud at the inducer exit decrease the shroud velocities,

_ the meridional curvature increases the velocity on the shroud .

The velocity vectors show the secondary flow patterns corresponding to the movement of the high loss regions shown on Fig. 42. On the SS of the main blades before the splitters LE, the losses convect towards the shroud. There is also convection towards the shroud on the PS of MB1. After the splitters LE, all the SS show either streamwise flow or convection towards the hub ; all the PS show either streamwise flow or convection towards the shroud. From these two trends, it can be inferred that the flow is swirling in each passage (hub to shroud on the PS, and shroud to hub on the SS), which explains the change in loss distribution observed between the splitters LE (losses at the shroud and/or near the SS) and the impeller exit (losses at the SS and towards the hub, Fig. 42). This trend is not true for the two high flow rate passages. Here the SS vectors are streamwise and the losses stay on the SS of the blades towards the shroud (SP2 and SP4) .

Of particular interest is the flow pattern on the SS of MB1 where velocities show the inception of stall in the meridional view. The SS of SP1,SP3 and to a lesser extent MB2 experience the same behavior. In section 5.5.2, the existence of stall inception in the impeller blade-to-blade velocity vectors is less obvious because the vectors plotted are not as close to the impeller walls .

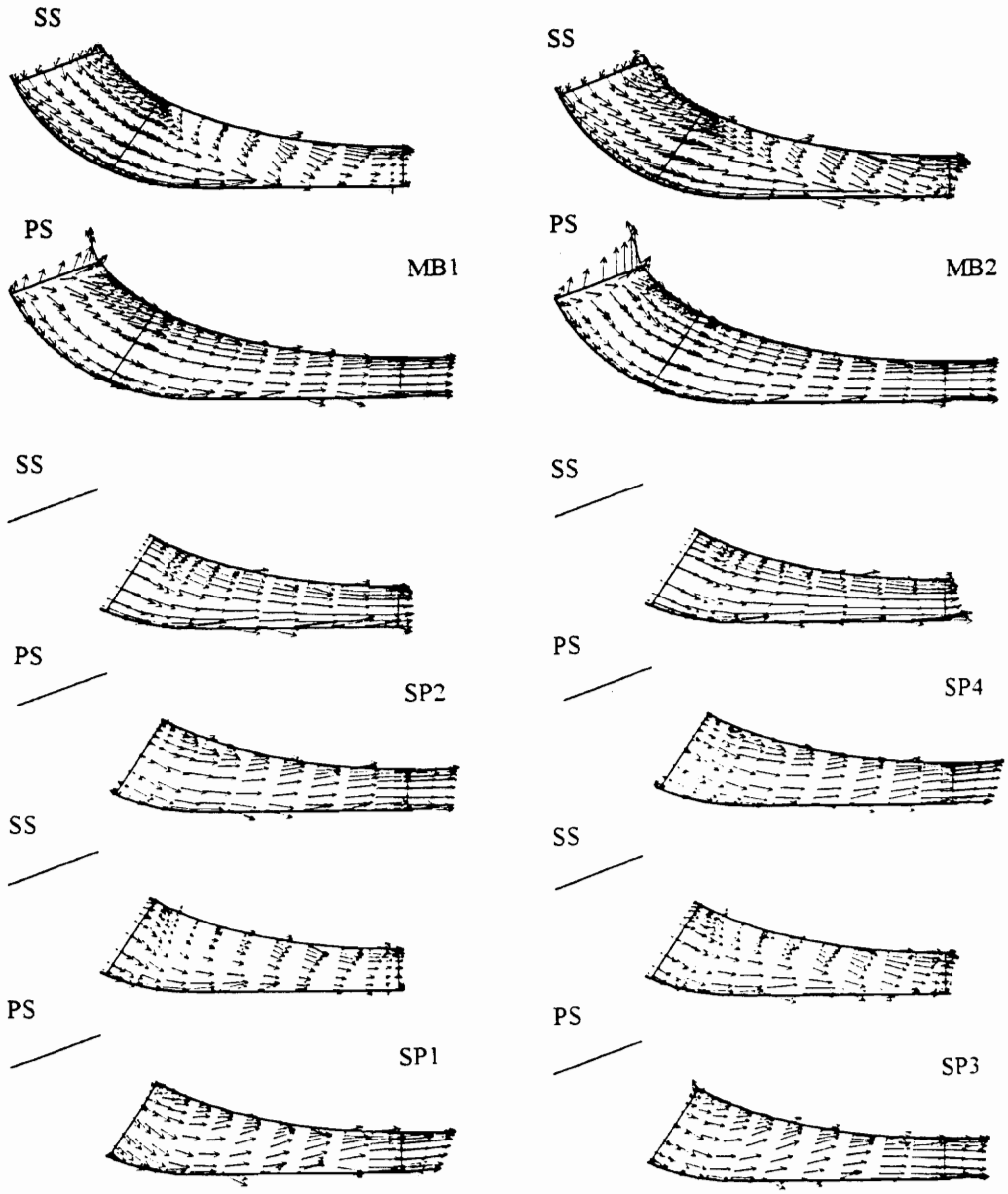


*Figure 43 : Meridional view of the impeller near-wall velocity vectors .*

Close observation shows that stall inceptions are related to the loss distribution (see 5.6) : stall inception occurs in high loss fluid regions such as the suction sides of SP1, MB1, SP3 and MB2. For these regions, SS velocities convect the high loss fluid near the shroud at the beginning of the splitter passages to the hub at the exit of the impeller .

Although stall inception is suggested by these meridional results, a blade-to-blade grid spacing such as in the impeller MB passages would be required in the splitters passages to confirm the extent of this stall phenomenon in each impeller passage (in terms of passage width).

### 5.7.2: Impeller Blade Loading .

The blade loading is defined as being the static pressure difference between the pressure side and the suction side. The blade loading is computed at near-wall grid locations .

Figure 44 shows the blade loading of the different blades SP1, SP2, MB1, SP3, SP4, and MB2 in that order .

The MB are highly loaded at the LE with a maximum pressure coefficient of 0.9 near the blade tips. This high pressure peak generates cavitation problems the same way as for the inducer tip. The loading rapidly decreases to 0.5 over a very small distance, and then continues to decrease till near the splitters LE. At that point, the MB have a negative loading, especially MB2 where the loading goes down to -0.14 near the shroud. After the splitters LE, the loading recovers rapidly, reaching levels of 0.28-0.3 on the main blades near the hub. Thus, in the splitter-bladed region, the blade loading of the impeller main blades is about a factor of 2 smaller than before the splitters, so that the loading is shared by the splitters. On the last sixth of the main blade radial length, the blades experience a strong unloading that goes down below -0.2 .

Similar behavior is noticeable on the splitter blades, which shows again that much higher performance could be achieved if the unloading could be suppressed. A change in the shape of the blades would be necessary to keep the loading as constant as possible, with the value that exists in the middle of the blade at least .

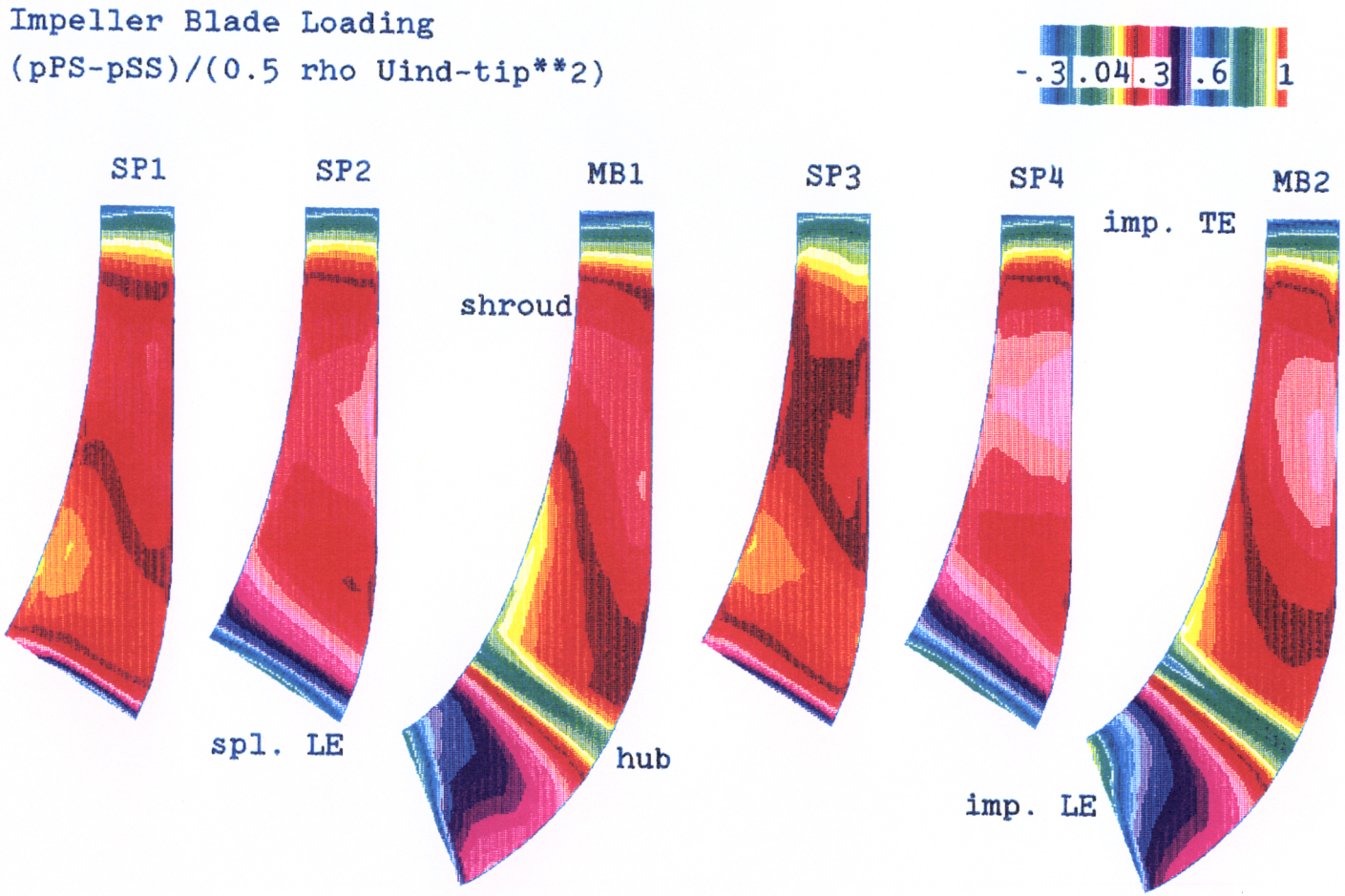


*Figure 44 : Blade loading of the impeller (contour interval 0.2) .*

Whereas at the location of the splitters LE the main blades are lightly loaded, the splitters LE are highly loaded. Cavitation will not occur at that point because the main blades have already increased the pressure enough to P=1.0 . The splitter blades SP1 and SP3 (near the main blades SS) have maximum loading coefficients of 0.45 whereas SP2 and SP4 (near the main blades PS) are more highly loaded at 0.8. This difference can be explained by the loss distribution which is different for each passage (see section 5.6). High loss passages on the SS of the blade create lower loading .

## 5.7.3: Static Pressure :

### *5.7.3.1: Blade-to-blade analysis :*

Figures 45 to 47 show the static pressure throughout the impeller in unrolled blade-to-blade views for different k-layers. These three hub-to-shroud surfaces are the same as those used in the previous results analysis (C=0.024 : hub ; C=0.62 : mid-height ; C=0.99 : tip). As a fraction of blade height in the impeller, these C values correspond to 0.7%, 40% and 91 % respectively .

In the impeller main blade passages, the static pressure increases in planes that are approximately normal to the primary direction. This pattern is similar to the one observed in the inducer blade passage. The pressure rises continuously along the SS of the main blades. On the PS, however, the pressure levels off then falls upstream of the splitter LE. This provides a more uniform static pressure to the LE regions of the splitter blade passages. In fact, the lowest pressures at this meridional location occur between the PS of the main blade and the SS of the neighboring splitter blade. For these passages, the inlet area is smallest, the losses are lowest and the flow rate is highest .

As was also noticed for the inducer, the TE blade unloading occurs on the uncovered part of the pressure sides of the blades (i.e., the PS of blade *n* is not covered by the SS of blade *n-1*). The static pressure is wavy at the impeller TE but quite similar for all passages. By the diffuser exit, the pressure is nearly uniform .

### *5.7.3.2: Blade surface analysis :*

Figure 48 shows the static pressure coefficients (PS and SS) for the two main blades at C=0.62. Not much difference can be seen between the main blades .

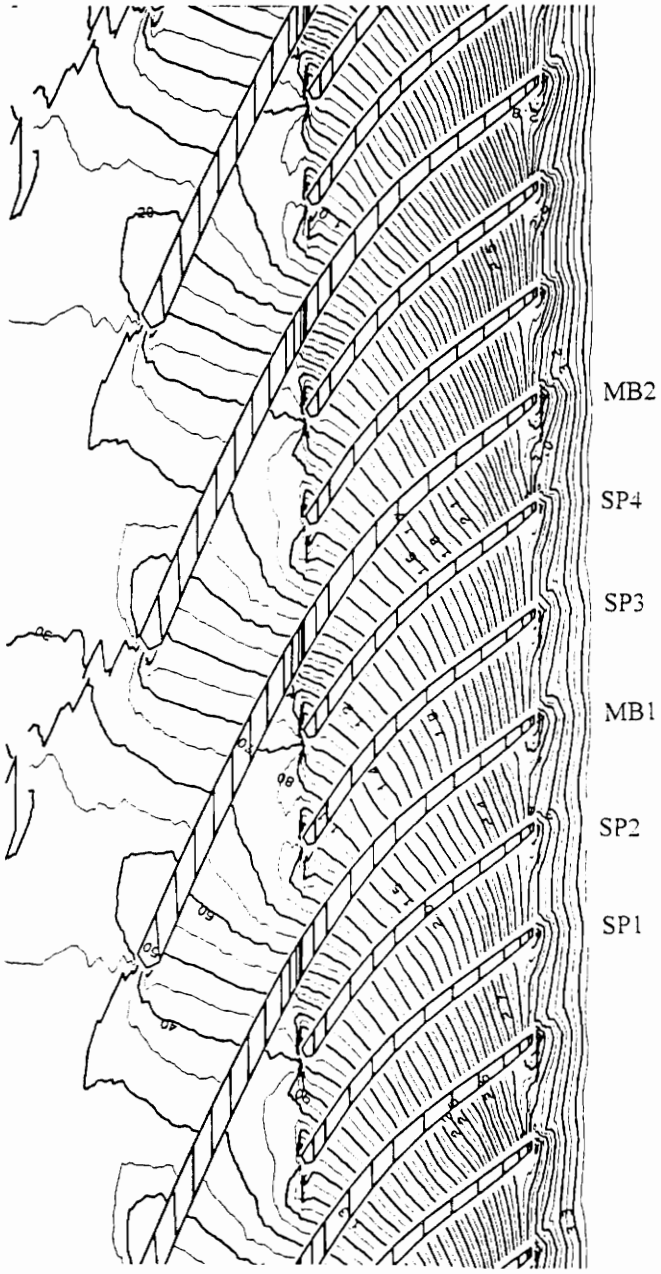


*Figure 45 : Blade-to-blade view of the static pressure in the impeller (hub) .*

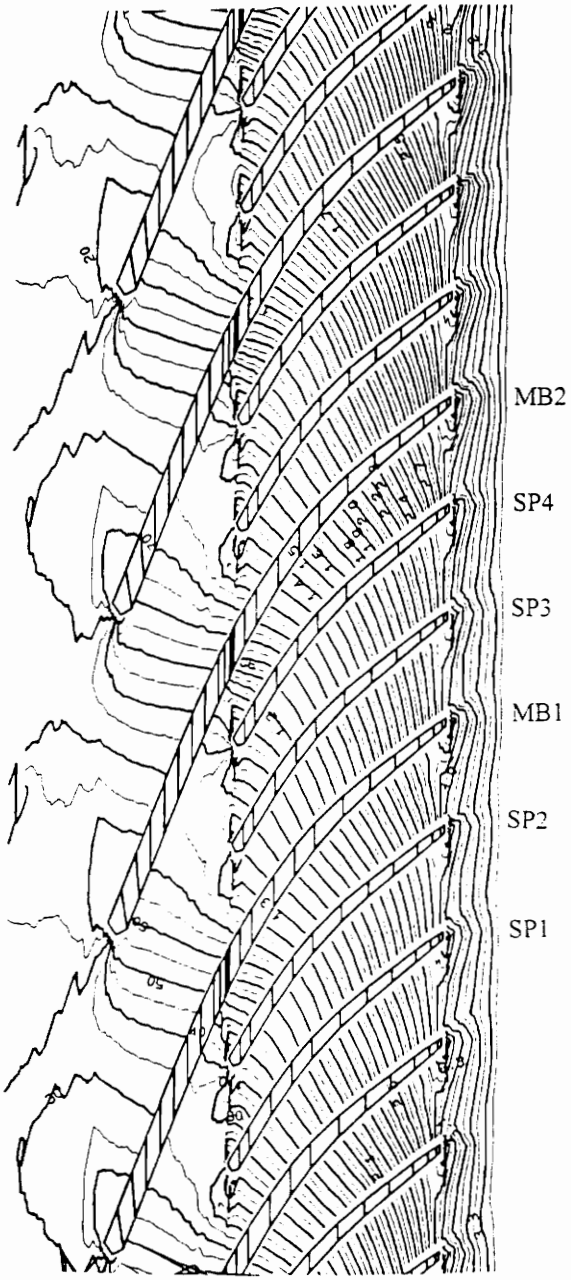


*Figure 46 : Blade-to-blade view of the static pressure in the impeller (mid-height) .*

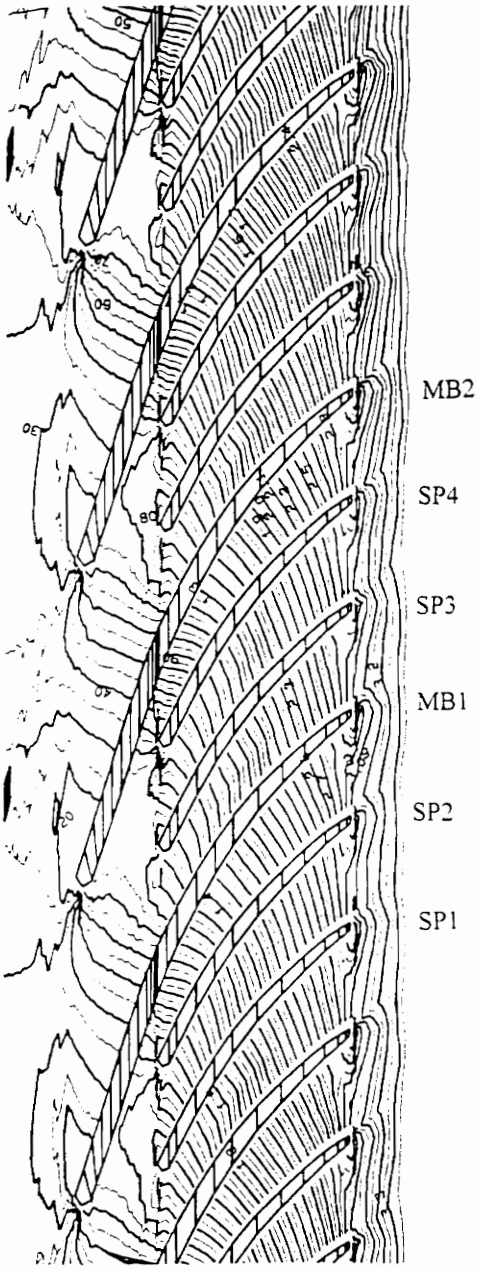


*Figure 47 : Blade-to-blade view of the static pressure in the impeller (tip) .*

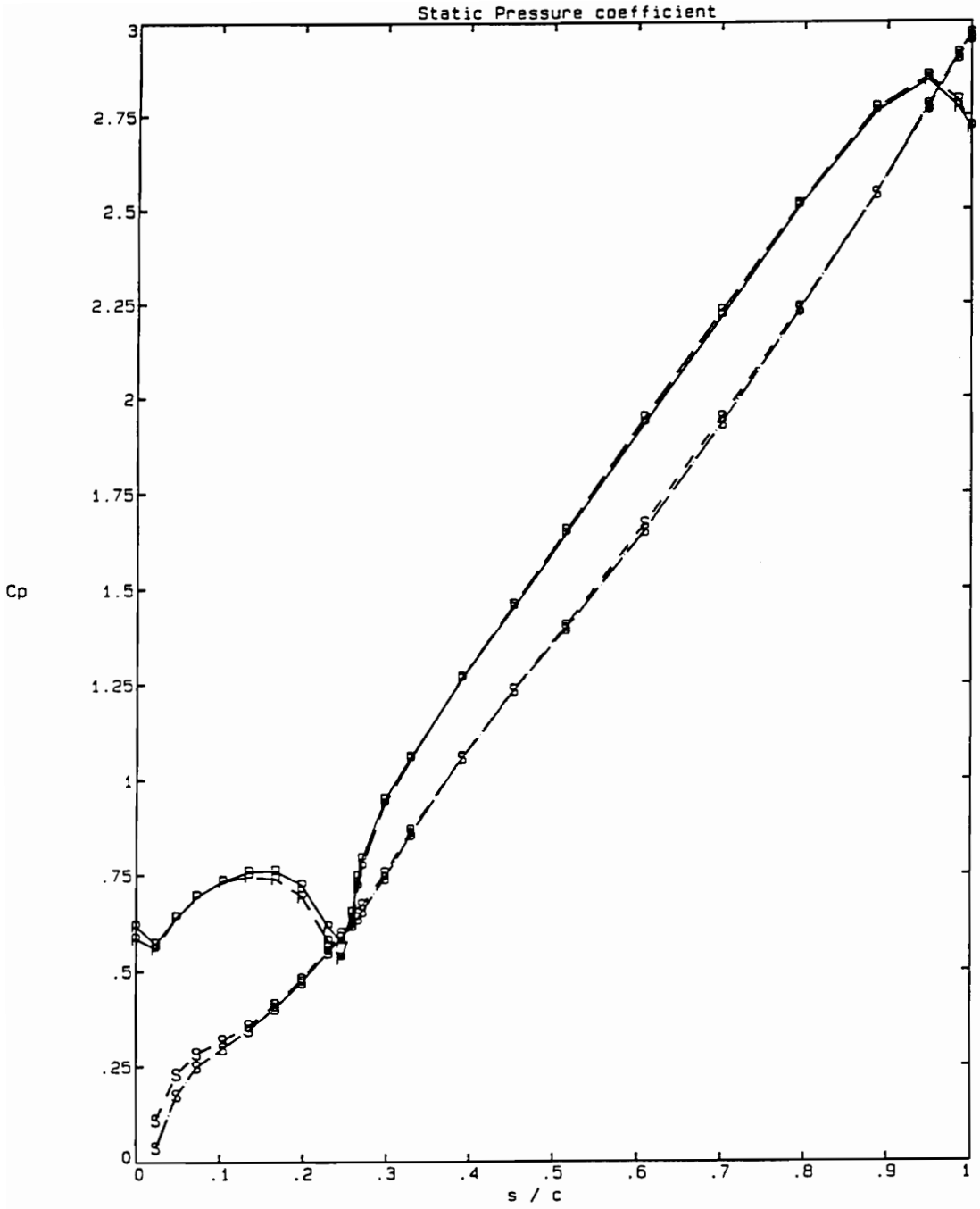


*Figure 48 : Comparison between the Static pressure coefficient (PS & SS) of MB1 and MB2 at k=6 (mid-height) .*

From the impeller main blades LE to the splitters LE, the static pressure on the SS constantly rises. On the impeller main blades PS, the pressure rises then drops severely at the splitters LE .

The difference between the PS and SS static pressure obviously gives the blade loading. The splitter blade region has a fairly uniform loading. The TE unloading can also be noticed. The negative blade-loading region is found to occur at s/c>0.95, whereas the blade unloading started at s/c~0.88 . The 12 percent unloading region corresponds to the uncovered region of the blade .

## 5.7.4: Isentropic Relative Velocities in the Impeller :

### *5.7.4.1: Computation of the isentropic relative velocity W :*

An alternative way of presenting the impeller static pressure distribution is to compute the ideal "blade velocities". These are based on isentropic flow with p*=0, and the local velocity is calculated using the local reduced static pressure $p_r$ .

Since the reduced pressure $p_r$ corresponds to the static pressure in the relative frame in which the total pressure is p* ,

$$p^* = p_r + \tfrac{1}{2}\rho W^2 \qquad (5.9)$$

Therefore :

$$W = \sqrt{\frac{p^* - p_r}{\frac{1}{2}\rho}} \qquad (5.10)$$

At the impeller inlet, the ideal loss-free case has p*=0, and the isentropic relative velocity, W, is given by :

$$W = \sqrt{\frac{-p_r}{\frac{1}{2}\rho}} \qquad (5.11)$$

In the results presented here, W is normalized by $U_{tip\ inducer}$ .

### *5.7.4.2: Relative flow in the impeller :*

Figure 49 shows the relative velocity at the near-wall grid locations (PS and SS) versus the meridional distance for each blade and at the mid-height .

As one expects, the relative velocity is higher on the SS than on the PS, but this is not true all throughout the blades. Since the TE are negatively loaded, the trend is

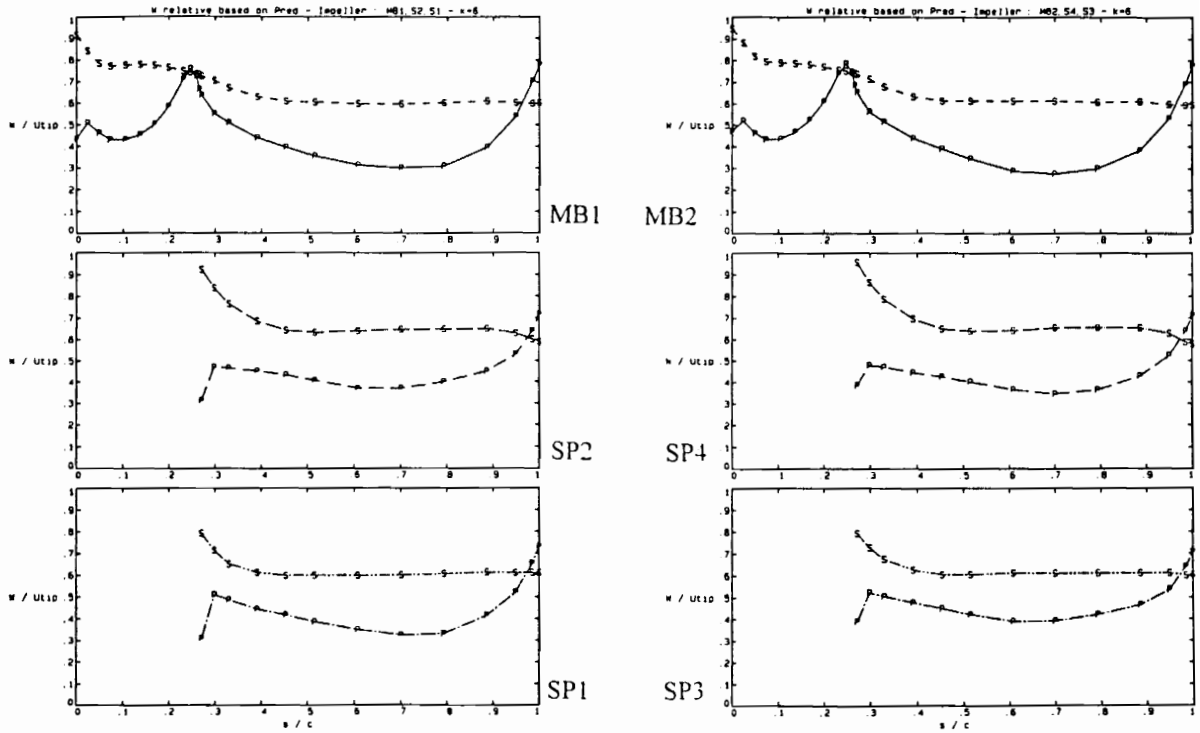


*Figure 49 : Isentropic relative velocity (PS & SS, near-wall) for (SP1,SP2,MB1) and (SP3,SP4,MB2) at k=6 (mid-height) .*

inversed there. For the impeller main blades, the relative velocities on the PS are also higher than on the SS near the location of the splitters LE. Again, this corresponds to the PS and SS inversion. The difference between the SS velocity and the PS velocity (for a given abscissa s/c) gives a measure of how heavily loaded the blades are, and regions like the LE or the blades' mid-meridional distance zones experience higher blade loadings .

Figure 50 shows the previous results in "across the channel"-views, i.e., the SS of blade n with the PS of blade n+1, at mid-height. In this passage view, there is no reverse loading at the splitter LE ; the reverse loading at the TE remains. Relative velocities on the suction sides can be seen to be rather constant in each passage, whereas pressure side velocities experience more changes. Were the impeller radial, the pressure difference between the SS of blade n and the PS of blade n+1 would be proportional to the local mass-flow rate. Even though this impeller is not radial, the relative velocity drop across the channel can be seen as a representation of the flow-rate, and will yield similar conclusions about the flow-split in the impeller passages .

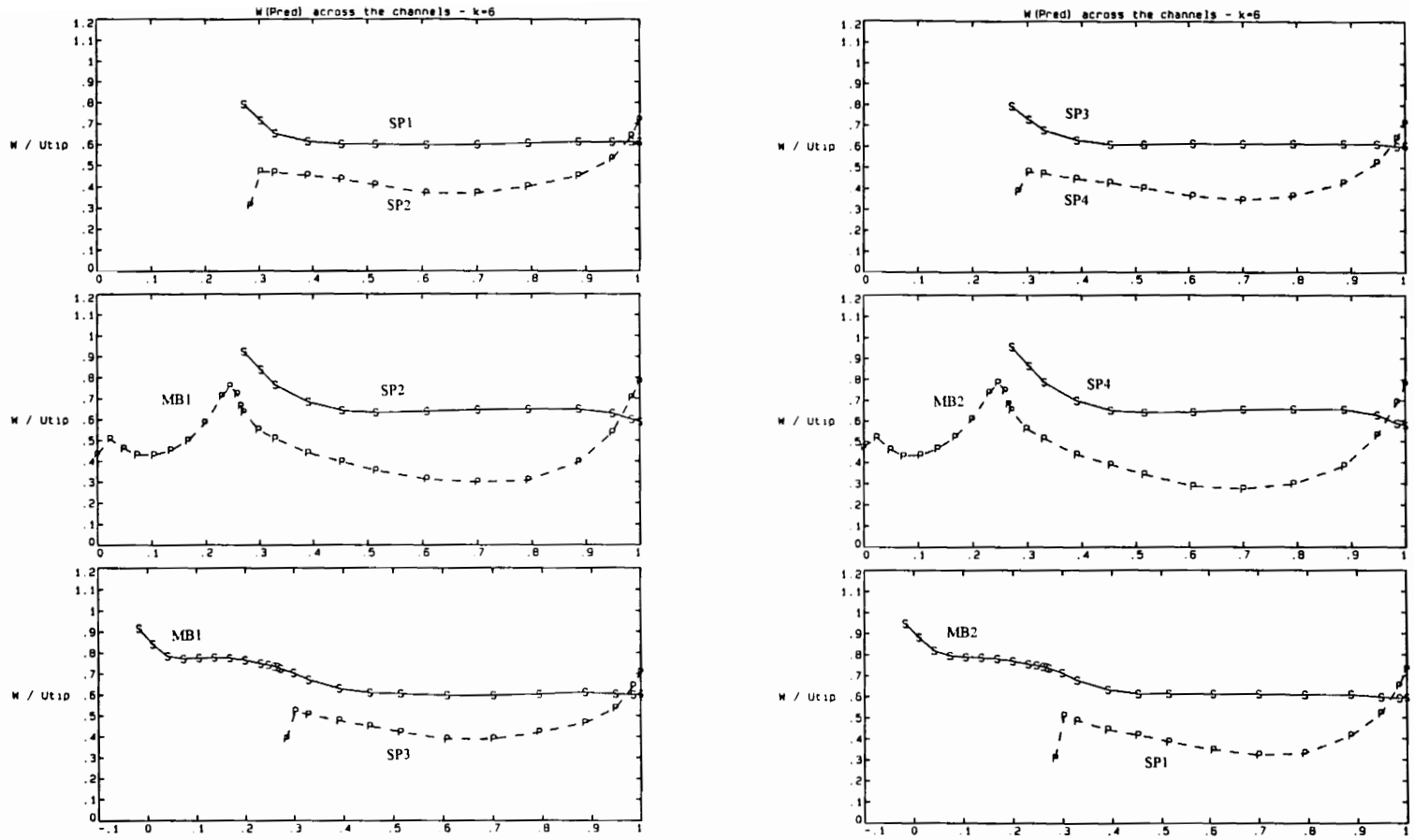


*Figure 50 : Across the channel relative velocity (PS & SS) for all the blades, at mid-height .*

## *5.8 Cavitation in the Tandem Inducer/Impeller.*

### 5.8.1: Cavitation inception :

Cavitation is generally considered to occur, as a first approximation, as soon as the static pressure goes below the local vapor pressure $P_V$ (=1.2 bar for LH2). Cavitation is therefore expected to happen for high velocities and/or high incidence angles .
With upstream total pressure $P_0$, the cavitation inception pressure coefficient can be defined by :

$$P_c = -\sigma_c = \frac{p_v - p_0}{\frac{1}{2}\rho U_{ind.tip}^2} = -0.057 \qquad (5.12)$$

The following analysis emphasizes possible cavitation inception through the machine .

### 5.8.2: Cavitation patterns :

Figure 51 shows locations where cavitation may occur in the unrolled blade-to-blade views at mid-height, inducer tip and within the inducer tip gap. Only static pressure coefficients below 0 are plotted .

* At the hub (not shown), no cavitation has been found .
* At mid-height, the inducer LE minimum static pressure (P ~ -0.04) is on the verge of reaching $P_c$. On the impeller main blades LE, cavitation is more severe since P goes down to -0.05 on MB1 and down to -0.1 on MB2. The impeller LE cavitates because of the locally high incidence that was seen in the blade-to-blade velocities (see section 5.5.2). Even though cavitation is not supposed to occur after the inducer (whose purpose is indeed to increase the static pressure enough so that cavitation is avoided), the inducer unloading at the TE combined with high incidence velocities generate that phenomenon .
* At the inducer tip and in the inducer tip gap, the inducer LE cavitation is present with static pressure coefficients below -0.1. Cavitation looks confined at the LE within a core of low pressure that does not propagate inside the inducer itself. In the tip gap, cavitation is even more intense with P<-0.15 . Values as low as -0.29 were found in the tip gap near the inducer LE .

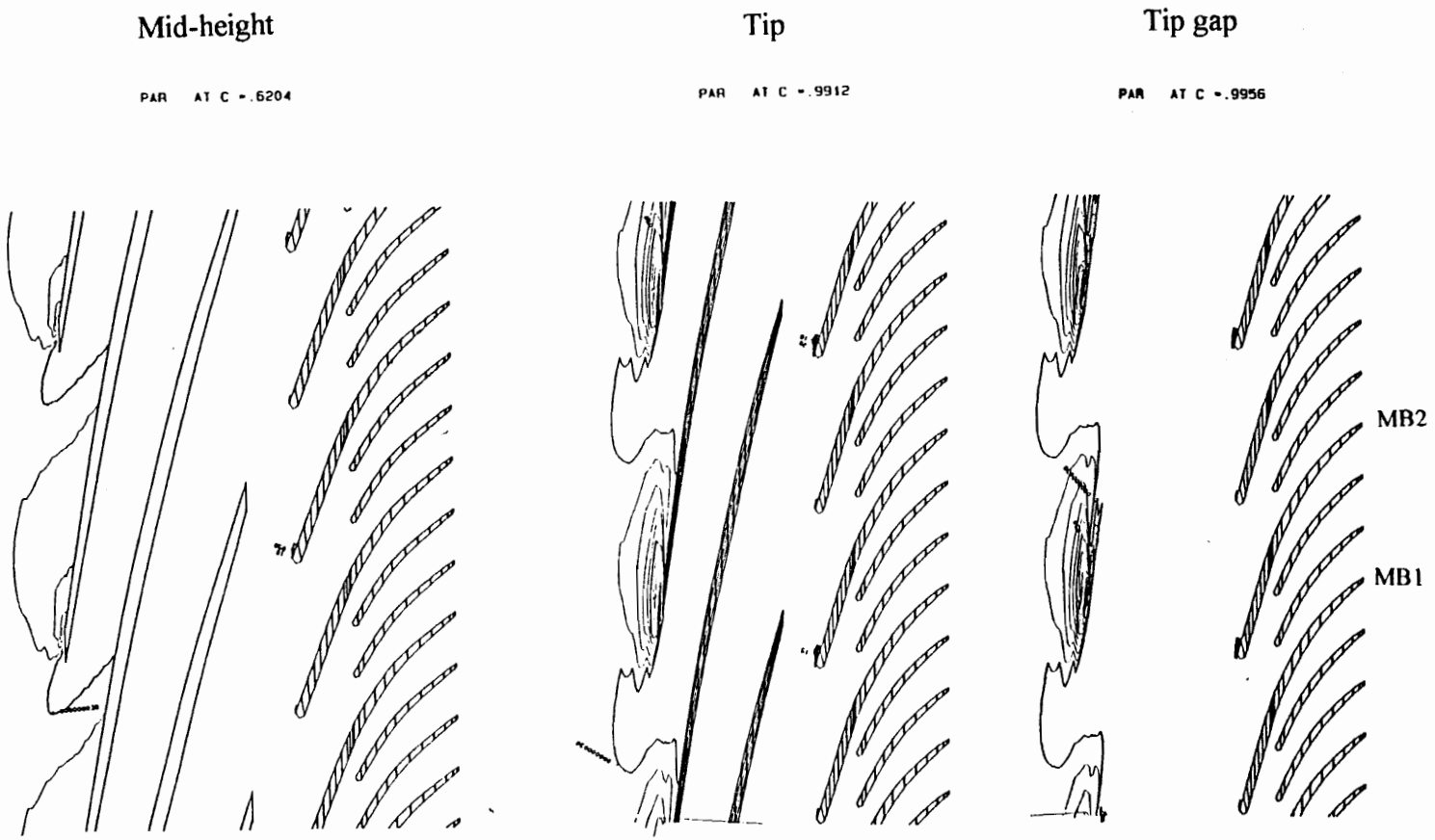


*Figure 51 : Blade-to-blade view showing static pressure coefficients below zero and the possibility of cavitation inception (mid-height, tip, tip gap) .*
*Contour interval 0.01 , 0.05 .*

At the impeller main blades LE for C=0.9912 and C=0.9956, cavitation has increased and P is now below -0.1 on MB1 and below -0.2 on MB2. These low pressure cores on the impeller main blade LE are spatially limited, but are as severe as for the inducer. Though extension through the impeller is very unlikely because of the high pressure rise, LE cavitation should be avoided, and LE redesign might be considered .

### 5.8.3: Inducer LE cavitation :

As was seen on the blade-to-blade views, the inducer LE low pressures (below $P_c$) are confined in a core whose width is about one third of the passage. The following figure (Fig. 52) shows cavitation decay in the inducer passage for the three j-planes near the SS. Plane 27 has a cavitation intensity about a third of that at the SS j=25. In cross-sectional planes (Fig. 53), the cavitation core can be identified on the SS. Just upstream the LE, the core starts about mid-height and widens as it goes toward the tip .

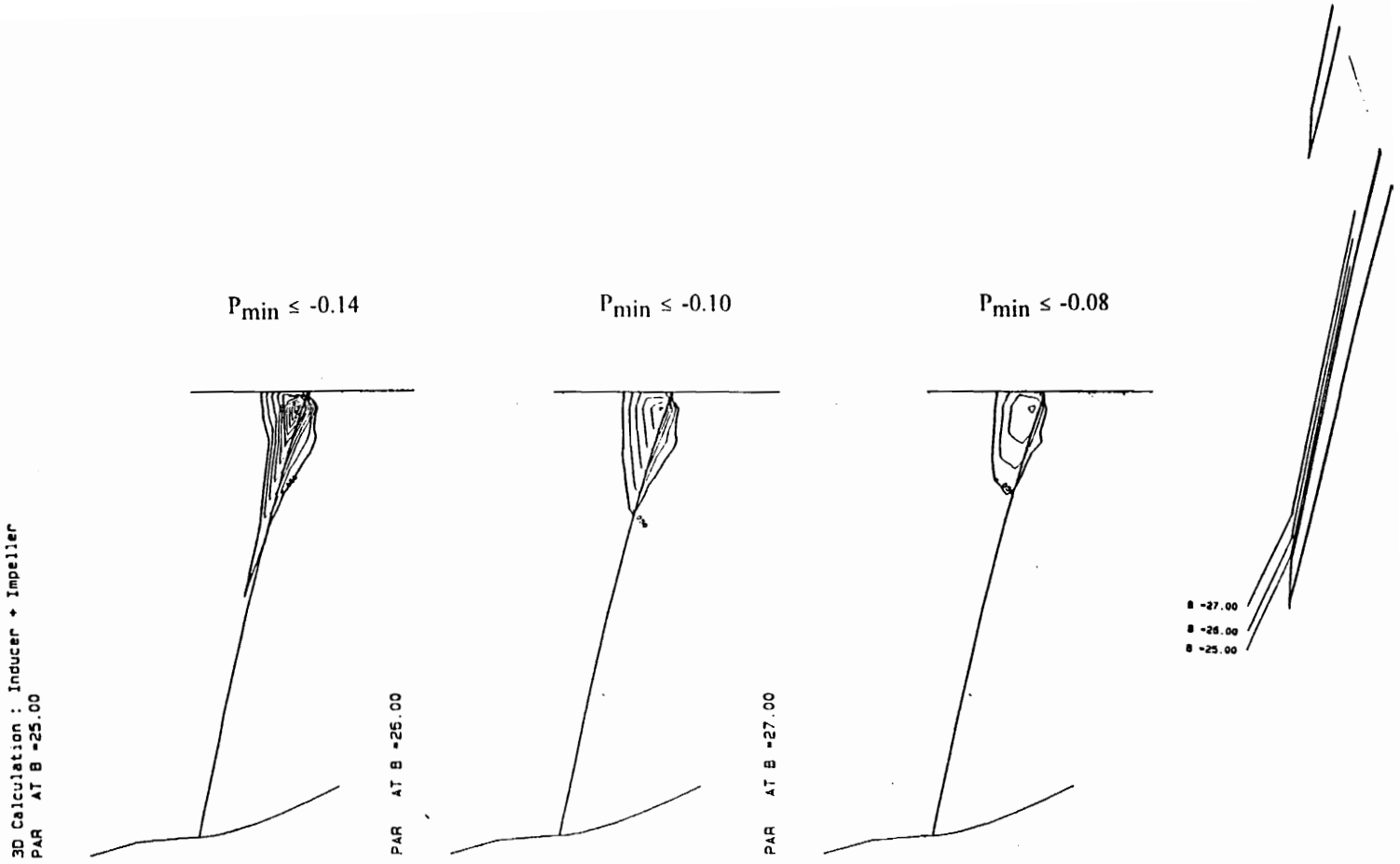


*Figure 52 : Meridional view of the blade-to-blade cavitation core decay .*
*Contours for P < -0.05 . Contour interval 0.01,0.05 .*

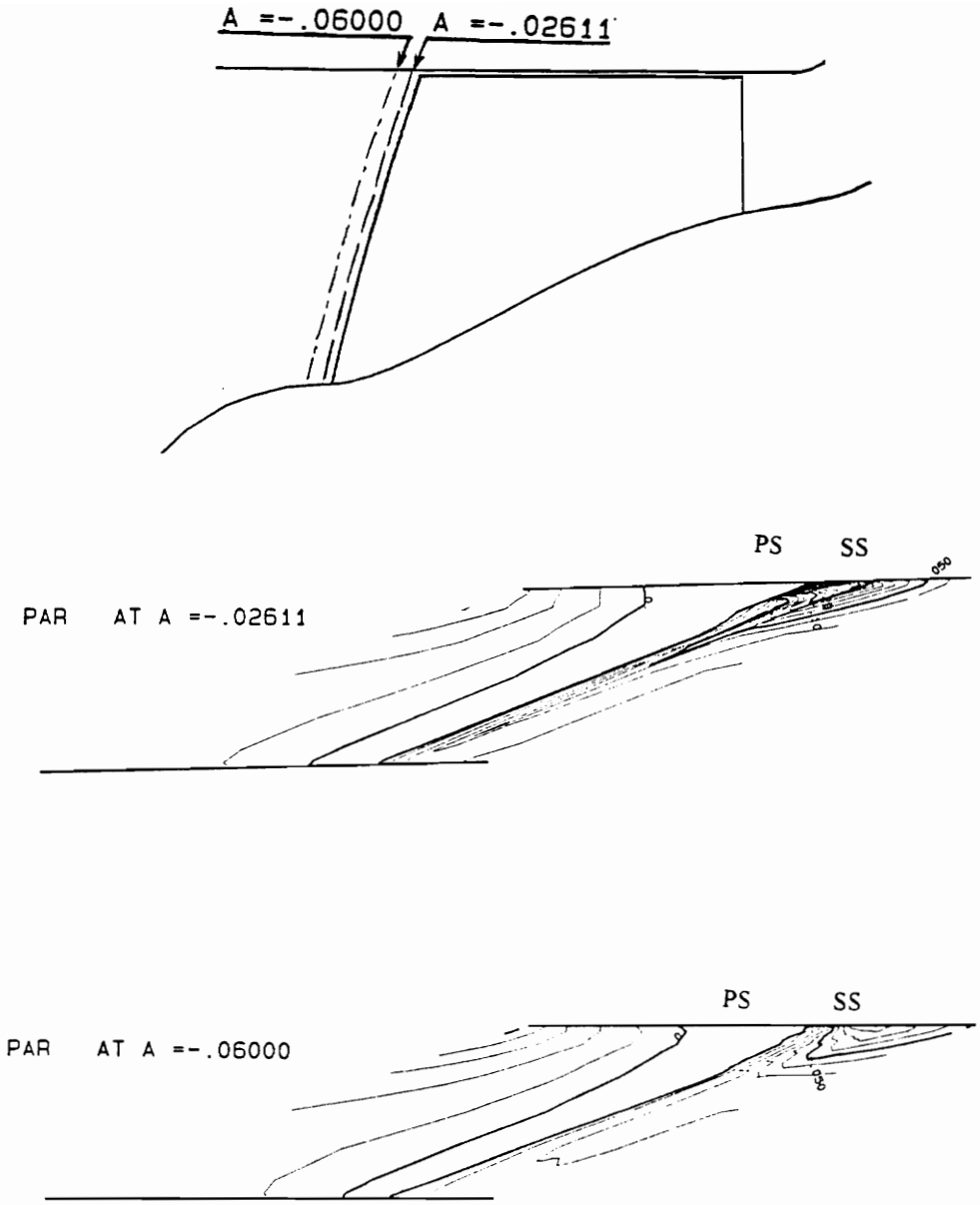


*Figure 53 : Cross-sectional view of the cavitation core .*
*Contour interval for P : 0.01,0.05 .*

# 6.0 COMPARATIVE STUDY OF DOWNSTREAM INFLUENCES ON THE INDUCER.

## *6.1 Introduction .*

A comparative study is here performed to investigate the possible influence of the inducer exit geometry on the inducer performance. Results from additional calculations of the flow in the inducer without the impeller are compared with the results for the tandem inducer/impeller configuration .

Previous inducer flow calculations [17,18] for the VULCAIN turbopump were performed with an axial exit duct downstream of the inducer. The tandem inducer/impeller geometry needs the inducer exit to be bent to allow the flow to go into the impeller. Preliminary design [42] showed non-negligible effects of the inducer exit geometry on the inducer design itself, especially for meridional results .

Therefore, two calculations for the inducer alone have been made : one with an axial exit downstream of the inducer, and one with a radial exit as in the tandem configuration. The grids for these calculations have been described in section 4.5.2. Figure 25 shows the grid for the axial exit and Fig. 23 shows the grid for the radial exit .

For simplicity in the following study :

_ the Inducer in the Tandem inducer/impeller Configuration will be denoted the ITC configuration .

_ the Inducer Alone Configurations (axial or radial exits) will be referred to as configurations IAC. When distinction between the two exits is necessary, the radial case will be denoted IARC (Inducer Alone in the Radial Configuration) and the axial case will be called IAXC (Inducer Alone in the aXial Configuration) .

Interest is focused on possible differences that might occur in the flows for these two geometrical configurations .

## 6.2 *Main results of the comparative study.*

### 6.2.1: Mass-averaged pressures :

Figure 54 shows the mass-averaged pressure coefficients (defined in 5.3.1) plotted against the A parameter through the whole geometry for the three cases .

Both IAC perform the same overall static and total pressure rises, with maximum coefficients just upstream of the inducer exit of $P_s$=0.32, $P_t$=0.405 as found in the tandem configuration. Since overall changes for each pressure ($P_s$ , $P_t$ and P*) are alike in both IAC, it is expected that there will be only very small differences between the inducer flows .

Differences can be noticed after the inducer exit (A=1) :

_ the axial exit inducer has relatively constant static, total and rotary stagnation pressures,

_ whereas the radial exit inducer has increasing static and total pressures under the effect of area changes and work done by the rotating hub and shroud walls. Losses are also produced, and develop considerably in the so-called "splitter" region (A=3 to A=4) where they increase by a factor of 4 .

When the impeller is present, the inducer gives the same overall pressure rise, but the decreases in static and total pressures near the trailing edge (TE) are slightly larger .

### 6.2.2: Efficiencies :

The efficiencies are computed at A=1.338, downstream of the inducer TE, as previously described for the tandem configuration, Section 5.3.3 .

Table 6 details all the terms that were used to compute the efficiency $\eta$ in the different inducer configurations .

***Table 6 : Computation of the efficiency for the different inducers .***

| | $\Psi_{E1}$ | $\Psi_{E2}$ | $\Psi_{loss1}$ | $\Psi_{loss2}$ | $\Psi_{TSs}$ | $\eta$ |
|---|---|---|---|---|---|---|
| **IARC** | 0. | 0.4284 | 0.00076 | 0.0426 | 0.0029 | 0.8963 |
| **IAXC** | 0. | 0.4257 | 0.00026 | 0.0414 | 0.0030 | 0.8970 |
| **ITC** | 0. | 0.4106 | 0.00034 | 0.0396 | 0.0028 | 0.8983 |

t : total pressure
s : static pressure
* : rotary stagnation pressure
r : reduced pressure

0 : inducer LE
1 : inducer TE

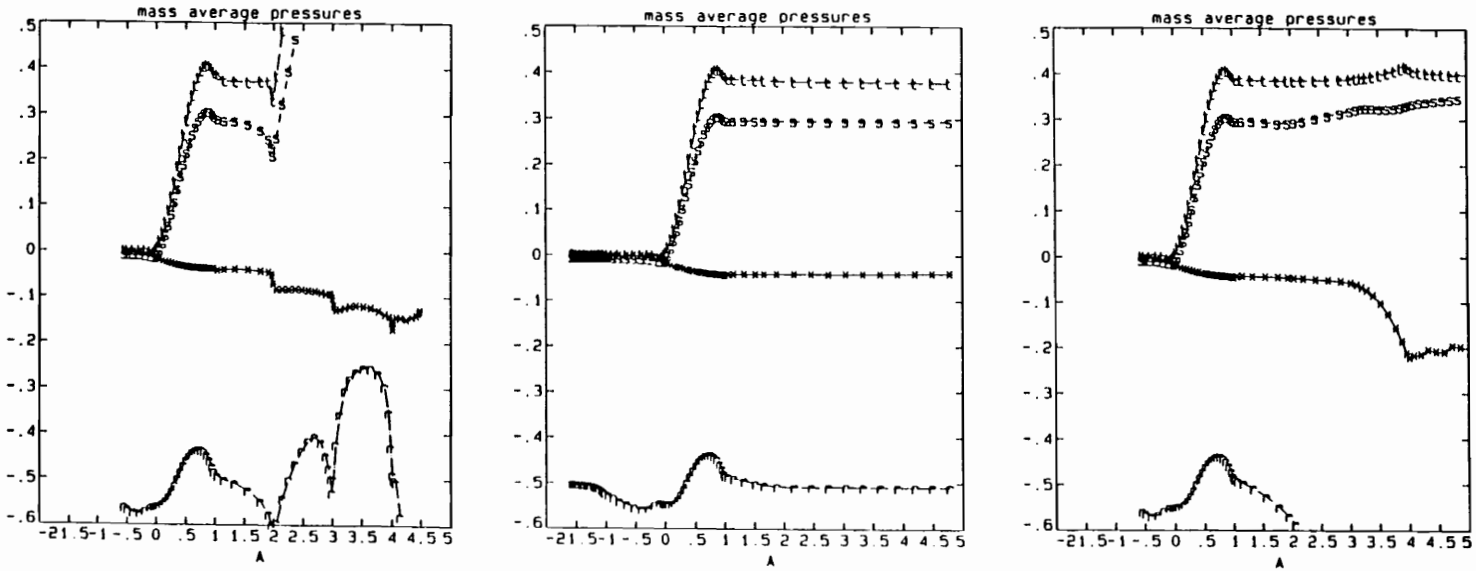


Tandem configuration

Axial exit

Radial exit

*Figure 54 : Mass-averaged pressure coefficients for the three calculations .*

The inducer efficiencies calculated for the three exit flow geometries agree quite closely, $89.7 \pm 0.1$ percent. In the IAC, both the work and losses are unaffected by the changes in downstream boundary conditions. The ITC has slightly lower losses, but also has less work done than the IAC.

For the inducer, the head coefficients, $gH / U_{tip}^2$, are 0.193, 0.192 and 0.186 for the IARC, IAXC and ITC calculations, respectively .

### 6.2.3: Circumferentially averaged flow at the inducer exit :

After the inducer trailing edge, an axial cut of the flow was done at the axial location z=0.091m, between the A=1.225 and the A=1.45 grid lines. This plane is at about a third of the inducer/impeller gap (meridional view) after the TE. Properties at that plane were circumferentially averaged, and are plotted here as hub-to-shroud profiles. Figures 55.a and 55.b show the location of this axial plane in the tandem and the axial case, respectively .

Figure 56 shows the mass-averaged total pressure (56a), static pressure (56b) and rotary stagnation pressure (56c) for the three different inducer configurations .

The total pressure profiles are almost identical for the radial and axial cases. The ITC has less total pressure rise (about 4 percent less), over most of the height, than the IAC. This is consistent with the slightly larger total pressure fall, for the ITC, near the inducer TE, as shown in Fig. 54. This can be thought of as an impeller back-pressure effect. The presence of the impeller modifies the pressure distribution in the inducer/impeller gap and in the uncovered region of the inducer blade, thus affecting the net work by this plane .

Static pressure profiles show similar behavior as for total pressure, with a maximum difference between the ITC and the IAC of about 5 percent . Note that for the axial configuration, where there are no meridional curvature effects, the static pressure varies almost linearly with radius .

In the three configurations, losses remain low for $\bar{r} = \dfrac{r - r_{hub}}{r_{shroud} - r_{hub}} \leq 0.64$, but increase drastically from then till the shroud. Overall, for all three exit geometries, the losses are remarkably similar .

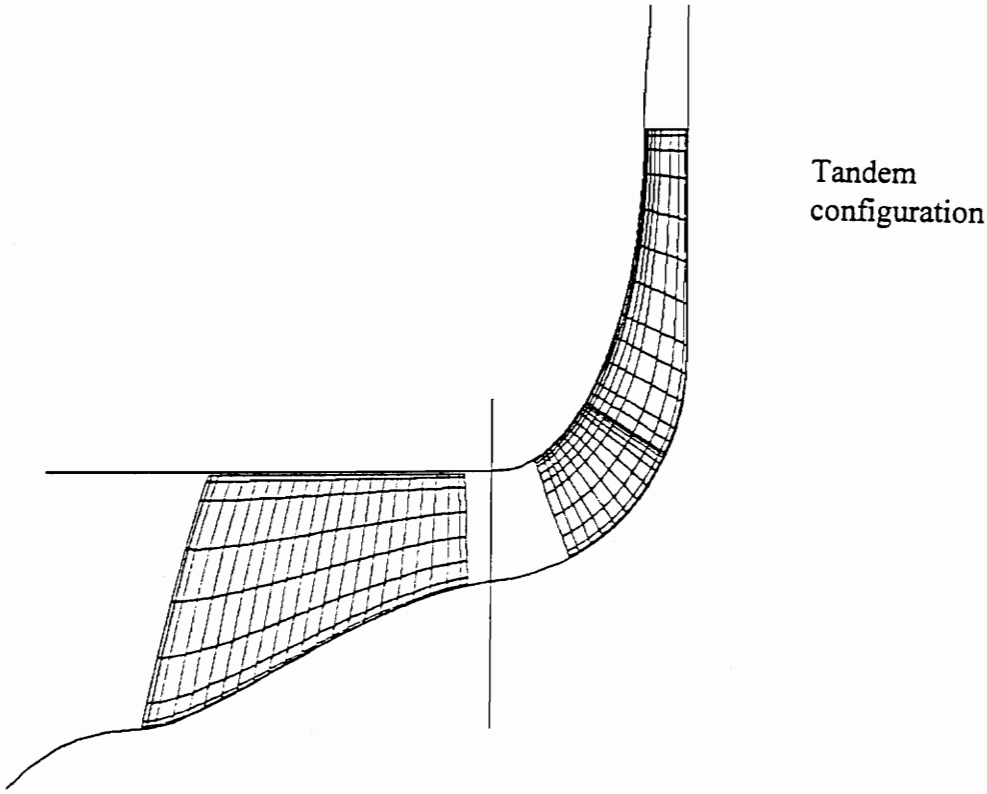


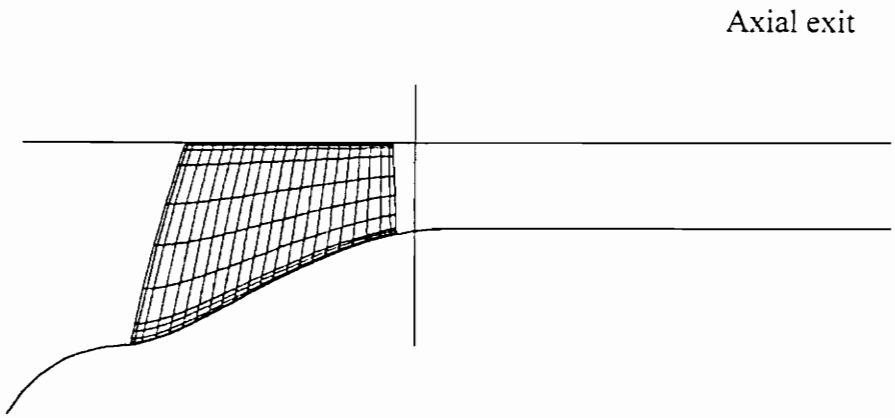


***Figure 55 : Location of the axial cut plane in the tandem (a) and axial (b) cases .***

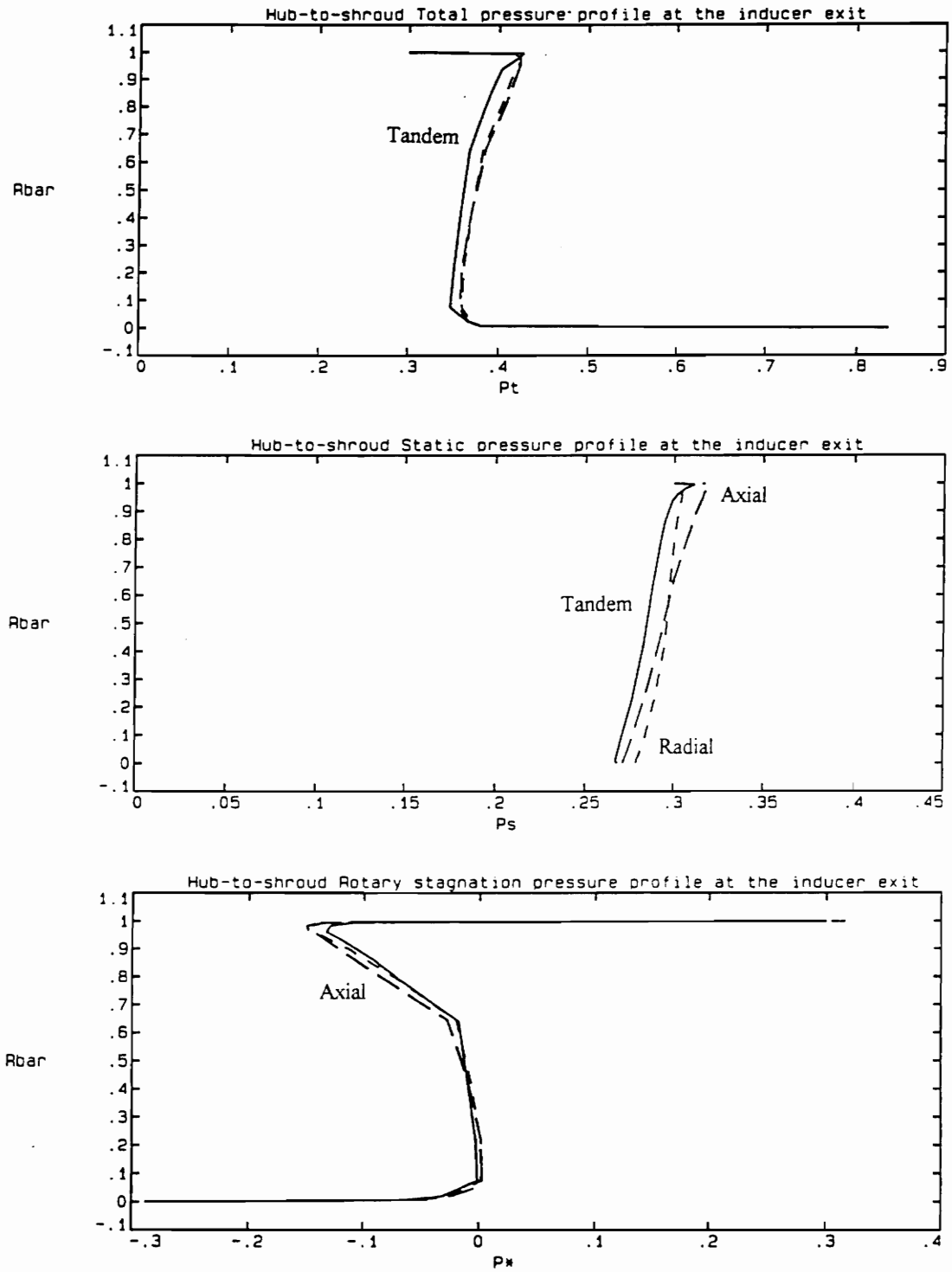


***Figure 56 : Hub-to-shroud circumferentially averaged profiles :***
***(a) total pressure (top) ; (b) static pressure ; (c) rotary stagnation pressure (bottom) .***

Figure 57 shows the axial velocity $W_z$ (a), the relative tangential velocity $W_\theta$ (b), and the relative angle $\beta$ (c) for the three different configurations. $W_z$ is area-averaged ($\overline{W_z}$), $W_\theta$ is mass-averaged ($\overline{\overline{W_\theta}}$), and the relative angle $\beta$ is given by :

$$\tan\beta = \frac{\overline{\overline{W_\theta}}}{\overline{\overline{W_z}}} \qquad (6.1)$$

Much information is to be gained from the analysis of the relative velocity and the relative angle. Figure 57.a first shows that the axial velocity profile at the exit of the ITC is very similar to the axial case. Overall, the IAXC has a more uniform axial velocity profile than the ITC. The IARC is much different from the other two profiles. It has a more distorted axial velocity profile than in the ITC and the IAXC because of curvature effects .

From this velocity analysis, it is clear that the axial exit gives a better correspondence with the flow for the impeller inlet than the radial exit. The impeller therefore acts as if it were canceling the effect of curvature (stronger in the IARC) .

The negative sign for the relative tangential velocity represents the flow in the relative frame ($W_{\theta rel} = V_{\theta abs} - r\,\omega$) .

For $0. \leq \bar{r} \leq 0.64$ , the magnitude of the relative tangential velocity increases linearly with radius in a region where the flow has very low losses (Fig. 56.c). Above $\bar{r} = 0.64$, losses were seen to increase considerably. Consequently, tangential velocities depart from their original linearity, and vary very little with radius till the wall .

Overall, the relative flow angles are between -73 and -78 degrees over most of the height. The variation in the relative angle profiles (Fig. 57c) show great similarities with the axial velocities. Again, relative angles in the ITC are very close to the angles obtained with an axial exit .

As a comparison, the impeller main blade LE angle (pressure side) is also presented on the figure. The blade angle varies from 69 degrees at the hub to 74 degrees at the shroud. Comparing with the flow angles, it gives an idea of the evolution of the incidence angle at the impeller LE (neglecting changes in flow angle due to meridional geometry changes in the gap). It can be seen that the IARC predicts more incidence below $\bar{r} = 0.64$ than the other two cases, and vice-versa above that radius. In the ITC case, incidence at the hub is about 2.5 degrees, but rapidly increases to 5 degrees at $\bar{r} \approx 0.075$. From there to the shroud, incidence decreases and reaches about 3 degrees near the shroud .

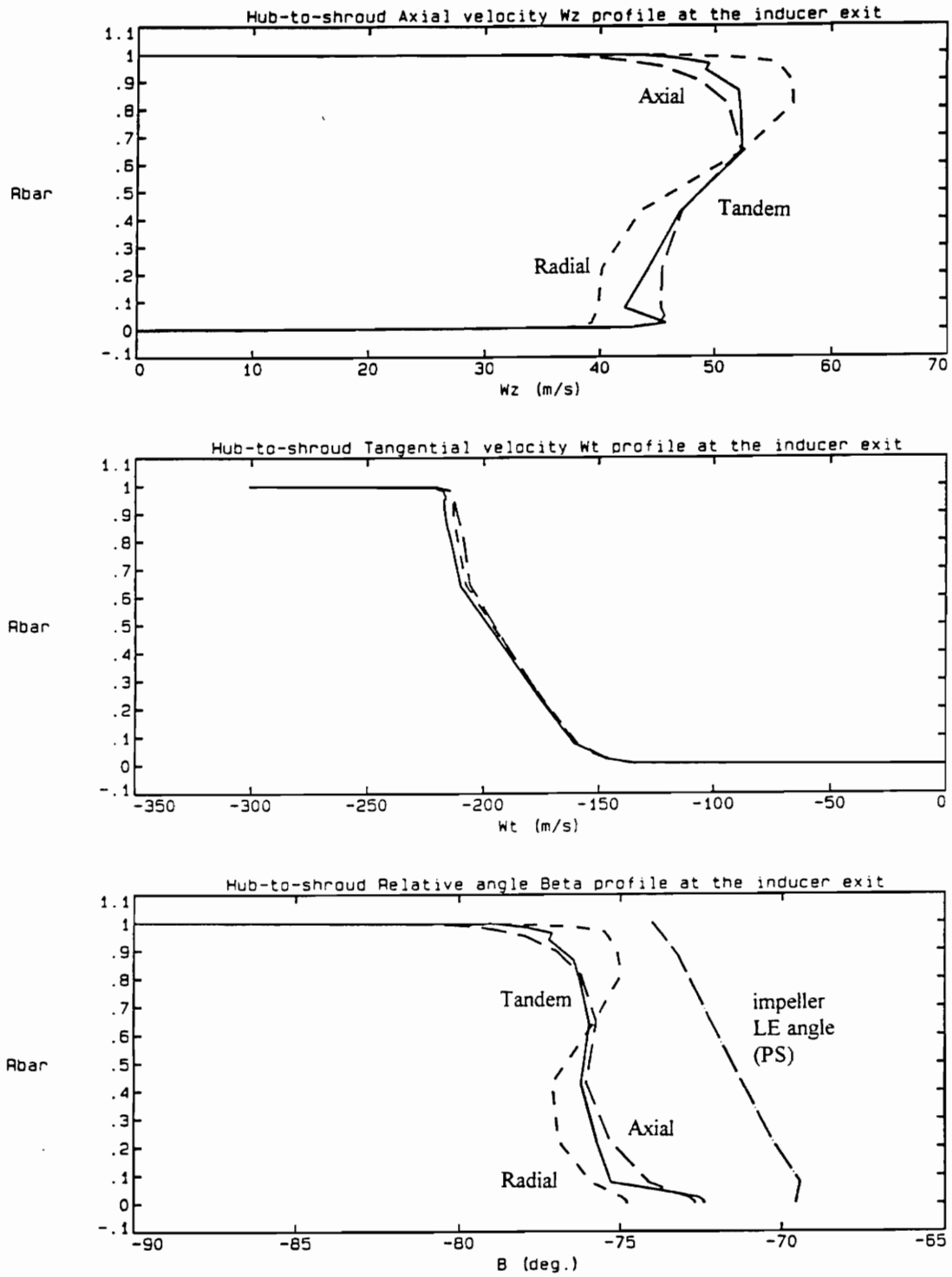


***Figure 57 : Hub-to-shroud circumferentially averaged profiles :***
***(a) axial velocity (top) ; (b) relative tangential velocity ; (c) relative flow angle (bottom)***

### 6.2.4: Inducer/impeller matching :

The previous circumferentially averaged results showed the influence of the impeller on the inducer characteristics. It also showed the main interest of the axial exit in terms of getting inlet conditions for an impeller alone calculation. Several problems need to be answered before knowing if inducer and impeller calculations can be uncoupled. In particular :

_ how strongly does the impeller influence the inducer flow (see section 6.3) ?

_ is there a minimum distance between the inducer and the impeller beyond which this influence is negligible ?

_ how important is this distance in terms of the inter-blade gap flow ?

Answers to these last two questions can be found in Jakobsen [3] and are detailed/reproduced below :

_ "the inducer discharge dimensions must match those of the impeller eye".

This may lead to head rise limitation problems because "an increase in the impeller eye diameter will decrease the impeller head but an increase of the inducer discharge diameter will increase the inducer head, and vice-versa". A solution to this problem can be found in increasing the axial clearance between the inducer and the impeller. A smooth meridional contour for the clearance is advised by Jakobsen [3] .

_ the axial clearance is required for a good hydrodynamical inducer/impeller matching. It is essential for good suction performance of the impeller main blades. The general expression for the minimum axial clearance is given by :

$$\Delta z = \frac{2\pi r}{N} \sin\beta_{TE} \qquad (6.2)$$

where : * r is the local radius,

* N is the number of blades in the inducer (here, N=4),

* $\beta_{TE}$ is the blade TE angle defined by : $\tan\beta = \frac{dz}{r.d\theta}$ (6.3)

(evaluated at the TE) .

In the particular case of a flat-plate inducer, this expression reduces to :

$$\Delta z = \frac{L_{ax}}{\sigma} \qquad (6.4)$$

where : * $L_{ax}$ is the axial length of the blade

* $\sigma$ is the solidity at the inducer TE .

Figure 58 shows the application of Jakobsen's formula to the present geometry. The x-axis represents the dimensionless distance for several approaches that were made in order to see different effects (see below). The y-axis is the dimensionless radius :

$$\bar{r} = \frac{r - r_{hub}}{r_{shroud} - r_{hub}} \quad . \tag{6.5}$$

Different analyses for the minimum distance between the components are proposed here :

_ solution 1 :

It shows the actual axial distance between the inducer and the impeller (dist=$Z(i_{imp.LE},k)$ - $Z(i_{ind.TE},k)$) normalized with the Jakobsen's distance DZJ taken from Eq. (6.2) .

_ solution 2 :

It shows the effect of curvature on the distance between both elements. DZJ is still taken from Eq. (6.2). The distance is calculated as the curvilinear abscissa, for a given k-layer :

$$\text{dist} = \int_{ind.TE}^{imp.LE} \sqrt{dr^2 + dz^2} \tag{6.6}$$

This distance has been computed on the original grid (see section 4.2.3) before the k-smoothing .

_ solution 3 :

It shows the difference between a flat-plate inducer and the present design. "dist" is taken as in solution (1), and DZJ is taken from Eq. (6.4), for constant radius layers inside the inducer .

In each of the three cases, the distance between the inducer and the impeller decreases as the radius increases from hub to shroud. These variations are linear .

* Case (1) is the most demanding one. At the hub, the axial distance is about 72.5 percent the Jakobsen's required axial distance. It drops down to only 40 percent, near the shroud. As a consequence, impeller interactions on the inducer are expected to be relatively weak at the hub, but will increase and reach their maximum at the shroud .

* Using meridional distances, case (2), has a little relieving effect, but it remains limited since the present inducer/impeller gap is close to being axial (the impeller starts early in the bend) .

* Case (3) shows that the present inducer is rather far from being a flat plate inducer. Were it the case, about 88 percent of the Jakobsen's distance would be reached here at the hub, and about 57 percent near the shroud .

Figure 59.a shows a practical example (the LE-5 Liquid Oxygen Turbopump, [25]) of inducer/impeller gap in which a minimum axial distance between the two components seems to be applied. The axial distance seems to be of the order of the inducer tip axial chord. Besides increasing the axial distance, the adopted solution there was to start the impeller LE after the bend and in the radial region. Together with decreasing flow control (incidence) at the impeller LE, this solution requires a particular technology for the shroud at the inlet. No blade strengthens the impeller inlet against centrifugal stresses, i.e., no material link exists between the hub and shroud surfaces. Rotordynamics (vibration, seals, wear) might be more difficult to handle .

Conversely to the tandem inducer/impeller case, the inducer / guide vane / impeller configuration (Fig. 59.b) has a minimal axial distance between the components. The inducer/guide vane gap is only about a third of the inducer tip axial chord. However, the guide vane/impeller gap is larger (about half the guide vane chord), possibly to allow the flow to become more uniform before the impeller inlet .

Figure 60 shows a possible modified meridional design for the inducer/impeller gap. Criteria (1) is used to impose the minimum distance at the shroud. The hub distance is automatically satisfied. The inter-blade gap is an axial inducer exit, which has been shown (see 6.2.3) to give good results for the impeller inlet flow .

Even if the hydrodynamical gap improves the inducer/impeller matching, it has to be seen as a compromise with rotor-dynamic problems. Increasing the gap also increases the shaft length, and possibly the inducer overhang, depending on where the bearing is to be located. Finally, it also increases the overall pump size .

As a conclusion, it is clear that the minimum axial distance suggested by Jakobsen is not satisfied in the MCA geometry. The question of whether there is a hydrodynamic mismatch between the inducer exit flow and the impeller inlet is considered in the next two sections, 6.3 and 6.4 .

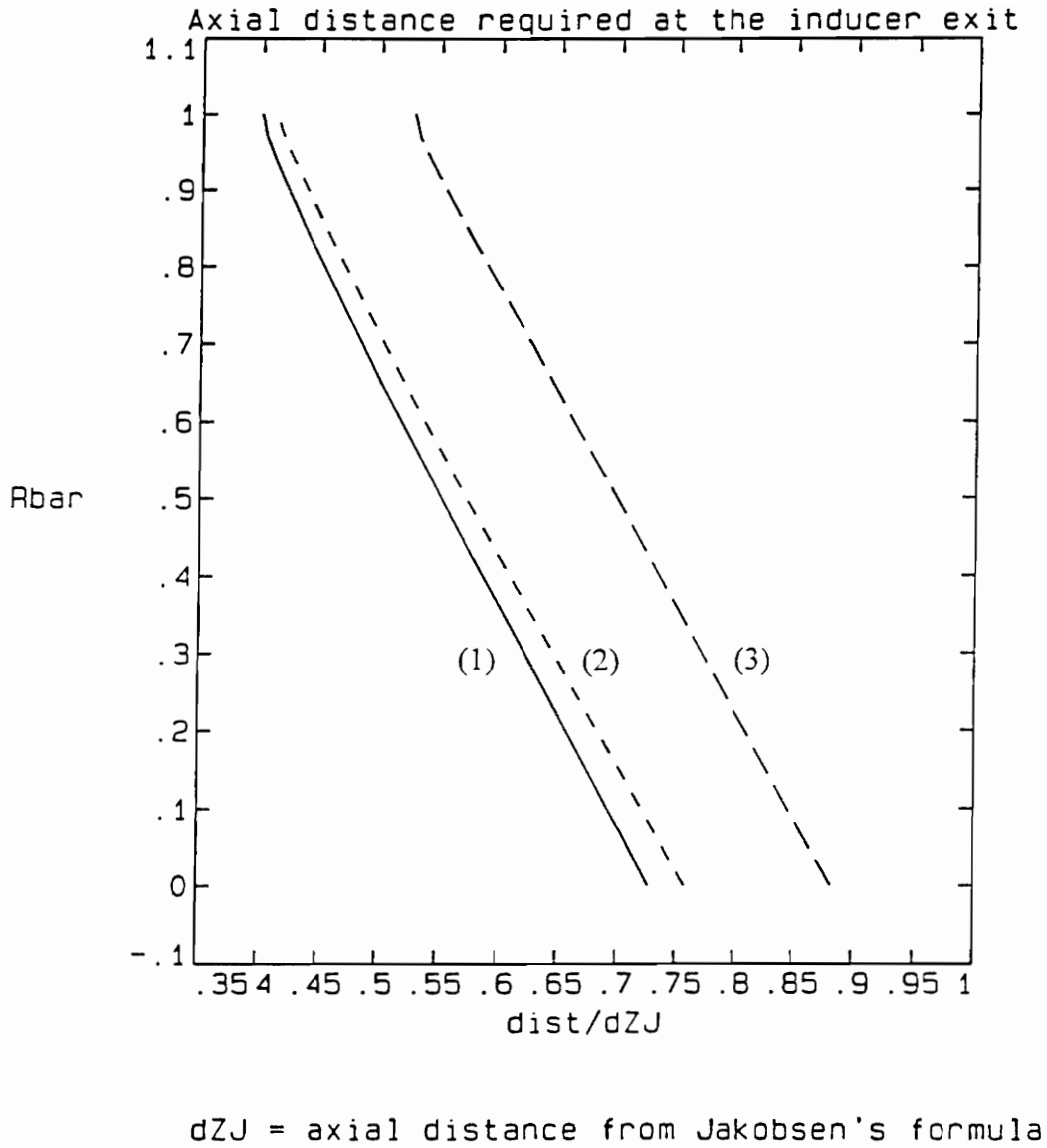


*Figure 58 : Comparison of the actual inducer/impeller gap with Jakobsen's suggestion*

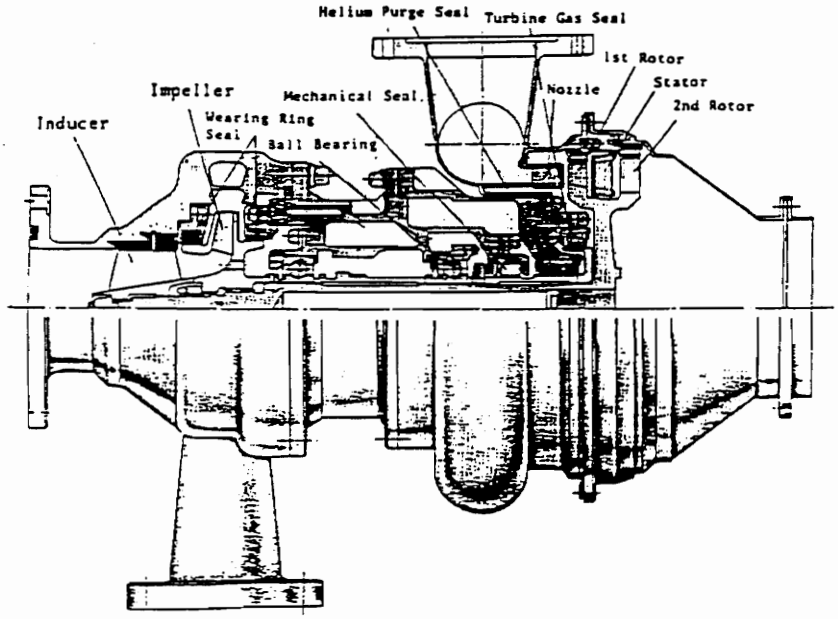


*Figure 59.a : Inducer/impeller gap in the LE-5 Liquid Oxygen Turbopump [25].*

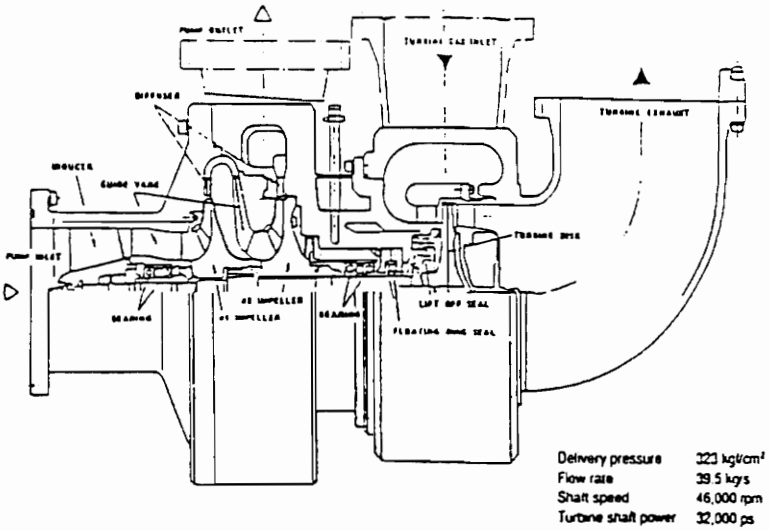


*Figure 59.b : Observed gaps in the tandem inducer/guide vane/impeller combination of the LE-7 Fuel Turbopump [25].*

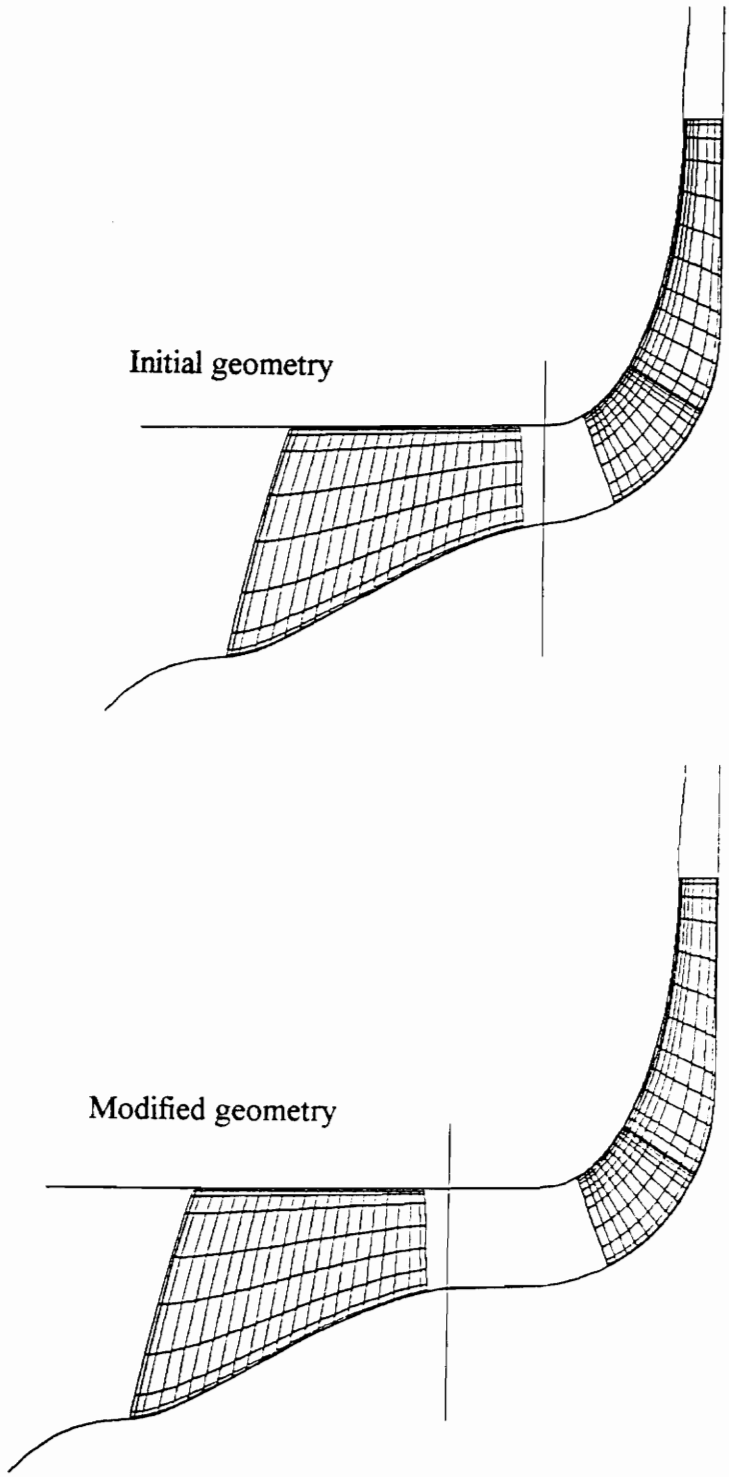


*Figure 60 : Possible modification for the inducer/impeller gap .*

## *6.3 Introduction to the Impeller and Geometry Influences on the Inducer Flow .*

For each of the three calculations, a common control volume (CV) can be defined to help determine the possible origins of flow differences in the inducer. This CV is characterized by :

_ an entrance plane (left face) : grid inlet plane,

_ a top face : the shroud,

_ a bottom face : the inlet pipe center line and the inducer hub,

_ and an exit face : the $A \cong 1.225$ plane (used for the axial cut) .

Because of identical boundary conditions, the three flows have the same velocity and pressure field at the inlet face of the CV, and there is no inlet recirculation at that plane. Thus, for identical inducer geometry, flow and boundary conditions, similar upstream conditions can not but produce a similar flow field in the inducer. As a consequence, differences in the inducer flow occur through the exit face. The only influence that the impeller and/or the geometry can have on the inducer is through this downstream surface of the CV .

The governing equations allow the impeller and the geometry to influence the inducer in three different ways across this surface :

1) Convection :

Were the inducer exit flow stagnating or recirculating, backflows would bring information from the impeller to the inducer through the surface .

At design flow rate, none of the IAC configurations give inducer exit stagnating flow. In the ITC, since curvature will not produce recirculation at design flow, the only possible backflow can result from the impeller presence. Figure 61 shows the absence of any backflow in the A=1 to A~1.6 region. Impeller LE backflows are relatively confined . From this analysis, it is clear that no backflow occurs in the exit face of the CV. Convection is not an inducer influencing factor .

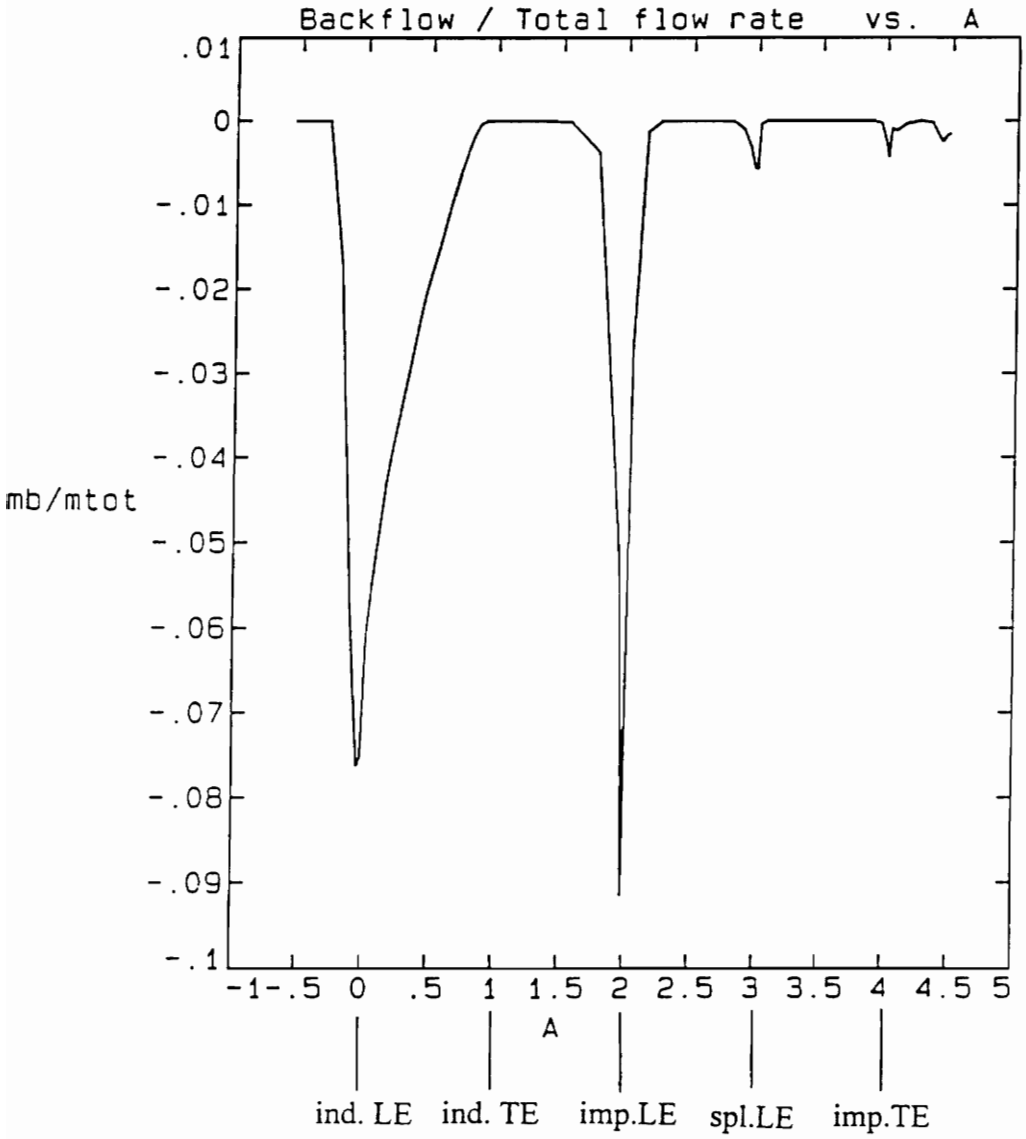


*Figure 61 : Backflow development in the tandem inducer/impeller .*

2) Laminar and turbulent diffusion of momentum across the surface :

Velocity gradients in the axial direction govern the diffusion of momentum across the CV exit plane. These effects are probably small .

3) Static pressure :

Both the presence of the impeller and the meridional curvature seriously modify the static and reduced pressures in the CV exit surface. As a consequence, possible differences in the inducer flow field could result from a pressure driven mechanism acting through the surface .

Figure 62 shows the static pressure in the CV exit plane (A=1.225) for both the IAC and the ITC .

The IAC cases show four high static pressure regions on the shroud and four lower static pressure regions at the hub, one for each of the four inducer blades. The locations of the inducer trailing edges can be easily guessed by the rapid tangential static pressure gradient that occurs between the red/yellow contours and the green ones across the reversely loaded TE (i.e., higher pressures on the SS, lower ones on the PS) .

The ITC configuration shows eight high pressure regions on the shroud corresponding to the eight impeller main blades. The circumferential high/low pressure pattern caused by the impeller main blades adds to the reverse loading pattern at the inducer TE : it increases the high pressure at the inducer TE suction side, and decreases the low pressure at the inducer TE pressure side.

In the IARC, static pressure contours are similar to those in the IAXC. However, high pressure regions are not as strong as the corresponding high pressure regions in the IAXC. Low pressures are almost alike in both cases. Globally, the pressure distributions in the IAC are consistent with the circumferentially averaged results shown on Fig. 56.b.

From this analysis, it is obvious that the impeller influences the pressure distribution in the CV exit plane. Further study is now needed to determine how far upstream in the inducer the impeller interaction can be felt .

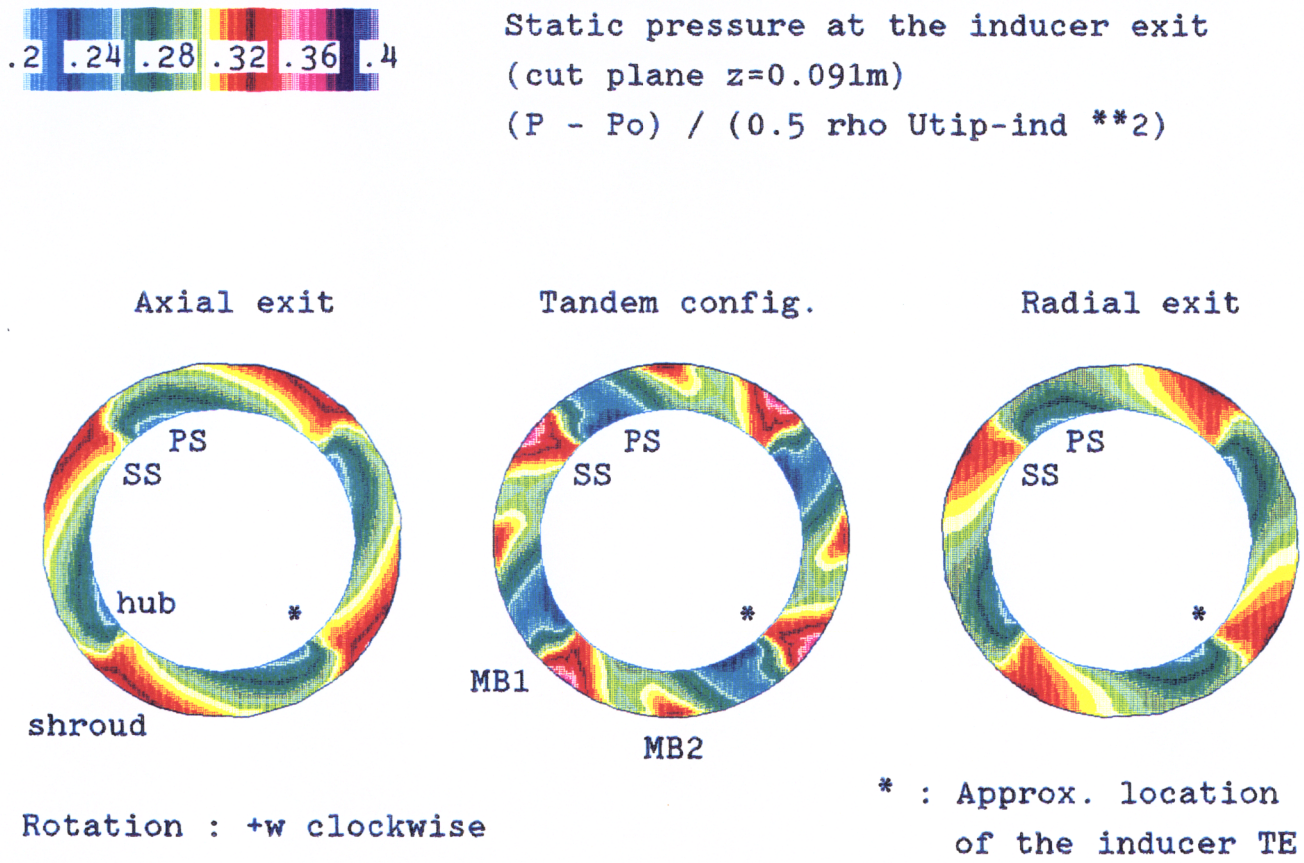


*Figure 62 : Static pressure in the gap (A=1.225) for the three configurations .*

## *6.4 Blade-to-blade and Inter-blade Gap Results .*

### 6.4.1: Definition of accurate constant fraction-of-height surfaces :

As it was pointed out in 4.5.1.2, the C parameter represents different fractions of height throughout the whole geometry, depending on the i-plane considered. This problem mainly comes from the grid smoothing in the k-direction (see 4.4.2.3), especially after the inducer TE, in the bend and in the impeller .

In order to make grid-independent comparisons between the three configurations, properties to be studied were interpolated on accurate constant fraction of height surfaces. Three unrolled blade-to-blade surfaces will be considered :

_ 2.5 percent fraction of height : near hub surface,
_ 50.0 percent fraction of height : mid-height surface,
_ 97.5 percent fraction of height : through the inducer tip and near the shroud surface .

At the tip section, the constant fraction of height surface cuts the inducer blade with a variable radius (from LE to TE). Thus, the first 80 percent chord distance from the LE will be seen to cut the full blade whereas the last 20 percent are right at the tip section. This explains the change in the blade point type and the sudden appearance of the grid near the TE .

### 6.4.2: Reduced pressure :

The relation between reduced pressure $P_r$ and the rotary stagnation pressure is similar, in the relative frame, to the relation between the static and the total pressures in the absolute frame. Thus, looking at reduced pressure variations provides information about the relative velocity W .

The present section aims at showing the ever growing (from hub to shroud) influence of the impeller on the inducer in the uncovered region particularly .

<u>Comparison between the IARC and the ITC :</u>

Figures 63 to 65 show - in color - the reduced pressure near the hub, at mid-height and near the tip & shroud for the comparison between the IARC and the ITC .

Hub :

As the flow approaches the inducer LE, the reduced pressure decreases and the flow accelerates. At the LE itself, $P_r$ slightly increases, thus underlining the slowing down effect at the LE (similar to a stagnation point on a blunt body). As the flow goes through the inducer, a $P_r$ gradient develops normal to the streamwise direction. Low pressures are on the SS and high $P_r$ are on the PS, which is consistent with the already noticed high relative velocities on the SS and lower ones on the PS of the blade .

At the hub, the fluid flows along almost constant $P_r$ streamlines (sensibly parallel to the blade surfaces), thus showing that hub velocities remain fairly constant .

Until the TE, the reduced pressure development inside the inducer is identical in both the IARC and the ITC. A trailing edge to trailing edge line shows very similar circumferential variation of the reduced pressure. The uncovered region of the inducer blade is only very slightly affected by the impeller presence. This is consistent with previous statements according to which the inducer/impeller gap at the hub is close to being large enough to allow good suction performance. In the uncovered region, the $P_r$ gradient in the streamwise direction becomes negative, and the flow is accelerated .

In the IARC, reduced pressure keeps decreasing after the TE as the flow accelerates in the bend, and $P_r$ becomes circumferentially uniform. In the ITC, the presence of the impeller modifies the $P_r$ distribution after the TE. Instead of becoming circumferential uniform, $P_r$ changes to a high/low pattern around the leading edge of each impeller blade due to the incidence on the blades and the high blade loading. The low pressure on the inducer TE pressure side connects to the low pressure on impeller MB2 suction side, thus forming a throat through which the flow is accelerated. Along the inducer PS in the uncovered region, $P_r$ decreases till the TE and the flow accelerates. At the TE, velocities leaving the PS are slightly higher in the ITC case. Correspondingly, there is a ridge of higher reduced pressure connecting the inducer SS with MB1 pressure side .

$P_r$ distributions on the impeller PS are identical for both MB1 and MB2. On the SS, the inducer PS TE / impeller MB2 SS throat causes the reduced pressure distribution to be different on the suction side of MB2 from what it is on the SS of MB1. The reduced pressure decreases much more and therefore accelerates the flow more around the LE .

Mid-height :

Flow upstream the inducer LE is accelerating under the same reduced pressure gradient in both configurations. Inside the inducer passage, on the SS, $P_r$ remains almost

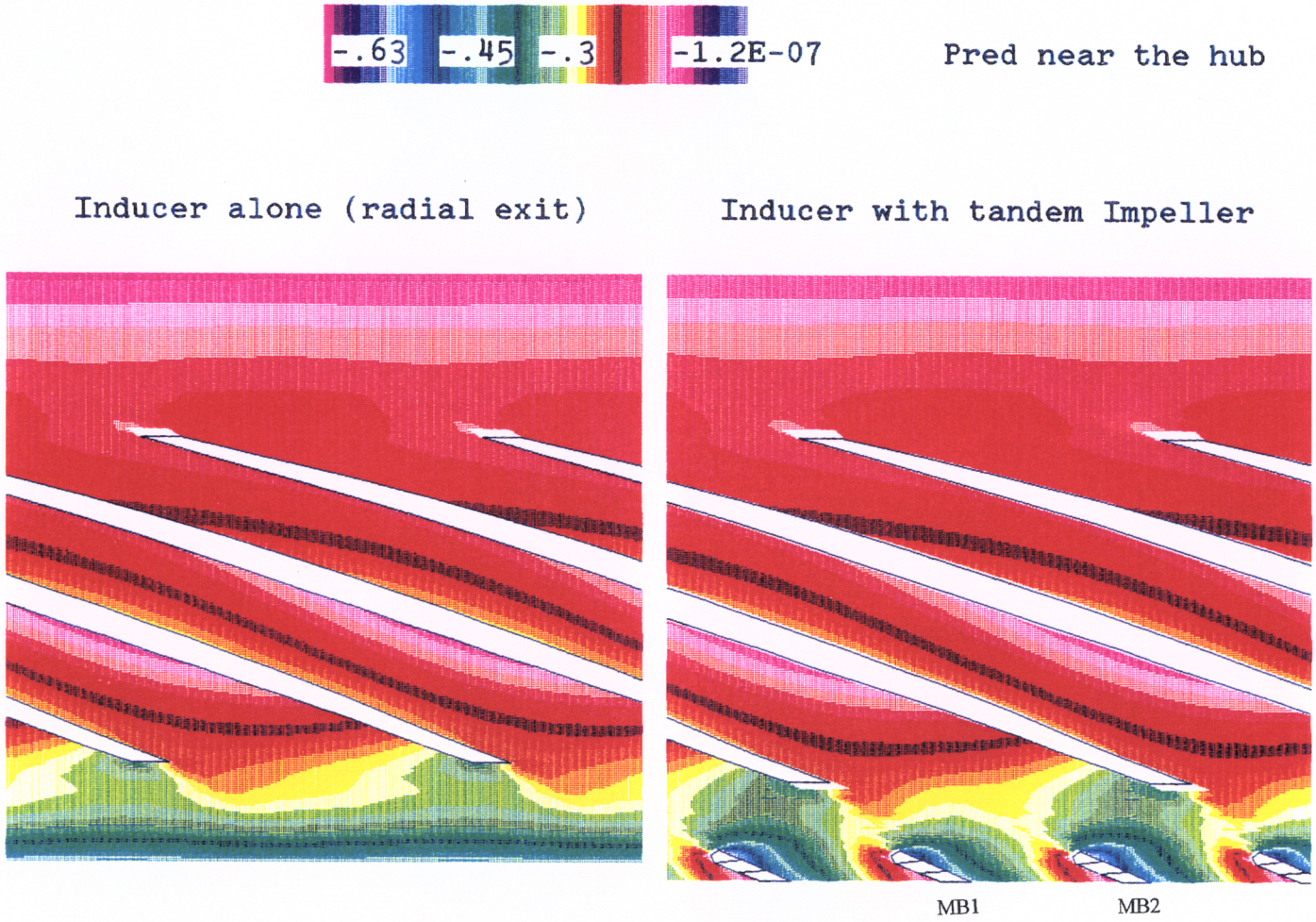


*Figure 63 : Blade-to-blade view of the reduced pressure near the hub, for the IARC and the ITC .*

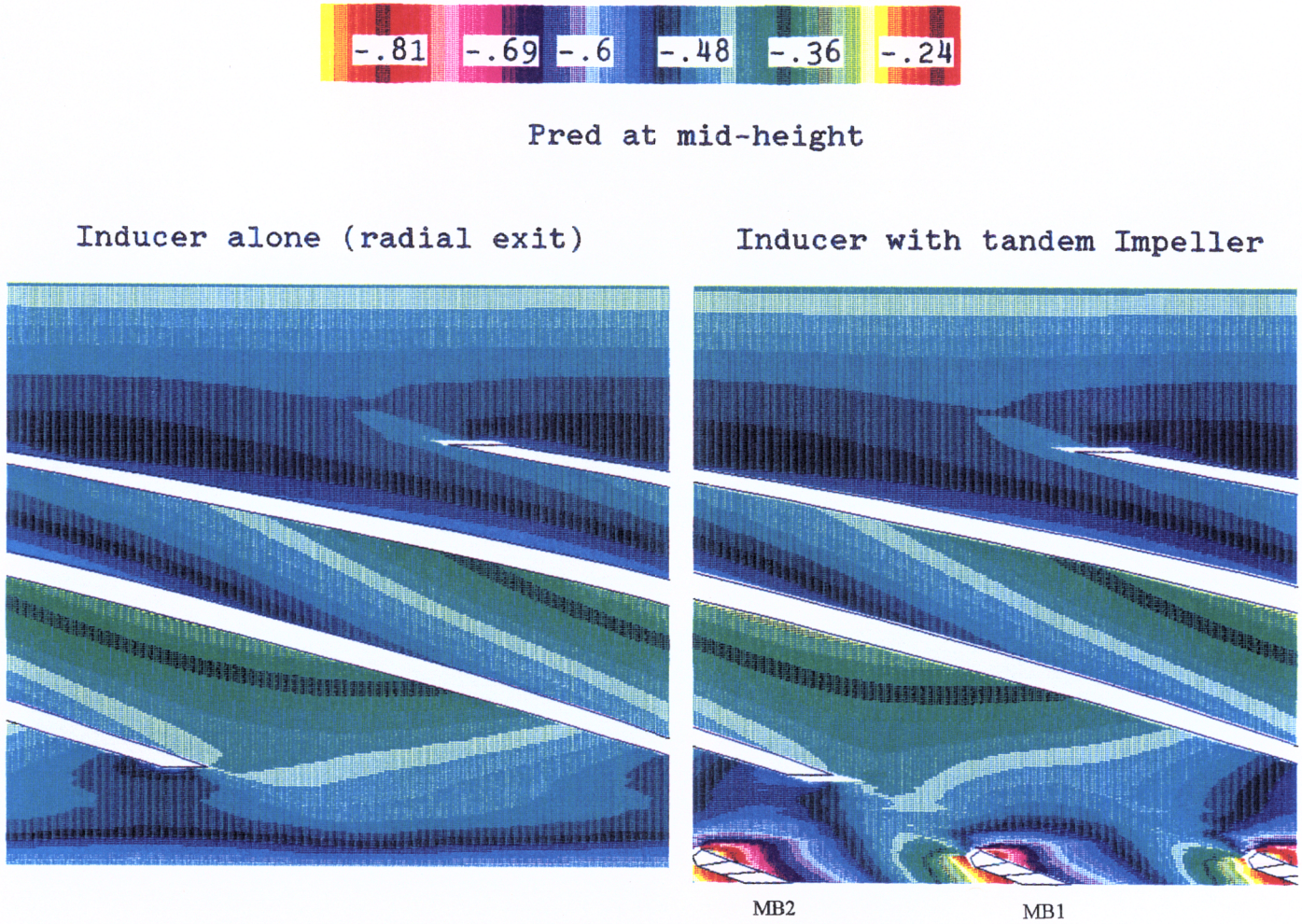


*Figure 64 : Blade-to-blade view of the reduced pressure at mid-height, for the IARC and the ITC .*

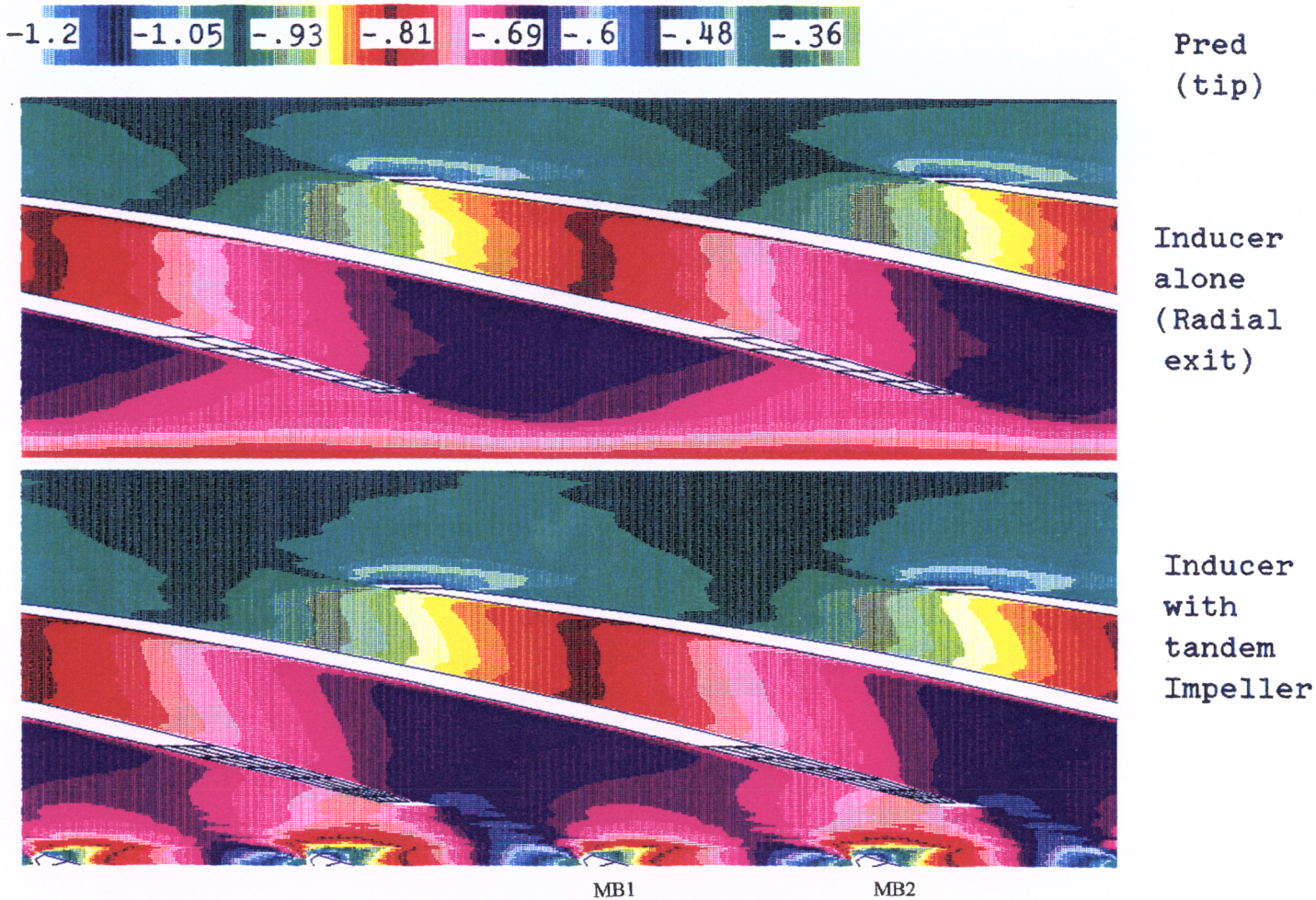


*Figure 65 : Blade-to-blade view of the reduced pressure near the tip & shroud, for the IARC and the ITC .*

constant till about 50 percent of the blade chord, as can be seen by the dark blue contour which builds at the LE. From 50 percent chord till the TE, $P_r$ increases and decelerates the flow. There are no significant differences in $P_r$ between ITC and IARC on the SS .

$P_r$ increases on the PS till mid-chord, and then decreases until the inducer blade TE. The minimum $P_r$ on the TE corner is lower for the ITC than for the IARC. The influence of the impeller is also felt on the uncovered part of the inducer TE, as can be seen by looking at the dark blue zone. Thus, the influence of the impeller goes more upstream into the inducer passage at mid-height. As it was seen at the hub, $P_r$ contours in the ITC build in accordance with the impeller main blades. In particular, flow acceleration or deceleration in the gap and near the blades are similar to those near the hub .

Tip :

As the study is carried on from hub to shroud, the reduced pressure gradient in the inducer passage changes from being blade-to-blade to being mostly in the streamwise direction. Since the radius is almost constant for this tip-section, the reduced pressure contours are almost identical to static pressure contours (to within a constant) .

The reduced pressure rise through the inducer is very similar in both IARC and ITC. Slight differences in the upstream LE region should be due to grid changes (see 4.5.2), and remain relatively minor. The influence of the impeller on the inducer has increased considerably at the tip because the inducer/impeller gap is now relatively small. The impeller modifies the reduced pressure field in the whole uncovered part of the inducer TE, starting on the plane normal to the blades at the inducer TE. In that plane, $P_r$ is maximum ; it then decreases along the inducer PS till the TE. Because of the even smaller inducer TE PS / impeller MB2 SS throat at the tip, $P_r$ decreases even more in this throat, which accelerates the flow considerably. The acceleration is such that LE SS of both impeller main blades are now quite dissimilar, with stronger velocities and higher cavitation inception on the SS of MB2. This was seen in section 5.8 with cavitation intensity on MB2 twice that of MB1 .

### 6.4.3: Rotary stagnation pressure :

Figure 66 gives an overview to losses at the inducer exit. For each configuration, three cross-sectional i-planes show the loss build-up at the inducer TE, at the A=1.225 plane (near the axial cut z=0.091m) and in the inducer/impeller gap (A=1.451). Overall,

there are only very minor differences in the loss patterns. These small differences can be attributed to the different pressure distributions : in the tandem configuration, losses are seen to be slightly weaker near the shroud (compared to the IAC). This is because the presence of the impeller weakens the pressure difference (in the inducer passage) that drives the tip gap flow, and thus the losses generated in the tip gap flow are weaker .

At A=1.225, losses are less circumferentially uniform and more concentrated in a small region in the ITC than in the IAC. This corresponds to the lower pressures seen in the ITC (green, Fig. 62. Note the θ rotation is opposite from Fig. 66) due to the presence of the impeller. The latter maintains a wake development from hub to mid-height, whereas the IAC have a very weak hub to mid-height loss build-up in the inducer wake .

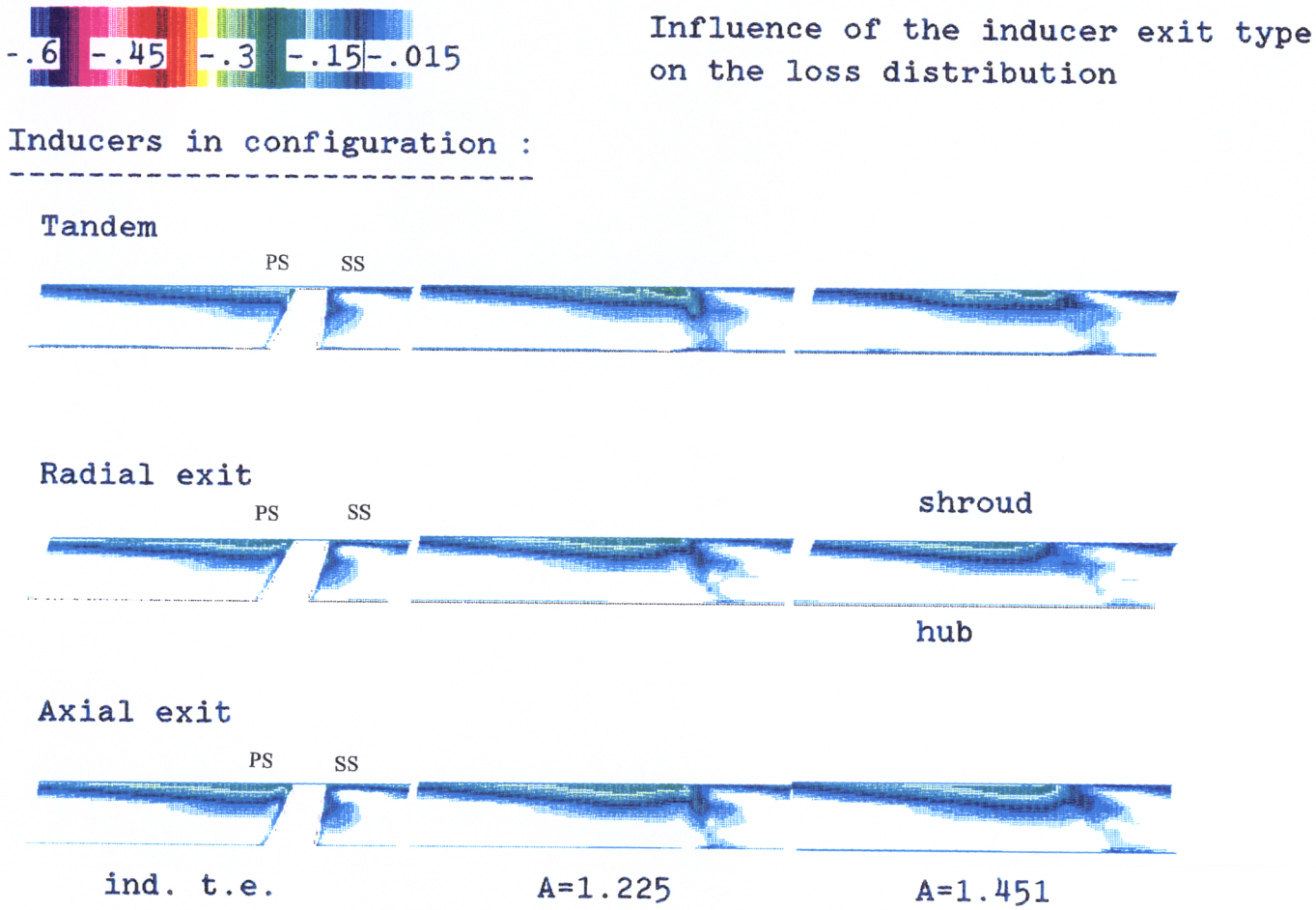


*Figure 66 : Cross -sectional views of loss build-up at the inducer TE and in the gap, for the three configurations .*

## *6.5 Inducer Meridional Analysis :*

## *Static pressure and blade-loading .*

Figure 67 shows the meridional static pressure distribution for the mid-passage. The figure details the results for the ITC, the IAXC and the IARC in that order. An interpolation program was written to get accurate mid-passage surfaces in the three cases, especially for the ITC which has a different blade-to-blade grid .

No significant differences in static pressure contours can be seen within the inducer at mid-passage for the three cases. After the TE, the IAXC shows a radial pressure gradient corresponding to work done and radial equilibrium. Higher pressures are located near the stationary shroud. In the IARC, the radial equilibrium pressure gradient is canceled out by curvature to give a fairly uniform pressure. In the ITC, a strong meridional pressure gradient develops after the inducer TE due to the presence of the impeller .

The blade loadings of the inducers are shown in Fig. 68. With similar pressure distributions on the SS, the blade loading differences mainly depend on the PS patterns. On the second half of the blade (mostly in the uncovered region), the loading of the ITC decreases more rapidly than the IAC. Corresponding to the lower pressures observed on the PS of the ITC, there is a larger region of reverse loading in the ITC than in the IAC. Also, the reverse loading at the TE of the ITC is stronger ($\Delta P \sim -0.12$) than in the IAC ($\Delta P \sim -0.10$) .

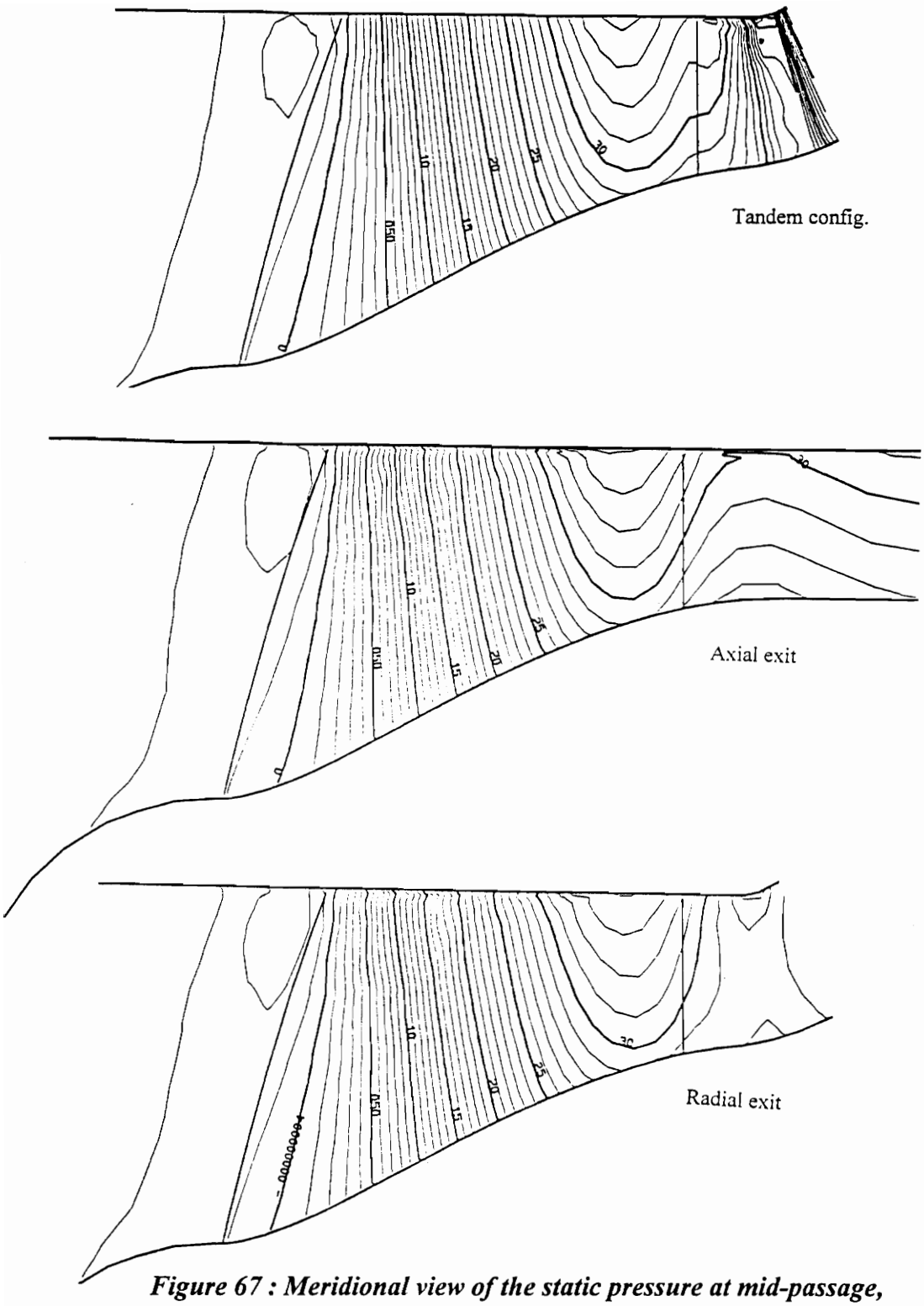


***Figure 67 : Meridional view of the static pressure at mid-passage, for the three configurations.***

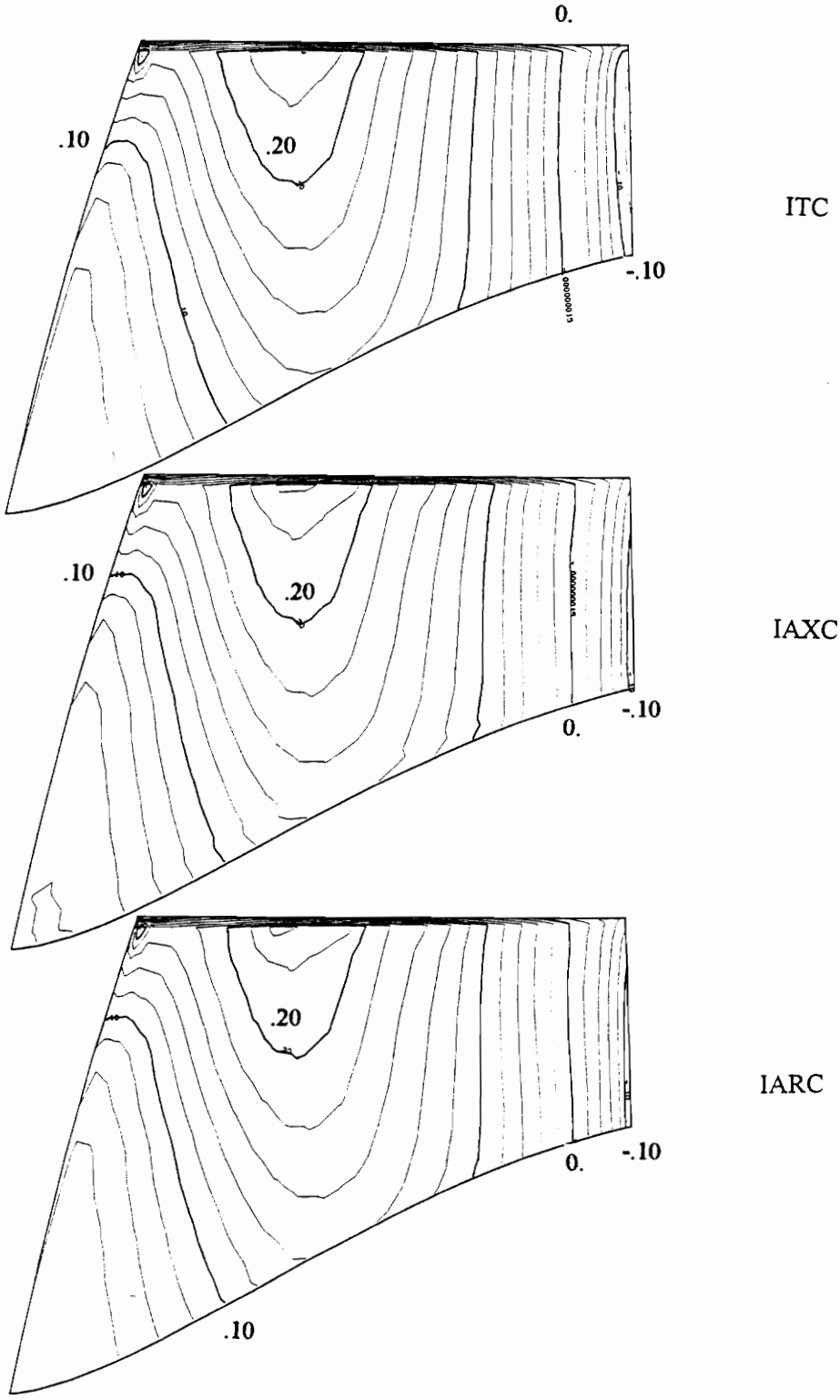


***Figure 68 : Meridional view of the ITC, IAXC and IARC inducers blade loadings .***

## *6.6 Insight into the Inducer/Impeller Uncoupling .*

Combining the results from the present analysis with those from the previous sections enables several conclusions to be drawn for the inducer/impeller uncoupling .

Passage-to-passage differences in loss distribution (Fig. 42) first give an idea about the uncoupling process. In the impeller, the differences that can be seen passage-to-passage are mostly created within the centrifugal stage itself. Corresponding passages in the impeller are very similar to each other in flow (see passages SP2-MB1 and SP4-MB2 for example). They are also very different from the other passage pairs, MB1-SP3 and MB2-SP1, and SP3-SP4 and SP1-SP2 .

Therefore, the circumferential non-uniformity of the inducer exit losses (Figs. 56.c and 66) has a small effect compared with the subsequent changes due to the impeller flow development .

This is furthermore consistent with the fact that losses are produced approximately equally (Fig. 27) between the inducer, the impeller LE and the splitters' leading edges. This loss production process is more important than the non-uniformities in the inducer exit flow, and small changes in the inducer exit flow will not have consequent influences on the impeller .

Figures 56.c and 57.b showed that the circumferentially averaged loss and relative tangential velocity (i.e., the work) distributions at the inducer exit were almost independent of the geometrical shape of the inducer exit . Thus, the choice of exit geometry for the inducer calculation would appear to not significantly influence the impeller inlet flow .

However, the presence of closely coupled downstream impeller blades has been shown to create local geometric throats, with associated low static pressures. These throats have been seen to affect the minimum static pressures at the leading edges of the main blades, and may therefore influence impeller suction performance. Furthermore, if the impeller had less losses at the main blade and splitter leading edges, this centrifugal stage would become more sensitive to small variations in inlet profiles. Impeller losses would no longer be more important that inducer exit losses. Then, details of the impeller leading edge flows and losses may also be more sensitive to circumferential variations in static pressure than the present flow calculation has shown .

**Procedure for performing an impeller alone calculation :**

The following steps suggest a way to perform an impeller alone calculation :

_ the inlet plane should be taken at about one-third of the inducer/impeller gap downstream of the inducer trailing edge (see section 6.2.3), and before the start of the axial-to-radial bend at the shroud .

_ use the axial configuration (seen to give better results) to determine the P* and $\overline{\overline{W_\theta}}$ circumferentially averaged profiles at the inducer exit .

_ assume $V_r$=0 on average in the inlet plane .

_ compute the static pressure field using the radial equilibrium equation (which uses $\overline{\overline{W_\theta}}$ )

_ using P* and the newly found pressure field, compute the axial velocity distribution .

_ check that the axial velocity matches the velocity given by continuity, $\dot{m}$ / (ρA) .

_ if it does not, the pressure level needs to be adjusted till the same flow rate is achieved .

From this entire study, it appears that the following procedure could be adopted for tandem inducer/impeller pump rotor design :

_ First step : predesign of the tandem geometry .

_ Second step : inducer calculation with axial exit .

_ Third step : uncoupled redesign of the impeller .

_ Fourth step : Coupled check of the geometry with a full tandem inducer/impeller configuration .

The last step should be used to help set the optimum indexing of the impeller relative to the inducer, and thus to optimize the suction and hydrodynamic performance of the impeller .

## *6.7 Conclusions relative to downstream inducer influences .*

The impeller has only a minor influence on the inducer. With the current indexing of the MCA impeller relative to the inducer, the impeller increases the reverse loading at the TE of the inducer. This slightly decreases both the work (less pressure loading) and the losses (less tip leakage flow and losses) in the inducer. The ITC has 4 percent lower work than the IARC, and 6 percent lower losses. Thus, the ITC has a slightly higher efficiency, 89.8 percent, than the IARC, 89.6 percent .

Inducer flow calculations were performed with three exit flow geometries : with the impeller downstream, with the impeller blades removed but the same hub and shroud walls, and with an axial exit. Comparisons of circumferentially averaged results for all three configurations were made on an axial plane downstream of the inducer. These results surprisingly showed better agreement between the axial configuration and the tandem configuration than between the radial and the tandem configurations. This was especially noticeable for the axial velocity, the static pressure and the relative flow angle .

Useful redesign studies for the impeller can be started with uncoupled inducer and impeller calculations over the flow coefficient range of interest. The losses at the MCA impeller LE are sufficiently high, due to incidence and high blade loading, that the impeller calculations can be made using circumferentially averaged properties from either an axial or a radial exit inducer. The method for doing this has been described in section 6.6 .

A final phase of the redesign process could involve coupled inducer-impeller flow calculations to optimize the blade indexing, and thus to optimize the suction and hydrodynamic performance of the impeller .

# 7.0 CONCLUSIONS .

**Tandem Inducer / Impeller .**

Three-dimensional flow was computed through a complex tandem axial-inducer / centrifugal-impeller configuration using the 3D turbulent Navier-Stokes code, MEFP. This calculation was made at real engine working conditions with liquid hydrogen and a high Reynolds number. It is the first known 3D calculation of the non-cavitating flow inside such a geometry .

The flow calculation represents one of the most advanced numerical investigations of the flow field in rocket pumps. In a logical evolution since LeFur [17] and Excoffon [18], flows with ever increasing geometric complexity have been numerically solved for an inducer, a tandem bladed inducer and finally this geometry. These calculations were probably the first for each type of geometry .

The conclusions relative to each component of the MCA pump showed the following interesting characteristics :

*Flow in the inducer :*

1) the inducer inlet flow is dominated by a circumferentially uniform tip leading edge vortex driven by the locally high blade loading .

2) cavitation inception is predicted to occur near the suction side of the inducer blade over the outer half of the blade height. It is also predicted within the tip clearance gap where it appears to be stronger .

3) the inducer boundary layers are centrifuged towards the tip and mix with the tip leakage flow that moves the fluid from suction side to pressure side of the passage .

4) the loss distribution at the inducer exit shows high losses in the shroud half, and low losses in the hub half of the annulus .

5) the inducer trailing edge experiences a reverse loading on the uncovered part of the blade. This unloading is enhanced by the presence of the impeller. Modification of the inducer blade shape might be suggested, but it may not entirely solve the problem .
6) the inducer head coefficient and efficiency were predicted to be 0.186 and 89.8 percent, respectively .

*Flow in the impeller :*

1) the locally high positive incidence at the impeller inlet causes an unexpected appearance of cavitation. It also causes high blade loadings for a short distance at the impeller leading edges, resulting in high loss production on the suction side of the blades.
2) a balanced flow split is achieved in the impeller main passages. More differences occur in the splitter passages : channels including the pressure sides of the main blades have higher flow rates than the other passages .
3) the flow splits are affected by the loss distribution. High losses result in lower flow rates .
4) the losses evolve gradually in the inducer, but more rapidly at the leading edges of the impeller main blades and of the splitter blades .
5) the flow development in this impeller is therefore not very sensitive to small changes in the inducer exit loss distribution .
6) the impeller flow shows a fairly good development, with limited stall inception on high loss suction sides .
7) the impeller blade loading is quite similar for corresponding blades .
8) the impeller head coefficient and efficiency were predicted to be 0.69 and 97.5 percent, respectively .

*Flow in the Inter-Blade gap :*

In the inducer/impeller gap, the flow tends to spill from the pressure side to the suction side just upstream of both impeller main blades. The flow then accelerates around the suction side of the leading edges as it enters the impeller main passages. Because of the small throat formed by the inducer trailing edge and the leading edge of the impeller main blade MB2, the flow accelerates even more in this throat. MB2 therefore has higher leading edge velocities and higher cavitation inception than MB1 .

## Influence of Downstream Geometry on Inducer Flow .

*_ Downstream Inducer Influences :*

The influence of downstream geometries on the inducer flow was studied. Three exit geometries were considered : with the impeller downstream, a radial exit with the impeller annulus geometry but with the blades removed, and an axial exit .

The main results were found to be :

1) the three inducer exit geometries give approximately the same overall inducer performance. The total pressure rises for the axial and radial exits are the same, $P_t$=0.385. Due to the unloading of the inducer trailing edge, the impeller reduces the total pressure rise to $P_t$=0.371. The efficiencies are all the same, 89.7 percent .

2) the circumferentially averaged results at the inducer trailing edge showed that the axial exit inducer gave better agreement with the tandem configuration than the radial exit.

*_ Blade Row Uncoupling :*

Losses generated in the impeller itself are much more important than loss non-uniformities at the inducer exit. The latter therefore do not significantly influence the impeller flow. This conclusion combined with the good agreement between the circumferentially averaged results at the inducer exit for the different exit geometries suggests that separate calculations could be performed with reasonable accuracy for both elements of the present geometry (i.e., initial redesign calculations can be performed for the impeller alone). A procedure was therefore suggested for performing an impeller alone calculation starting with inducer exit results .

However, because of circumferential variations in the flow in the inducer/impeller gap, a coupled inducer/impeller calculation is recommended to more accurately predict suction performance .

## Suggestions for Design Improvements .

The redesign should concentrate on the impeller head rise, the impeller flow split and the inducer/impeller gap (length and indexing) :

1) the impeller head rise could be increased by increasing the impeller exit blade angles. Also, the unloading of the impeller trailing edges might need to be improved by changing

the shape of the blades. However, residual unloading will remain because of the uncovered section .

2) major work appears to be necessary to define the optimum design of the splitters to obtain a better flow split. The location of the partials in the meridional and blade-to-blade views has to be determined using the loss distribution in the impeller .

3) the inducer/impeller matching may require a larger gap, as suggested by Jakobsen, or as seen in the current technologies .

**Contributions to Tandem Inducer/Impeller Design .**

The results presented in this thesis give a good description of the flow in the tandem configuration. Besides providing insight into the flow characteristics and answering the uncoupling question, the present calculation also embodies the final step of the design procedure started at SEP [42]. The overall results show a relatively good quality of the turbopump geometry, even though the design procedure could not be fully implemented for the impeller. No severe problems have arisen in the flow results .

The encouraging results obtained here support the ever growing interest in 3D Navier-Stokes codes for the design and validation of pump geometries .

# BIBLIOGRAPHY .


[1] : **WISLICENUS George F.**
"Preliminary Design of Turbopumps and Related Turbomachinery" .
NASA Reference Publication 1170 - 1986
Reference : TJ267 W58 1986 .

[2] : **ROCKWELL Industry, ROCKETDYNE Division**
"Challenges in Space Shuttle Main Engine Rotating Turbomachinery" .
Doc BC 83-33 Feb. 14th, 1983 .

[3] : **JAKOBSEN J.K.**
"Liquid Rocket Engine Turbopump Inducers" .
Series on NASA Space Vehicle Design Criteria .
NASA SP-8052, May 1971 .
Reference : TL521 A333 No8052 , Microfiche N71 34950 .

[4] : **Anonymous .**
"Liquid Rocket Engine Centrifugal Flow Turbopumps" .
Series on NASA Space Vehicle Design Criteria (Chemical Propulsion) .
NASA SP-8109, December 1973 .
Reference : TL521 A333 No8109 .

[5] : **ACOSTA A.J.**
"An Experimental Study of Cavitating Inducers" .
Proceedings of Second Symposium on Naval Hydrodynamics .
Washington, D.C., pp.533-557, August 1958 .

[6] : **SOLTIS R.F. , ANDERSON D.A. and SANDERCOCK D.M.**
"Investigation of the Performance of a 78 deg. Flat Plate Helical Inducer"
NASA TN D-1170, March 1962 .

[7] : **MULLAN P.J.**
"An Investigation of Cavitating Inducers for Turbopumps" .
Gas Turbine Laboratory, M.I.T Report No. 53, May 1959 .

[8] : **SOLTIS R.F. , ANDERSON D.A. and SANDERCOCK D.M.**
"Cavitation and Noncavitation Performance of a 80.6 deg. Flat-Plate Inducer at Three Rotational Speeds" .
NASA TN D-1439, 1962 .

[9] : **SOLTIS R.F. , ANDERSON D.A. and SANDERCOCK D.M.**
"Performance of an 84 deg. Flat-Plate Helical Inducer and Comparison with Performance of Similar 78 deg. and 80.6 deg. Inducers" .
NASA TN D-2553, 1964 .

[10] : **LASHMINARAYANA B.**
"Visualization of Flow in Axial-Flow Inducers" .
Transactions of the ASME .
Journal of Basic Engineering, Vol.94, December 1972 .

[11] : **LASHMINARAYANA B.**
"Three Dimensional Flow Field in Rocket Pump Inducers, Part 1 : Measured Flow Field Inside the Rotating Blade Passage and at the Exit" .
Transactions of the ASME .
Journal of Fluids Engineering, pp.567-578, Decmber 1973 .

[12] : **LASHMINARAYANA B.**
"Experimental and Analytical Investigation of Flow Through a Rocket Pump Inducer" .
Fluid Mechanics Design and Acoustics of Turbomachinery .
NASA SP-304, Part 2, 1974 .

[13] : **LASHMINARAYANA B.**
"Analytical and Experimental Study of Flow Phenomena in Noncavitating Rocket Pump Inducers" .
NASA Contractor Report 3471, October 1981 .

[14] : **LASHMINARAYANA B.**
"Fluid Dynamics of inducers - A Review" .
Transactions of the ASME .
Journal of Fluids Engineering, Vol.104, pp.411-427, December 1982 .

[15] : **LASHMINARAYANA B. and GORTON C.A.**
"Three Dimensional Flow Field in Rocket Pump Inducers, Part 2 : Three Dimensional Viscid Flow Analysis and Hot Wire Data on Three Dimensional Mean Flow and Turbulence Inside the Rotor Passage" .
Transactions of the ASME .
Journal of Fluids Engineering, Vol.99, No.1, pp.176-186, March 1977 .

[16] : **COOPER P. And BOSCH H.B.**
"Three Dimensional Analysis of Inducer Fluid Flow" .
NASA CR No.54836, NASA STAR Index N66-22266, February 1966 .

[17] : **LEFUR Thierry**
"Computational Study of 3D Turbulent Air Flow in a Helical Rocket Pump Inducer" .
M.S. Thesis, VPI&SU, December 1989 .

[18] : **EXCOFFON Tony**
"3D Flow and Performance of a Tandem-Bladed Rocket Pump Inducer" .
M.S. Thesis, VPI&SU, April 1982 .

[19] : **MOORE J.G.**
"An Elliptic Calculation Procedure for 3D Viscous Flow" .
AGARD Lecture Series No.140 on 3D Techniques Applied to Internal Flows in Propulsion Systems, Rome, Cologne, Paris. June 1985 .

[20] : **MOORE John , LEFUR Thierry and MOORE Joan G.**
"Computational Study of 3D turbulent Air Flow in a Helical Rocket Pump Inducer" .
AIAA Paper No. 90-2123 presented at the 26th Joint Propulsion Conference, Orlando, Florida - July 1990 .

[21] : **BARIO F. , BARRAL L. , BOIS G.**
"Air Test Flow Analysis of the Hydrogen Pump of Vulcain Rocket Engine" .
Pumping Machinery - FED, Vol.81, July 8-12 1989, pp.149-155 .
Reference : TA357 F25 v.81 .

[22] : **HOWARD J.H.G. , HUTCHINSON B.R. and BROBERG R.B.**
"Flow Analysis in a Spiral Inducer Impeller" .
ASME Paper 93-GT-227, 1993 .
Reference : TJ7 A4 .

[23] : **EL GHAZZANI E.M. , BOIS G. , GEAI P. And LEBOEUF F.**
"Three-Dimensional Inviscid Flow Computations in a Spatial Turbopump Inducer Using a Distributed Loss Model" .
ASME Paper 92-GT-65, 1992 .

[24] : **HAMKINS C.P. , FLACK R.D.**
"Laser Velocimeter Measurements in Shrouded and Unshrouded Radial Flow Pump Impellers" .
Transactions of the ASME .
Journal of Turbomachinery, Vol.109, pp.70-76, January 1987 .
Reference : TJ267 T58 v.109

[25] : **MERKLE C.L , BROWN J.R , McCARTHY J.P. , NORTHAM G.B. , POVINELLI L.A. , STANGELAND M.L. , ZUKOSKI E.E.**
Chapter 4 :
"Turbomachinery Components" by STANGELAND M.L. , pp.89-146 .
NASA - JTEC .
JTEC Panel Report on "Space and Transatmospheric Propulsion Technology". August 1990 .

[26] : **KAMIJO Kenjiro , HIRATA Kunio .**
"Performance of Small High Speed Cryogenic Pumps" .
Transactions of the ASME .
Journal of Fluids Engineering, Vol.107, pp.197-204, June 1985 .
Reference : TA349 J6 Vol.107 .

[27] : **CAMPBELL W.E. , FARQUHAR J.**
"Centrifugal Pumps for Rocket Engines", pp.655-687 .
Pumping Machinery For Aerospace Applications .
Reference : NASA SP TL521 A333 No.304 pt.2 .

[28] : **JANSEN Willem , KIRSCHNER Andreas M.**
"Impeller Blade Design Method for Centrifugal Compressors" .
pp.537-563 .
Turbomachinery Design .
Reference : NASA SP TL521 A333 No.304 pt.2 .

[29] : **AL-ZUBAIDY Sarim N.J.**
"Advanced Direct-Design Procedure for Centrifugal Compressors" .
Journal of Propulsion and Power, Vol.9, No.1, Jan.-Feb. 1993
Reference : TL780 J68 , Vol.9, No.1, pp.67-73 .

[30] : **BOYCE M.P. , BALE Y.S.**
"A New Method for the Calculations of Blade Loadings in a Radial Flow Compressor" .
ASME Paper No.71-GT-60 . Reference : TJ7 A4

[31] : **ZANGENEH M.**
"Inviscid-Viscous Interaction Method for 3D Inverse Design Centrifugal Compressors" .
ASME Paper No.93-GT-103 . Reference : TJ7 A4

[32] : **CASEY M.V. , DALBERT P. , ROTH P.**
"The Use of 3D Viscous Flow Calculations in the Design and Analysis of Industrial Centrifugal Compressors" .
Transactions of the ASME .
Journal of Turbomachinery, Vol.114, pp.27-37, January 1992 .
Reference : TJ267 T68 .

[33] : **FURST R.B.**
"Space Shuttle Main Engine Turbopump Design and Development" .
AIAA Paper No.75-1301
AIAA/SAE 11th Propulsion Conference,
Anaheim, California / September 29-October 1, 1975 .
Reference : TL510 A688 A22x

[34] : **FURST R.B.**
"Space Shuttle Main Engine Turbopump Design" .
Rocketdyne Division / Rockwell International .
Reference : TL1S6 No.730926

[35] : **CSOMOR A. , FAULKNER C. , FERLITA F.**
"ALS Turbomachinery Technology" .
SAE Technical Paper Series .
Aerospace Technology Conference and Exposition .
Long Beach, California, October 1-4, 1990 .
Reference : TL240 S23 , Microfiche : No.90-1882

[36] : **STANGELAND M.L.**
"Turbopumps for Liquid Rocket Engines" .
Reference : TL1 S25 No.924 , 921043 .

[37] : **NASA George C. Marshall Space Flight Center**
"Workshop for Computational Fluid Dynamics (CFD) Applications in Rocket Propulsion"
April 19-21, 1994. Huntsville, Alabama

[38] : **GROHMANN M.**
"Extend Pump Application with Inducers" .
Hydrocarbon Processing, Vol.58, No.10-12, pp.121-124, Oct-Dec. 1979
Reference : TP690 A1 P4 Vol.58 No.10-12 .

[39] : **JOSUHN-KADNER B. , HOFFMANN B.**
"Investigations on a Radial Compressor Tandem-Rotor Stage with Adjustable Geometry" .
Transactions of the ASME .
Journal of Turbomachinery, Vol.115, pp.552-559, July 1993 .
Reference : TJ267 T68 , Vol.115 No.3 .

[40] : **MOORE Joan G.**
"Calculation of 3D Flow Without Numerical Mixing" .
AGARD Lecture Series No.140 on 3D Techniques Applied to Internal Flows in Propulsion Systems, Rome, Cologne, Paris. June 1985 .

[41] : **MOORE John and J.S. TILTON**
"Tip Leakage Flow in a Linear Turbine Cascade"
Transactions of the ASME .
Journal of Turbomachinery, Vol.110, January 1988, pp.18-26 .

[42] : **RENAUD Philippe**
Projet MCA : Avancement du dimensionnement .
Amélioration de l'écoulement méridien dans l'inducteur et le rouet .
Calculs aube-à-aube .
Note interne SEP Service TM/TP . Décembre 1993 .

Uncited References :


[43] : **NISHIDA Akira**
"Investigation of Flow in Centrifugal Impeller with Tandem Inducer" .
M.S. Thesis, Texas A&M University, August 1976 .
Reference : 1976 Thesis N724 c.2 , Texas A&M Univ. Lib.

[44] : **BALJE O.E.**
"Axial Cascade Technology and Application to Flow Path Designs.
Part II - Application of Data to Flow Path Designs" .
Transactions of the ASME .
Journal of Engineering for Power, October 1968, pp.329-340 .
Reference : TJ1 A7 Vol.90 ser.A/B .

[45] : **BALJE O.E.**
"Axial Cascade Technology and Application to Flow Path Designs.
Part II - Application of Data to Flow Path Designs" .
Transactions of the ASME .
Journal of Engineering for Power, October 1968, pp.329-340 .
Reference : TJ1 A7 Vol.90 ser.A/B .

[46] : **KAMIJO K. , SUZUKI A. , SHIMURA T. , HASHIMOTO R. , WATANABE M. , WATANABE Y. , IWABUCHI T. and MORI Y.**
"Experimental Investigation of Small High-Speed High-Head Oxygen Pump".
Nat. Aerospace Lab. (Japan) , NAL Report TR-415, 1975 .

[47] : **KAMIJO K. , HIRATA K.**
"Performance of Small High Speed Pumps".
ASME Symposium on Performance Characteristics of Hydraulic Turbines and Pumps, Boston, Book No. H00280, 1983, pp.165-171 .

# APPENDIX 1 :

# BLADE INTERPOLATION PROCEDURE .

Each blade is going to be redefined onto the single grid (the Final Interpolating Grid, Fig. 17). The interpolation process is also done so the blades will be such as:

* $RR_{PS}(i,j,k) = RR_{SS}(i,j,k) = RRg(i,1,k)$ .
* $ZZ_{PS}(i,j,k) = ZZ_{SS}(i,j,k) = ZZg(i,1,k)$ .
* $\theta_{PS}(i,j,k)$ and $\theta_{SS}(i,j,k)$ are the new interpolated values .

### A.1.1 : Problem set-up :

Figure 69 shows the geometric situation, and defines the notations we need .
Each blade will be interpolated onto the corresponding main grid region defined by the LTE index values stored previously :

| | | |
|---|---|---|
| _ inducer : | | $indI \leq i_g \leq indE$ |
| _ impeller : | - main blade : | $impI \leq i_g \leq impE$ |
| | - splitter blade : | $isplit \leq i_g \leq impE$ |

where :

$i_g$ is the running index of the main grid in the i-direction .
indI is the i-index of the inducer LE in the FIG .
indE is the i-index of the inducer TE .
impI is the i-index of the impeller main blade LE .
isplit is the i-index of the impeller splitter blade LE .
impE is the i-index of the impeller main blade TE .

### A.1.2 : Methodology :

The procedure is here described for one side of the blade .
An elementary control surface is defined on that particular side by a quadrangle ABCD such that:

1) $A(i_b,j_b,k_b)$ 2) $B(i_b+1,j_b,k_b)$
3) $C(i_b+1,j_b,k_b+1)$ 4) $D(i_b,j_b,k_b+1)$

For each point $M(i_g,1,k_g)$ of the main grid, the control surface is looked for, such that M belongs to the surface ABCD. The search is done for :

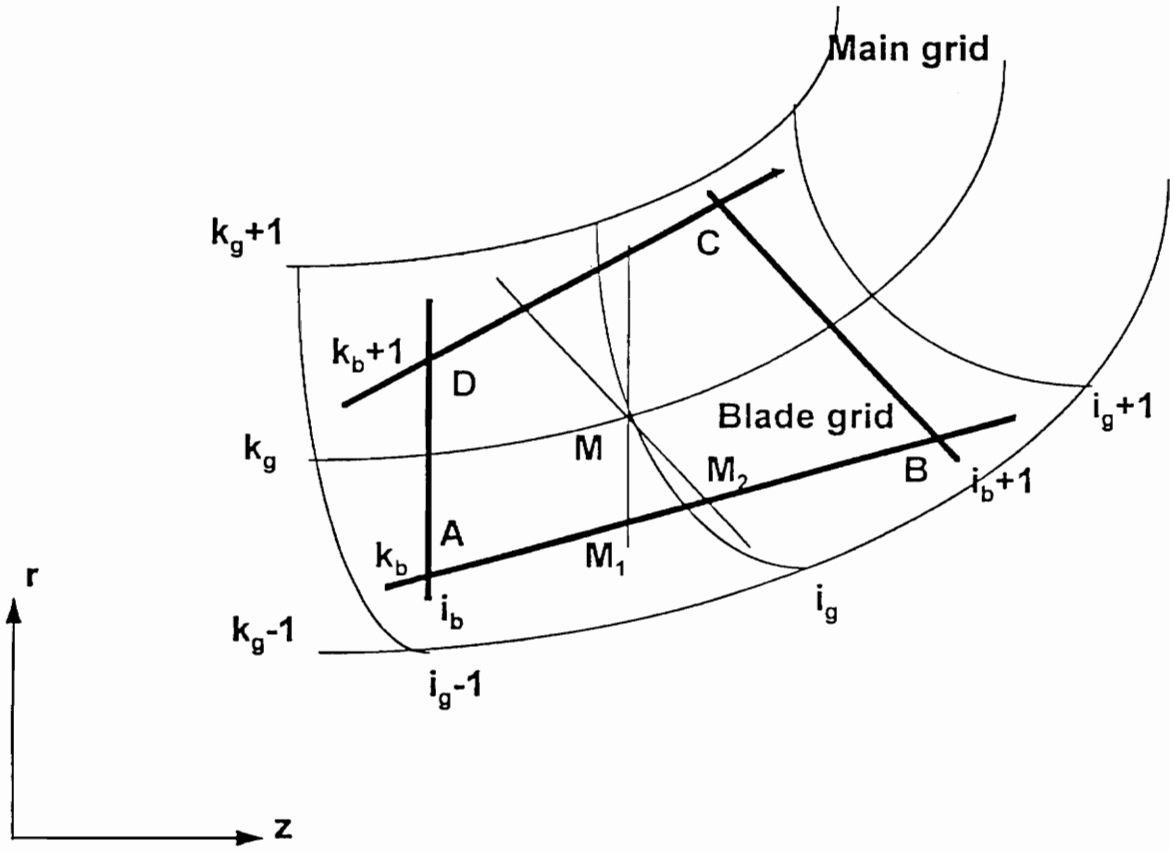


*Figure 69 : Meridional view of the two grid systems (superposition) .*

$indI \leq i_b \leq indE$ or $impI \leq i_b \leq impE$ or $isplit \leq i_b \leq impE$

$j_b = 1$ or 2

$k_g\text{-}1 \leq k_b \leq k_g+1$ .

### A.1.2.1 : M is an inner grid point :

M is neither a hub, nor a shroud, nor a LE nor a TE point .
The search procedure for the control surface that contains M consists in moving the quadrangle ABCD in the $i_b$-direction for each $k_b$-layer until M belongs to ABCD .

The criterion for M to belong to the quadrangle is based on projections. We define 8 projections :

_ proj. of M on AB using the AD direction
_ proj. of M on AB using the CB direction
_ proj. of M on BC using the AB direction
_ proj. of M on BC using the DC direction
_ proj. of M on CD using the BC direction
_ proj. of M on CD using the AD direction
_ proj. of M on DA using the CD direction
_ proj. of M on DA using the AB direction

Then we form eight scalar products of the following type **AM1 . AB** and **AM2 . AB** . M will be said to belong to the control surface if at least one of the two scalar products is positive for each side of the surface. Once A,B,C and D are found, a double linear interpolation finds $\theta_M$ using $\theta_A$,$\theta_B$,$\theta_C$ and $\theta_D$ .

### A.1.2.2 : M is a border grid point :

_ If M is a hub point & M is not at the TE :
ABCD are still defined but the search is done for $k_b$=1 .

_ If M is a hub point & M is at the TE :
Then A and B are on the hub, B and C are on the TE. The search is done for $k_b$=1 .

_ If M is a shroud point & M is not at the TE :
Then C and D are on the shroud and the search is done for $k_b$=16 .

_ If M is a hub point & M is at the TE :

C and D are on the shroud, B and C are on the TE. The search is done for $k_b$=16 .

The search procedure for a border grid point is identical to the inner grid point case.

### A.1.2.3 : Double linear interpolation :

A,B,C,D have been found .

If **AM1** . **AB** and **AM2** . **AB** are both positive, we keep E=M1 for the interpolation. If one of the two scalar products is negative, we keep E as the point for which the product is positive .

Once E is defined, F is automatically defined by E and M (see figure 70). We then calculate :

$$\theta_E = \theta_A + (\theta_B - \theta_A) * \frac{AE}{AB} \quad \text{and} \quad \theta_F = \theta_D + (\theta_C - \theta_D) * \frac{DF}{DC}$$

Finally, the interpolated value for $\theta_M$ is given by :

$$\theta_M = \theta_E + (\theta_F - \theta_E) * \frac{EM}{EF}$$

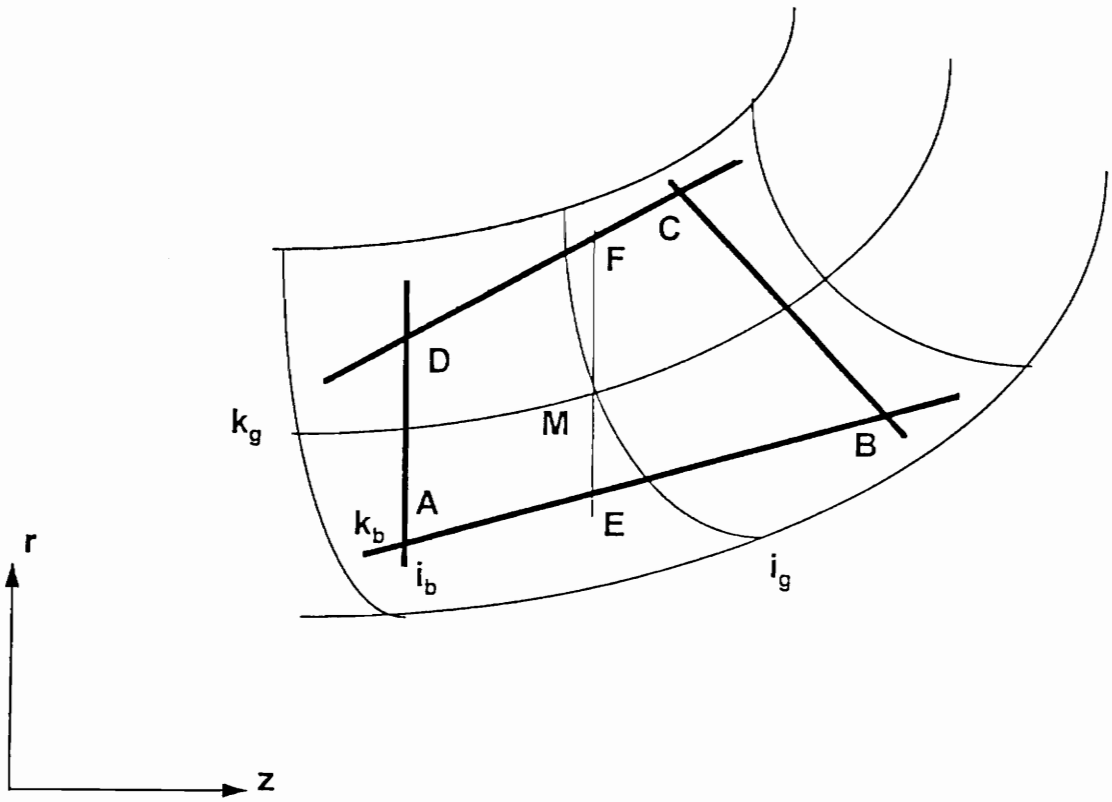


*Figure 70 : Double linear interpolation scheme .*

# APPENDIX 2 :

# MEFP GEOMETRY FORMAT

The MEFP geometry format follows the GEOMI specifications [48] .
GEOMI is a software able to handle computational grids in the format compatible with the MEFP code. To manipulate grids, GEOMI uses a triple coordinate system (see Figure 71) :

1.) A cylindrical coordinate system (r,θ,z) or a Cartesian coordinate system (x,y,z) to define the coordinates of each point of the grid. When a rotating frame is desired (flow on rotor), the (r,θ,z) coordinate system must be used and the rotation must be about the z-axis. When a repeating boundary is used, the repeat must occur in the y or θ direction .

2.) The (i,j,k) coordinate system numbers the consecutive lines of the grid in the three directions with consecutive integers, from 1 to the grid dimension in each direction (idim,jdim,kdim). The I,J and K directions do not need to be orthogonal or even smooth. However, they must form a right-handed grid system with IxJ having a positive component in the K-direction .

3.) The (A,B,C) coordinate system supplies an arbitrary (however ascending with respect to the I,J,K coordinates) real value to each line of the grid in each direction. This coordinate system is essentially used to modify the grid by interpolation, as explained below, When possible, A,B and C are chosen proportional (at least locally) to the distance .

In the example of Figure 71, a Cartesian coordinate system has been chosen. The horizontal plane on display can be referenced as either K=3 or C=2.5. In case a new plane must be inserted at the coordinate A=3.5, i.e. between the planes I=2 (A=3.0) and I=3 (A=4.0), GEOMI can create it by interpolation with respect to the A coordinate. The A values are unchanged in the new grid but the I planes are incremented by 1 for the planes following the new plane which is now defined by I=3. The dimension of the grid in the I direction is also incremented by 1.

<u>The point definition :</u> As stated above, the point coordinates can be defined either in a Cartesian coordinate system x,y,z (type 1) or a cylindrical coordinate system r,θ,z (type 2). Each point must also be assigned an integer called LT value, according to the following specifications :

| | | |
|---|---|---|
| 1 | = | free stream |
| 2 | = | free stream |
| 3 | = | rotating solid wall |
| 4 | = | stationary solid wall |
| 5 | = | inside a solid body |

Geometry file format : The standard format for a grid file is the following :

COMENT

IDIM , JDIM , KDIM , LCOOR

( B(j) , j=1,JDIM ) , ( C(k) , k=1,KDIM )

For i=1,IDIM

A(i), (((LT(i,j,k),C1(i,j,k),C2(i,j,k),C3(i,j,k)) , j=1,JDIM), k=1,KDIM)

Where :

COMENT is one line of comments

IDIM,JDIM,KDIM are the dimensions of the grid

LCOOR gives the type of the coordinate system (1=cartesian , 2=cylindrical)

A(),B(),C() are arrays of the A, B and C values

LT(i,j,k) is an array of LT values

C1(i,j,k),C2(i,j,k),C3(i,j,k) are arrays of the three coordinates, with :

C1 = x or r

C2 = y or θ

C3 = z .

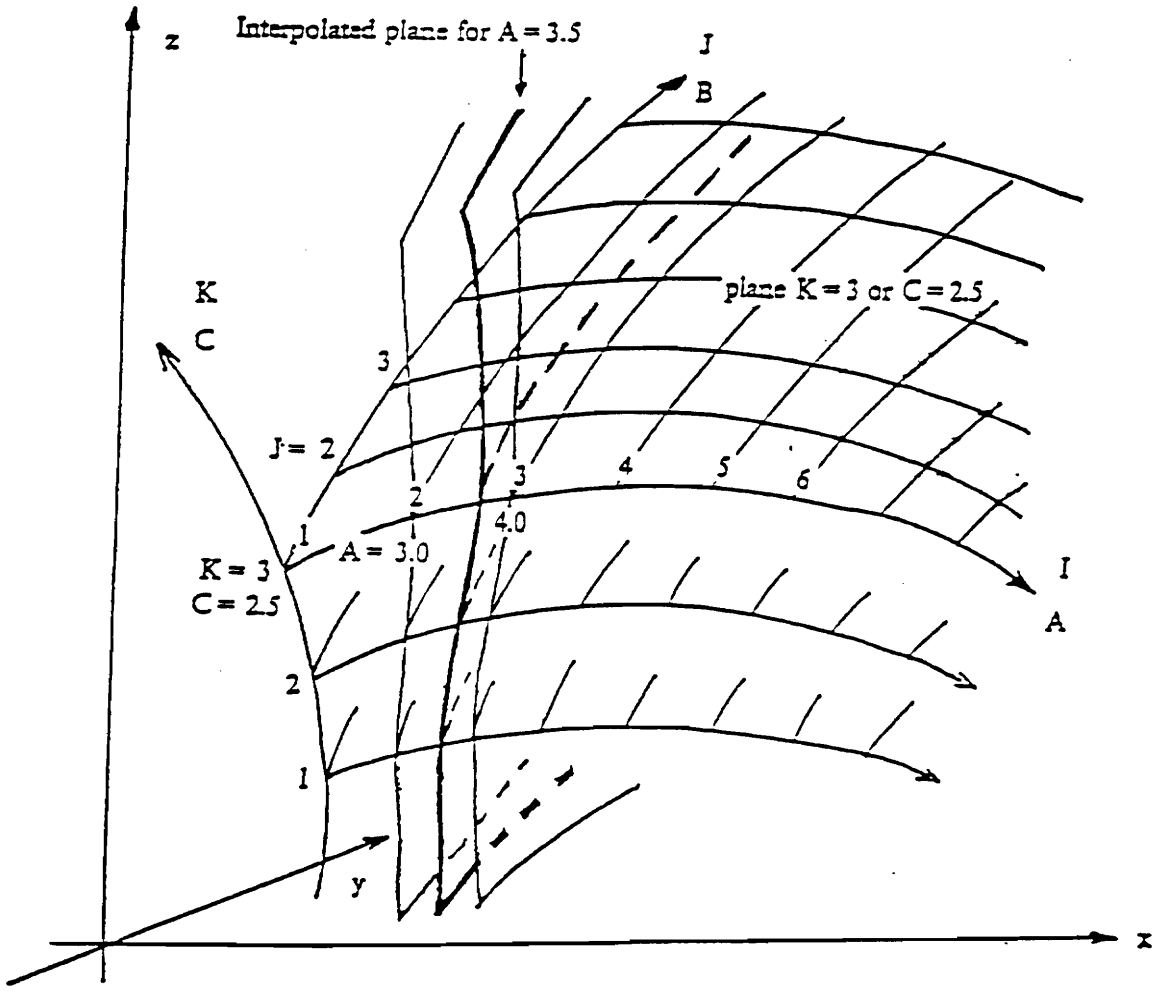


*Figure 71 : GEOMI triple coordinate system : (I,J,K) , (A,B,C) and (x,y,z) (from[5])*

# Vita

Philippe Renaud was born on May 3, 1969, to Annie P. and Michel C.M. Renaud in Pont-à-Mousson, France. After he completed his High School studies at the Lycée Jacques Marquette in Pont-à-Mousson, he spent two years at the Lycée Henri Poincaré in Nancy to prepare the national "Concours d'entrée aux Grandes Ecoles". He entered the "Ecole Nationale Supérieure d'Hydraulique et de Mécanique de Grenoble" (Mechanical Engineering) and graduated in June 1992. In September 1992, he entered the "Ecole Nationale Supérieure du Pétrole et des Moteurs" and graduated in July 1993. He started working for the "Société Européenne de Propulsion (SEP)" in Vernon in November 1993. In January 1994, he moved to the USA to complete a Master of Science in Mechanical Engineering at the Virginia Polytechnic Institute and State University, and to work on a research project under the sponsorship of SEP. Upon completion of his thesis, Philippe plans to go back to France and look for a job in the fluid mechanics and turbomachinery field, preferably in an aeronautic company .

Ph. Renaud